Università degli Studi di Trento – Dipartimento di Fisica
Fondazione Bruno Kessler – Integrated Radiation and Image Sensors

Characterisation of Silicon Photomultipliers for the detection of Near Ultraviolet and Visible light

Cycle XXIX

G. Zappala'
Supervised by: N. Zorzi

Abstract

Light measurements are widely used in physics experiments and medical applications. It is possible to find many of them in High–Energy Physics, Astrophysics and Astroparticle Physics experiments and in the PET or SPECT medical techniques. Two different types of light detectors are usually used: thermal detectors and photoelectric effect based detectors. Among the first type detectors, the Bolometer is the most widely used and developed. Its invention dates back in the nineteenth century. It represents a good choice to detect optical power in far infrared and microwave wavelength regions but it does not have single photon detection capability. It is usually used in the rare events Physics experiments. Among the photoelectric effect based detectors, the Photomultiplier Tube (PMT) is the most important nowadays for the detection of low–level light flux. It was invented in the late thirties and it has the single photon detection capability and a good quantum efficiency (QE) in the near–ultraviolet (NUV) and visible regions. Its drawbacks are the high bias voltage requirement, the difficulty to employ it in strong magnetic field environments and its fragility.
Other widely used light detectors are the Solid–State detectors, in particular the silicon based ones. They were developed in the last sixty years to become a good alternative to the PMTs. The silicon photodetectors can be divided into three types depending on the operational bias voltage and, as a consequence, their internal gain: photodiodes, avalanche photodiodes (APDs) and Geiger–mode detectors, Single Photon Avalanche Diodes (SPADs). The first type detector does not have internal gain, thus its signal is proportional to the number of incoming photons that are converted in electron–hole pairs. The detector and the read–out circuit noises limit the detector sensitivity to, at least, some hundreds of photons. The APD exploits the impact ionisation effect to have an internal gain up to some hundreds or more. The internal gain allows the detector to improve the performance with respect to a similar area photodiode reducing the sensitivity limit to some tens of photons. Operating the APDs with a bias voltage larger than the breakdown one, the Geiger–mode operation range can be reached. In this case, the detectors have a very high gain, in the order of $(10^5 \div 10^7)$, but their signal is not proportional to the number of the incoming photons, it is always the same. The SPAD (or GM–APD) is a typical Geiger–mode silicon detector. It has the single photon detection

capability as the PMT, due to the high gain, but its signal is digital: it is fired or not by the incoming photons. The capability to give a signal proportional to the number of photons is lost in a SPAD. To recover this property, a matrix of independent SPADs connected in parallel is built. These matrices are called Silicon Photomultipliers, SiPMs (or Multi–Pixel Photon Counters, MPPCs). In a typical SiPM, the output signal is the sum of the SPAD ones, thus, although the digital nature of the SPAD signal, it is analogue and ranges from zero to the maximum number of cells composing the matrix. The detector response can be considered linear if the number of incoming photons is much smaller than the total number of cells because the probability that two photons arrive on the same cell is negligible. Main features of the SiPMs are the low bias voltage (<100 V typically), a high Photo-Detection Efficiency (PDE) in NUV and visible range (usually larger than the PMT QE), compactness, insensitivity to magnetic fields and high internal gain. The noise sources are the Dark Count Rate (DCR), the optical Cross–talk (CT) and the Afterpulsing (AP). The first is called primary noise and mainly depends, at room temperature, on the thermal generation of electron–hole pairs that can travel to the high–field region triggering a cell. The others are collectively called correlated noise because they can happen only after a primary signal, caused both by a photon or by a spontaneous carrier generation.

In this thesis, the focus is on the characterisation of one SiPM technology produced in Fondazione Bruno Kessler (FBK) in Trento, Italy, named NUV–SiPMs. This technology, implementing the p–on–n concept, showed, from the beginning, a high PDE spectrum peaked in the NUV to violet region exceeding the 30 %, a very low DCR, typically below 100 KHz/mm^2 in the operating voltage range, and a total correlated noise probability under the 50 %. In the last years, the technology was developed modifying the silicon wafer substrate properties, reducing the delayed correlated noise probabilities, and adopting the so–called High–Density concept. In this last version, named NUV–HD, a new layout, with a narrower border region around the cell active area and deep trenches to electrically and optically isolate the cells, is employed. The first improvement has a direct influence on the PDE because it increases the Fill Factor (FF), the ratio between the active to the total cell area. The second layout change reduces the probability that a secondary photon can travel from a cell to a neighbouring one, reducing the cross–talk probability. Possible applications of the NUV–HD devices are: medical application (e.g. the Time of Flight PET, ToF–PET, scanners), the rare events Physics experiments (e.g. NEXT and DarkSide) and Astroparticle Physiscs experiments (e.g. the Cherenkov Telescope Array Observatory, CTA). The ToF–PET scanners are promising medical techniques with the goal of improving the spatial resolution of the classical PET scanners measuring the gamma rays time of flight. For this reason, these scanners require very fast photodetectors with coincidence time resolution (CTR) less or equal to 100 ps. NEXT and DarkSide

are low temperature experiments with the main goal of observe rare events as the neutrinoless double beta decay and the Dark Matter particles. Due to the signal rarity, the detector noise requirements are very stringent. CTA will be a future ground–based Imaging Atmospheric Cherenkov Telescope (IACT) observatory, with the goal to track very high energy cosmic gamma rays, up to hundreds of TeV, to their galactic sources. It will consist of two matrices of telescopes of different type and size, each one having a camera. In the small size telescopes, the possibility to use the SiPMs to build the camera is under investigation. Since the cosmic gamma rays are detected through the secondary Cherenkov photons, produced by the accelerated electrons in the Earth atmosphere, the camera photosensors must have a very high detection efficiency from 300 nm to 600 nm, and, possibly, a low sensitivity in the NIR region to reject the night sky background. In addition, they must have good timing properties and high granularity.

To fully characterise the SiPM, measurements of signal properties, noise parameters and PDE are needed. The set–ups and analysis of the characterisation procedure are fully described. In particular, the optical set–up, with its calibration procedures, and the analysis methods, with the definition of the possible uncertainty sources, are the central point of this work. During the dark characterisation, the SiPM is enclosed in a light–tight climatic chamber. An oscilloscope acquires and sends to a PC software millisecond–long SiPM waveforms. The software implements a Differential Leading Edge Discriminator (DLED) algorithm to better distinguish the SiPM pulses with time separation larger than a few nanoseconds. This analysis allows to count the primary pulses, due to the thermal/tunnelling excitations, obtaining the DCR, and measure the correlated noise probabilities. In addition, signal parameters as amplitude, gain and cell recharge time are measured. The PDE measurements require a set–up in which the number of impinging photons to the device is precisely known. For this reason, a compact set–up, consisting of an integrating sphere inside a light–tight box, a series of LEDs with peak wavelength ranging from NUV to NIR, fully characterised before use, a monochromator, equipped with a tungsten lamp, and a transparent optical fibre, was developed. Along with the set–up, a light calibration procedure, taking into account different uncertainty sources (LED wavelength shift, light uniformity at the device position, etc.), was also developed. Three different analysis techniques can be used to obtain the technology PDE. Each technique has its own benefits and error sources. The equivalence among the different methods is shown. Moreover, measuring the PDE on SPADs with the same layout of single SiPM cells, identical results are obtained. This fact shows the equivalence between the single cell device and its larger counterpart, opening the possibility to measure the PDE of a new technology on SPADs. This is a very important result because the SPAD is a simpler device, with lower correlated noise, because it has no CT, and negligible primary one, often less than 1 kHz. Measurements are

more precise, faster and it is possible to apply larger bias voltage, obtaining more information on the technology in such conditions at which no SiPM can be tested any more.

A first version NUV–HD technology characterisation is shown. In this version, the NUV–HD SiPMs have cell pitch ranging from 25 μm to 40 μm. A typical primary noise lower than 100 KHz/mm^2 and a delayed correlated noise probability less than 5 % are measured, up to 10 V of overvoltage. In the same bias voltage range, a direct CT probability lower than 45 % is measured in the largest cell devices (25 % in the smallest ones). The PDE spectrum has the expected shape with the maximum in the NUV–violet region. A maximum value exceeding the 60 % is measured in the largest cell devices (45 % in the smallest ones). To investigate possible variations of the measured features on the wafer, devices taken from different wafer points are measured and compared finding no difference but the primary noise. This parameter shows a variation by a factor up to about three on the wafer level. To compare the different cell devices, all the measured parameters are plotted as a function of the peak PDE, about 400 nm. During this comparison, the smallest device reveals worse than the others having a larger noise, both primary and correlated, at the same PDE value. The other three devices are comparable within the measurement errors.

From the PDE measurements, a comparison between the measured FF and the expected one, as defined by the design, is obtained. In the smallest cell device, this comparison shows an unexpected discrepancy leading to the possibility that the expected FF is larger than the effective one. This possibility is investigated in the last part of this thesis in which a complete study of the factors contributing to the PDE is shown. This study is performed on a new NUV–HD version employing a photodiode with equal dopant profile of the SiPMs, a circular SPAD having 100 % FF and a square one with 35 μm cell size and a nominal FF equal to 81 %. A developed box model is used to describe the electric field inside the cell. The calculated effective FF is always different from the expected one. The reason of the measured difference is the electric field transition from the constant high value to zero occurring at the active area border region. This partially efficient region has an effect similar to an added completely ineffective region of $1 \div 1.5$ μm size inside the expected active area. The transition region effect is critical for the smallest cells because it strongly reduces the effective FF with respect to the design one.

The study of the factors contributing to the PDE of the NUV–HD SiPMs is very important. Through the obtained results, it is confirmed that the technology QE is just maximised in the wavelength range of interest, NUV to blue, and, at the same wavelengths, the triggering probability saturation rate is very small allowing the detectors to reach the maximum PDE when biased with a few volts of overvoltage. This operating condition has also the effect to employ the detector having low noise, both primary and correlated one.

The best solution to further improve the technology PDE is a redesign of the electric field border region to reduce the gap between the expected FF and the effective one. This is more important for the smallest cell devices in which the actual transition region effect reduces the PDE performance to about the $50 \div 60$ % of the expected values.

Contents

Introduction

The animals on earth have senses that help them to search for the food or a prey and defend against a possible predator or danger. The sight is one of the most important senses to know the world around them. Considering some of their aspects, as their habitat or their class, the animals are very different (e.g. predators or preys, mammals, reptiles, terrestrial animals, flying animals, etc.). Also the evolution of their organ sense, the eye, was different and led to the actual features. In general, it is possible to say that the eyes of two different animals are very different. Anyway, some common element is present in almost all of them:

- a lens, and often an iris, to focus and regulate the intensity of the entering light on an inner sensitive surface called retina;
- the presence in the retina of two different light–sensitive cells called rods and cones (the first ones for low–light contrast, the last for the colour identification);
- an optic nerve that transmits the collected electrical data to the brain for the reconstruction of the image.

Among the animal eyes, it is difficult to classify and establish the best one. Many studies demonstrated that the color vision is not a feature only in the human eye. In [1], the authors summarise the results of about one century of observations. Not all the animals have the color vision capability, and, among the gifted ones, the color perception can be very different. This difference depends on the number of the photosensitive type cones in the eye. Some animal is dichromat, as the tree shrew, some is trichromat, as the humans, and others are tetrachromat, as the Pekin robin. In Figure 1, a comparison between the expected color sensitivity among three different animals is shown. The picture is taken from [1].

Focusing the attention on the human eye, it is possible to report some of its features. In a human eye $\sim$100 million rods and $\sim$5 million cones, each one equivalent to a sensor pixel of the nowadays widely diffused cameras, are present; it has a vertical angle of view of $\sim 120^{o}$ and a horizontal one of $\sim 155^{o}$; it has the ability to distinguish two lines near $\sim$0.1 mm at about 25 cm distance; the visible spectrum ranges between 400 nm and 700 nm.

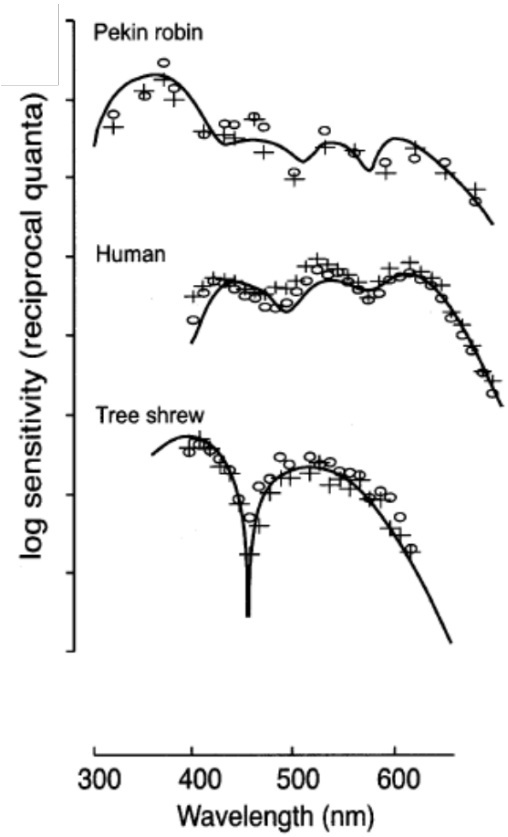

Figure 1: Comparison among the color perception as a function of wavelength for three different animals: tree shrew (dichromat), human (trichromat) and a Pekin robin (tetrachromat). Picture taken from [1].

Even if the human eye is a very sensitive organ, its ability to see the world has some limit. One of the most important is the impossibility to vary the focal length, and thus enlarge the seen images. To overcome this limit and see in detail very far, or very small, objects, instruments as optical telescopes and microscopes were developed during the past centuries. The development of the telescope began in Netherlands in the seventeenth century with the construction of the first refracting telescope (Hans Lippershey, a German–Dutch spectacle–maker, was the first to apply for a patent for this instrument). After half a century, the first model of a reflecting telescope was invented by Isaac Newton. This model did not suffer from the chromatic aberration as the previous models of refracting telescopes. The optical telescopes allowed men to improve the knowledge of the universe (e.g. they help Isaac Newton to write its famous law of universal gravitation). The microscope had a similar history, having been invented in the seventeenth century in Netherlands, probably by the same Hans Lippershey. It allowed great advancements in medical sciences. Even if these instruments greatly helped the science in the past, also they have a limit, the use of the visible light. Many information of distant objects

in space are carried out by photons outside the visible range. In Figure 2, a comparison of the milky way observed using different wavelengths is shown [2]. The importance to use different wavelengths to obtain the maximum number of information is evident.

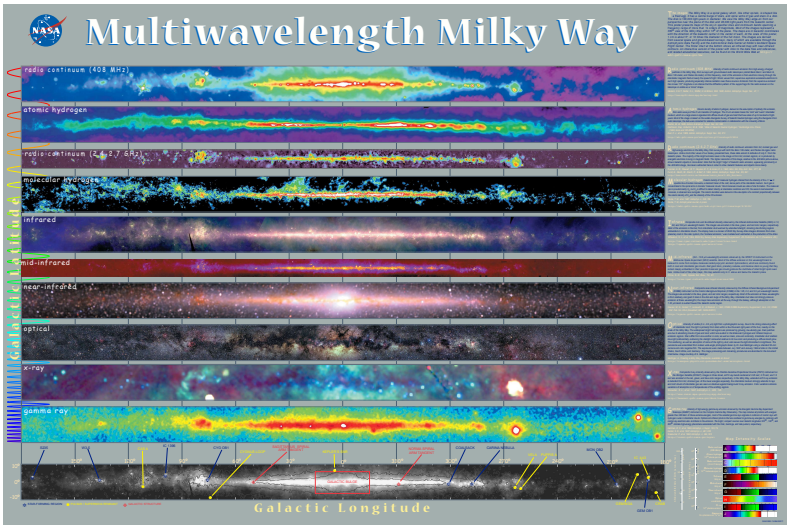

Figure 2: Milky Way observed using different wavelengths, from radio (top) to gamma ray (bottom). Picture taken from [2]. Every wavelength range carries informations not accessible by the others, thus it is of fundamental importance to use all of them to investigate the cosmos.

In the same way, it is not possible to use the visible light to explore the atomic structure of matter because its wavelength is larger than the typical distance between atoms in matter, the optical resolution is not enough. To overcome this limit and obtain the maximum number of information, new light detectors, sensitive also to other wavelengths were developed in the last century.
The development of light detectors with improved sensitivity made light measurements more and more important in many applications as high–energy physics (e.g. calorimetry readout [3]), spectroscopy [4], biotechnology [5], medical applications (PET and SPECT imaging techniques [6]) and astronomy (terrestrial and space telescopes cameras [7]).
Light detectors, or photodetectors, can be divided by their principle of operation and/or material. Nowadays, two main photodetector types are available: thermal type and photoelectric, or photovoltaic, effect based detectors.

Common elements to all thermal detectors (e.g. bolometers, cryogenic and pyroelectric detectors) are [8]:

- the presence of an absorbing material thermally connected to a heat sink;
- the exposure of the absorber to a light flux that increases its temperature;

- the absorber temperature relaxation to the heat sink one, after the exposure ending.

Thermal detectors differ for the readout of the temperature excursion in the absorber. Every detector exploits the operational parameter modification of a component, thermally connected to the absorber, due to the temperature variation.
One of the most widely used thermal detectors is the bolometer, first developed by prof. S. P. Langley in 1881 [9]. Important milestones in the technological development of the bolometers, that lead to the actual models, are reported in [8, 10, 11, 12, 13]. Usually, in a bolometer, a resistive thermometer (RTD) is thermally attached to the absorber material to measure the temperature variation. An RTD consists of a pure material with known resistance/temperature relationship [14] in which a power supply forces a current. Any temperature variation in the resistive element causes an electrical current measurement variation. A schematic representation of a typical bolometer is shown in Figure 3. The bolometers and other thermal detectors are mainly used to measure power at far infrared and microwave wavelength. They do not have a high sensitivity in UV and visible range and they are not single photon detectors.

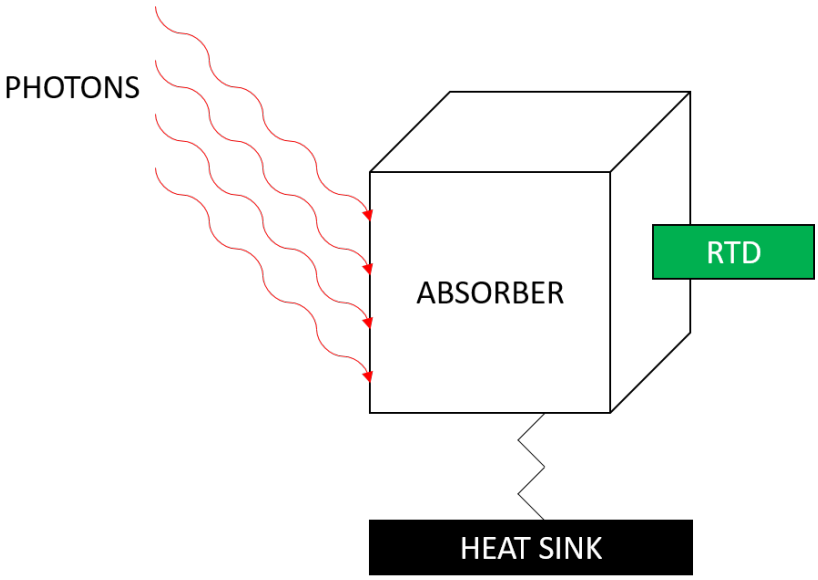

Figure 3: A scheme of a typical bolometer. Main elements, absorber, resistive thermometer (RTD) and heat sink are shown.

The second type detectors are based on the photoelectric (photovoltaic) effect. This phaenomenon was discovered by Hertz in 1887 [15]. He noted that a negative electrode lost its charge faster if illuminated with ultraviolet light. In the subsequent years, until 1889, Hallwachs, Elster and Geistel

confirmed the observations by Hertz, also with visible light striking an alkali metal [16, 17]. After years of different experiments and theories by many scientists, the phaenomenon was finally explained by A. Einstein in 1905 with his famous law of the photoelectric effect [18] that earned him the Nobel Prize in Physics in 1921. Einstein hypothesised that a light flux consisted of an integer number of elementary particles, later named photons, each one having fixed energy, related to the light wavelength by the equation (1):

$$W(\lambda) = n_{ph} E_{ph} = n_{ph} \frac{hc}{\lambda} \tag{1}$$

in which $W(\lambda)$ is the optical power per unit area of the incident light flux, n_{ph} is the photon rate per unit area and E_{ph} is the photon energy. The photon energy can be expressed by the Planck constant, h, the light speed, c, and the light wavelength, λ. The basic elements of the Einstein theory are:

- the photons can free electrons in a material if their energy is at least equal to the element work function;
- the difference between the photon energy and the work function converts in electron kinetic energy;
- any photon can free only one electron.

The difference between the photoelectric and the photovoltaic effects is the final state of the electrons. The photoelectric effect frees the electrons from the material, the photovoltaic effect frees the electrons from their atoms, but they are confined in the conduction bands, thus inside the material.

One of the most important and used photodetector based on the photoelectric effect is the photomultiplier tube (PMT) [19, 20, 21, 22]. The first PMT prototype was developed by the russian physicist L. A. Kubetsky, according to [20], even if, in western countries, V. Zworykin, G. A. Morton and L. Malter are considered the developers of the PMT [19]. In Figure 4, a schematic construction of a linear electrostatic–focusing type PMT is drawn. The PMT consists of a vacuum tube with an input window (the photocathode), a focusing electrode, a chain of dynodes (each one biased with increasing voltage) and a final collector, or anode. The principle of operation of a PMT can be explained with the following steps:

- an impinging photon frees an electron from the photocathode in the vacuum via the photoelectric effect;
- the electric field, caused by the different bias voltage between the photocathode and the first dynode, accelerates the free electron;
- in the first dynode, the electron can produce secondary electrons, via the secondary emission process described in [23, 24, 25];

- the secondary emission process occurs at every dynode due to the increasing bias voltage, thus an avalanche of carriers are generated from the first one;
- the anode collects all the electrons.

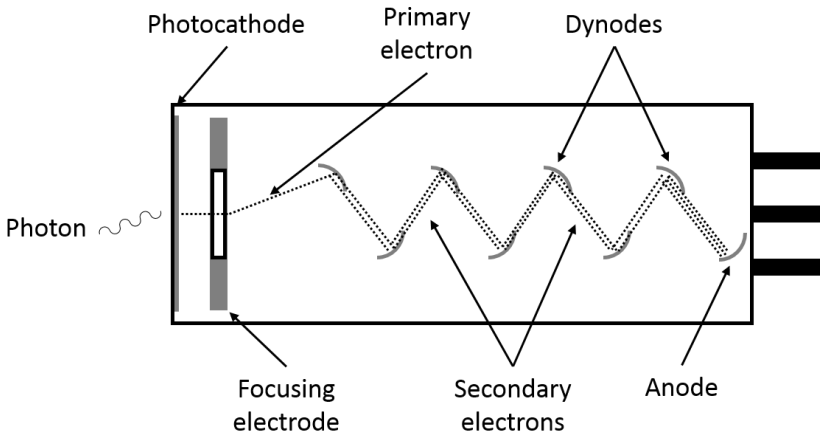

Figure 4: Schematic construction of a linear eletrostatic–focusing type PMT. Main elements (photocathode, dynodes, etc.) are shown.

Typical features and problems of a PMT are:

- high internal gain, defined as the average number of electrons produced per single impinging photon ($10^6 \div 10^8$);
- single photon detection capability, due to the high internal gain;
- very low noise;
- very large dimension range, from a few mm to circular detectors with 20 inches diameter;
- possibility to cover large area;
- good quantum efficiency in NUV and visible range;
- difficult employment in environments with strong magnetic fields;
- non linearity at high intensity light fluxes;
- very high bias voltage, typically larger than 1000–1500 V;
- stabilisation period (typically hours) is needed before operation;
- overexcitation risk;

- fragility and cost.

Even if the PMT is a very good photodetector, main problems as the high bias voltage operation and sensitivity to magnetic fields recommended the development of alternative detectors. For this reason, the solid–state detectors, built with semiconductor materials, were developed. Among the semiconductor materials, the silicon is the most widely studied and used to build photodetectors.
In general, a semiconductor photodetector principle of operation can be divided into three main steps [26]:

- an electron-hole pair is generated by an impinging photon;
- the carriers drift inside the detector volume, and multiply, via impact ionization process, if the detector is biased with enough voltage;
- the carriers are extracted generating a current signal.

The typical features of the silicon photodetectors are compactness, low bias voltage and the insensitivity to magnetic fields. Among the different solid–state photodetectors, the Silicon Photomultiplier (SiPM) gained more and more importance in the last years due to its good features (e.g. high internal gain, very high Photo–Detection Efficiency in NUV and visible wavelength ranges and single photon detection capability). The performance of this novel detector (developed and commercially available from the end of the last century) makes it a natural substitute of the classical PMT in many application.

In this thesis, the focus is on a SiPM technology manufactured in Fondazione Bruno Kessler (FBK, Trento, Italy) named NUV–SiPM. In the first chapter of the work, the SiPM detector will be reviewed introducing its principle of operation, noise sources and features. In the chapter two, particular attention will be paid to the FBK technology evolution in the last years and to the possible applications in which the detector could be an optimal solution. In the following chapter three, the set–ups for the characterisation in dark condition and for the Photo–Detection Efficiency measurements and the analysis procedures are shown. The last two chapters report the obtained results on different NUV–HD devices. Also, a model, describing the electric field inside the single SiPM cell, was developed to study the border effects and obtain information about the cell effective Fill Factor.

Chapter 1

Silicon Photomultiplier

1.1 Semiconductor Physics

The principle of operation of the semiconductor devices, thus also photodetectors, is based on the semiconductor physics. For this reason, main semiconductor physics features are briefly reported in this section. They are taken from [26].

The semiconductors can be single elements, typically belonging to the group IV of the periodic table, such as Silicon or Germanium, or compounds of many elements. Nowadays, known compound semiconductors have up to five different elements, such as the Gallium Indium Arsenide Antimonide Phosphide (GaInAsSbP). The semiconductor electrical properties are in between conductors and insulators. They are related to the particular energy–band structure of the semiconductors which have the conduction and valence bands separated by a small forbidden energy region (∼1 eV) called energy gap, or bandgap.

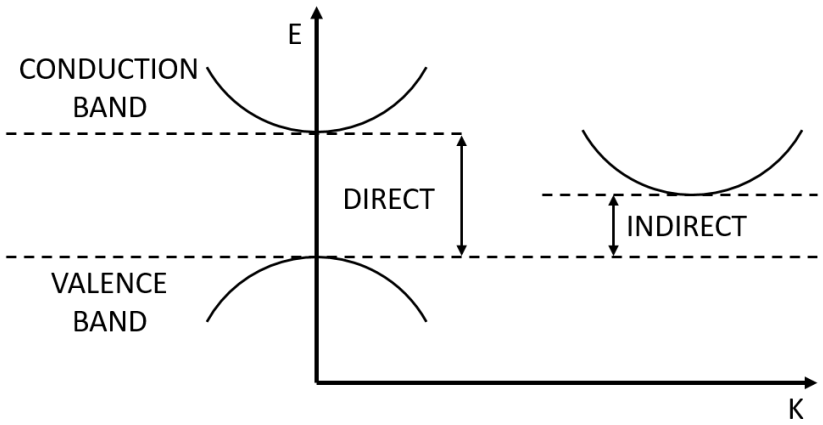

Figure 1.1: Energy–band structures of direct (left) and indirect (right) semiconductors.

The semiconductors are divided into two subgroups, direct and indirect, depending on the particular structure of the bands in the energy–momentum space. If the minimum in the conduction band is aligned with the maximum in the valence band, in the momentum space, the semiconductors are called direct (e.g. Gallium Arsenide, GaAs), else indirect (e.g. Silicon, Si) as illustrated in Figure 1.1.
Since in this thesis the focus is on the silicon photomultiplier, from now on, the silicon main properties will be reviewed. At room temperature, and under atmospheric pressure, the silicon bandgap is about 1.12 eV. This small value allows the promotion of electrons from the valence band to the conduction one, just due to the thermal agitation. The hole left in the valence band acts as a positive charge, moving in the opposite direction of the promoted electron, with electrical properties similar to those of the freed carrier. The intrinsic carrier concentration n_i (both electrons and holes) is about 10^{10} cm^{-3}. The number of electrons and holes are equal in intrinsic silicon. To increase the carrier concentration, the silicon is usually doped with donor and acceptor atoms (typically boron, phosphorus and arsenic). The doped silicon is called n–type or p–type if it is doped with donors or acceptors, respectively. In a n–type silicon the number of free electrons is larger than that of the holes, thus the electrons are the majority carriers. In a p–type silicon, the situation is the opposite, thus the holes are the majority carriers. The silicon photodetectors are based on the p–n junction, that is a device with two different doped parts, a p–type in contact with a n–type, as the one represented in Figure 1.2.

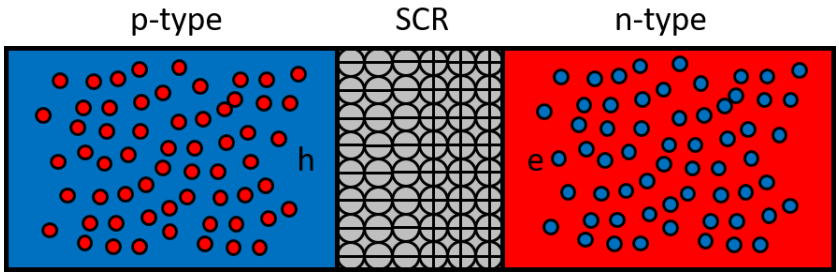

Figure 1.2: Scheme of a p–n junction. The grey volume is the space charge region (SCR). The fixed ions (large circles) and the free carriers, blue and red small circles for electrons and holes, respectively, are also shown.

In a p–n junction, there is a region in between the doped parts called space charge region (SCR) in which there are no free carriers because the electrons diffuse from the n–type to the p–type and the holes diffuse on the opposite direction. The remaining fixed ions create the so–called built–in electric field that reduces the carrier diffusion until an equilibrium between the diffusion current, due to the majority carriers, and the drift one, due to the minority carriers, moving in the opposite directions, is reached. Using an external power supply, it is possible to reduce or increase the SCR size, forward or reverse bias-

ing the junction, respectively. In the first case, the diffusion current increases; in the second case, the drift current increases. The IV plot of a typical p–n junction is pictured in Figure 1.3.

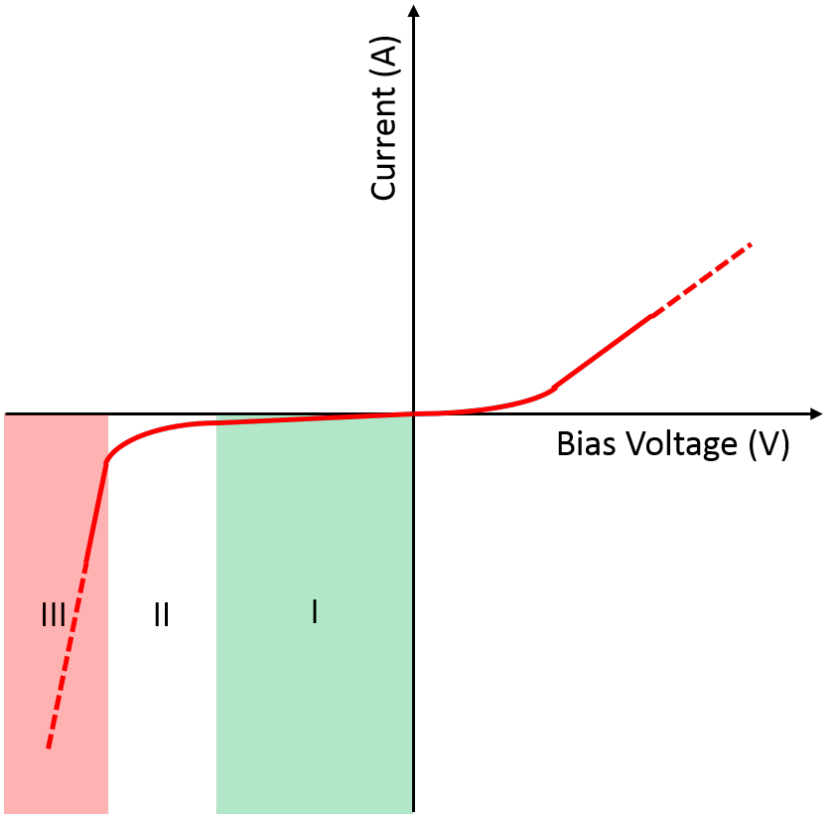

Figure 1.3: Typical IV plot of a silicon p–n junction. In the forward bias part, the current increases with the voltage after the knee point. Three different regions are highlighted with different colours in the reverse bias part. They are called linear, proportional and Geiger–mode, respectively. The plot is not in scale, the forward current is order of magnitude larger than the reverse one, at least up to the breakdown voltage is reached.

In the forward bias region, the current is almost zero until the bias voltage reaches the knee point (about 0.6 V for silicon) after which it rapidly increases. In the reverse bias part, three different regions are highlighted. In the region I, the electrical current slightly increases with the bias voltage, because the SCR size enlarges, favouring the drift current. This region was called linear in Figure 1.3, because the free carriers are collected without having the possibility to ionise the lattice, thus their number does not change during the drift (if no carrier recombine). In the region II, the current increases faster because the electric field is high enough to allow the impact ionisation process [26] to occur. This region was called proportional because, on average, every carrier produces a fixed number of secondary pairs and the final number of carriers is

proportional to the initial one. In the region III, the current suddenly increases of order of magnitudes because the electric field reaches a critical value, E_C, and the impact ionisation process produces an avalanche number of secondary pairs. The avalanche is self sustaining thus every carrier could ionise and produce secondary pairs in a never–ending process. The avalanche stops only if an external adopted quenching method is employed. If this occurs, the number of final carriers is always the same, within the statistical uncertainties, and independent from the number of the initial carriers that trigger the avalanche. For this reason, this region is called Geiger–mode. The bias voltage at which the electric field reaches the critical value is called breakdown voltage, V_{BD}.
The silicon photodetectors are based on p–n junctions biased at different voltages: the photodiodes are, typically, operated in the region I of Figure 1.3; the APDs are operated in the region II; the SPADs, and thus the SiPMs, are operated in the region III. In the following section, the differences between these photodetectors will be shown.

1.2 From the Photodiode to the Silicon Photomultiplier (SiPM)

The photodiode is the simplest silicon photodetector. It is a p–n junction (or p–i–n junction, in which i is an intrinsic, or poorly doped, silicon) reverse–biased with moderate voltage (also zero), very far from V_{BD}.
An impinging photon on a photodiode, with energy larger than the silicon bandgap (or, equally, with wavelength shorter than $\sim$1100 nm), can be absorbed creating an electron–hole pair. Due to the low applied bias voltage to the device, the impact ionisation process can not occur, and the photogenerated carriers have only two possibilities: they can drift through the depleted region, giving rise to an electrical current flowing in the device, that is the photodiode response to the incident optical power, or they can be reabsorbed. The probability for the photogenerated carriers to be reabsorbed depends on the carrier lifetime in silicon, related to the dopant level concentration and to the possible presence of defects or impurities. The probability for a photon to create a carrier pair that can originate a current signal is called quantum efficiency and it depends on the surface treatment of the device, on the active volume depth and on the photon wavelength.
When the photodiode is operated at a temperature different from the absolute zero, due to the thermal agitation, spontaneously generated electron–hole pairs can be observed. These carriers produce an electrical current. The surface leakage current must be summed up to the thermally generated one to obtain the so–called photodiode dark current, that is considered its noise. In general, a dark current in the order of a few pA per square millimetre is measured for a typical silicon photodiode. The impinging photons produce an

electrical current that sums up to the dark one. If the measured total current, when the photodiode is exposed to a light source, can be distinguished from the dark one, the electrical signal is considered statistically significant and the incident optical power can be measured. The statistical significance of the photodiode signal defines its signal–to–noise ratio and sets a sensitivity limit for the device. The minimum number of impinging photons that can give a significant device signal is, usually, thousands or more photons. Thus, this number is considered the photodiode sensitivity limit [26].

The most important and known silicon photodetector, operated with bias voltage belonging to the region II of Figure 1.3, is the Avalanche Photodiode (APD) [26, 27, 28, 29].
The APD structure is very similar to that of the photodiode, thus its principle of operation is very similar too. The different applied bias voltage to the APD causes the impact ionisation process to occur [30, 31, 32]. When the photogenerated electron–hole pairs move inside the APD high–field region, they create secondary pairs. This process is not infinite due to the friction losses inside the device, thus a finite number of final carriers are generated. The ratio between the number of final carriers over the number of initial ones is the gain of the device. Typical gain values for commercial APDs can be as high as 10^3 [33, 34]. Since the gain of the device is related to a stochastic process, it has statistical fluctuations. The gain fluctuations origin the so–called Excess Noise Factor, that, in general, increases with the gain.
The APD also suffers of the dark current as the photodiode but its surface leakage current component is not multiplied because the carriers do not pass through the high field region. Only the thermally generated current in the substrate is multiplied by the impact ionisation process, thus the device noise is not very different from that of a photodiode with equal area but the signal–to–noise ratio can be made larger by a proper choice of the operating conditions [34]. For this reason, the APD has a lower sensitivity limit than the photodiode, several tens to hundreds of photons, but it can not be considered a single photon detector too.

The problem to give the single photon detection capability to a silicon photodetector was solved increasing the bias voltage over the breakdown voltage V_{BD}, operating a device in the region III of Figure 1.3. These devices are called Single Photon Avalanche Diodes (SPADs), also Geiger–mode Avalanche Photodiodes (G–APDs) [35, 36, 37, 38, 39, 40, 41, 42, 43, 44, 45, 46, 47, 48].
The SPAD principle of operation is similar to that of an APD: an impinging photon can be absorbed in silicon and create a primary electron–hole pair; the photogenerated carriers, moving inside the high–field region, create secondary pairs. The larger bias voltage than that of an APD causes in the SPAD a never–ending production of secondary pairs. For this reason, a quenching

method must be employed to stop the production and collect the device signal.
Usually, the SPADs are divided into two categories, depending on the adopted quenching method: active and passive quenched. The active quenched SPADs employ an integrated circuit with a fast discriminator that detects the avalanche production of pairs inside the device. Then, the discriminator provides a digital output pulse for timing applications while a proper circuit quickly reduces the device bias voltage below V_{BD}, stopping the production of further secondary pairs. When the avalanche is stopped, the bias voltage is quickly restored to the operating condition to reduce the device dead time by a reset circuit [35, 40, 45, 48, 49, 50, 51]. The quenching circuit is, usually, built on wafer scale along with the SPAD junction. A simplified scheme representing an active quenched SPAD is given in Figure 1.4.

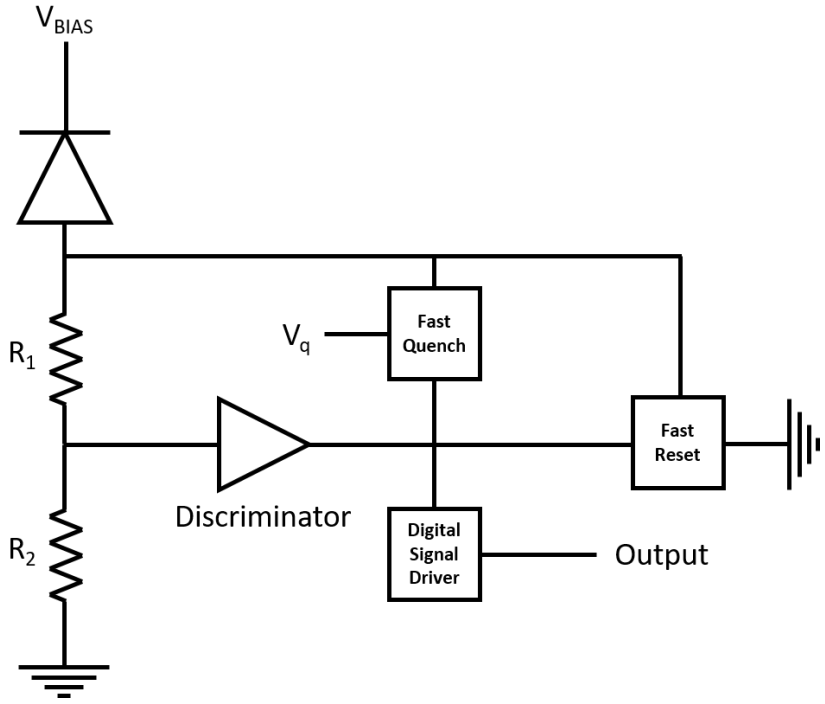

Figure 1.4: A simplified scheme of an active quenched SPAD is drawn. The junction is represented with a diode symbol. The discriminator, detecting the avalanche development in the junction, sends its output to trigger a digital pulse generator for timing applications and activate the fast quenching circuit to reduce the voltage across the junction below the breakdown one. Then, after the end of the avalanche, the reset circuit restores the device to the operating bias voltage.

In the scheme, the main components of the active quenching concept are drawn (the photodetector junction, represented by a diode symbol, the discriminator, the fast quenching circuit and the reset one). The passive quenched SPADs are simpler devices that employ a resistor *in series* with the junction to stop the

avalanche production of secondary pairs. The electrical current, produced by the primary and secondary pairs in the high–field region, flowing in the circuit, causes a voltage drop on the resistor that reduces the junction effective bias voltage below V_{BD}. This condition forbids the generation of further secondary pairs. After the avalanche is stopped, and thus the current flowing in the resistor decreases, the voltage across the junction is restored to the operating condition by the external power supply. The junction bias voltage is restored as the voltage in a capacitor in a series RC circuit with a typical time constant:

$$\tau = R_q C_D \tag{1.1}$$

in which R_q is the series quenching resistor value and C_D is the equivalent capacitance of the junction [35, 40, 45, 48, 52]. The series resistor is usually built on wafer scale along with the SPAD junction. A scheme representing a passive quenched SPAD is shown in Figure 1.5.

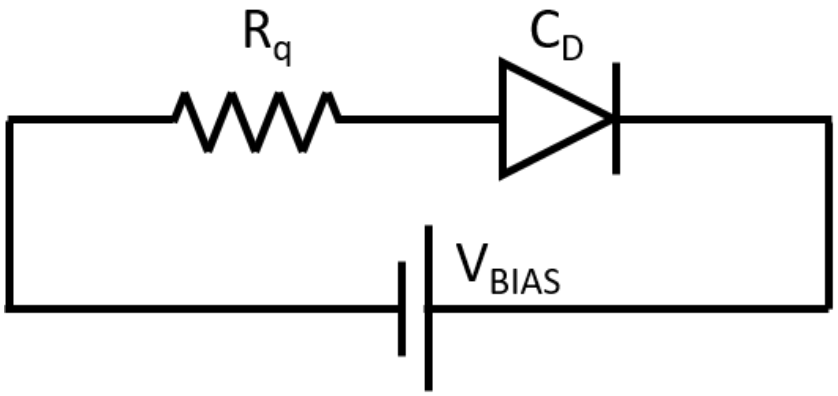

Figure 1.5: A scheme of a passive quenched SPAD is shown. As in Figure 1.4, the junction is represented with a diode symbol. The current flowing in the circuit causes a voltage drop on the resistor R_q reducing the effective bias voltage across the junction below V_{BD}.

There are two main differences between the active and passive quenched SPADs:

- the signal duration, typically longer in the passive quenched devices due to the large value of the series resistor that increases the time constant;
- the fill factor, that is the device active to total area ratio, typically larger in the passive quenched SPADs because the absence of the needed transistors by the circuits in the active quenched devices.

The signal–to–noise ratio of a SPAD, defined as in the case of the APD, allows to consider the device a single photon detector. But its signal is not correlated to the incoming optical power because the number of collected carriers is always

the same, within the statistical fluctuations, independently from the number of impinging photons and primary photogenerated pairs. The SPAD capability to detect the single photon was granted at the price to lose a proportional signal to the incoming optical power. Thus, it is considered a photodetector different from the photodiode or the APD and can be used only in particular applications in which the number of incoming photons is not requested but their presence or not is a needed information. Its capacity to be only in two states, triggered or not, makes the SPAD a digital detector.
Even if the single photon detection capability is an important feature and the SPAD was the only silicon photodetector having it, the impossibility to give information about the number of photons was a major limit in many applications. This limit was exceeded in past years connecting many SPADs in parallel in a matrix. These matrices are usually called Silicon Photomultipliers (SiPMs), or Multi–Pixel Photon Counters (MPPCs) [53, 54, 55, 56, 57, 58, 59, 60, 61, 62]. This thesis focus on a SiPM technology built with passive quenched SPADs, thus in the next section a detailed description of such a device will be given.

1.3 Silicon Photomultiplier

The Silicon Photomultiplier (SiPM) is a pixelated photodetector with identical independent cells connected in parallel. Every cell is a passive quenched SPAD with a series resistor, thus the SiPM is reverse–biased with voltage larger than V_{BD}. Its output is the sum of the fired cell signals, thus, even if every SPAD has a digital response, the SiPM is an analogue photodetector with signal proportional to the number of impinging photons. The SiPMs are usually built on silicon wafers with thin epitaxial layers.
As the other silicon photodetectors, photodiodes and APDs, the SiPM features are compactness, ruggedness, insensitivity to the magnetic fields and low bias voltage. In addition to these properties, the SiPM inherits other features from the SPAD including the high internal gain, the single photon detection capability, a very good timing resolution and a very high Photo–Detection Efficiency (PDE).

In Figure 1.6, the electrical scheme of a typical SiPM with n cells is drawn. Every SiPM cell is pictured and numbered inside a dashed line. Along with the main elements of the cell (the junction, represented with a diode symbol, and the quenching resistor, R_q), the parasitic terms are also drawn (the junction resistor, R_D, and the quenching capacitance, C_q). Also the capacitance of the metal grid above the cells, C_g, is indicated, in parallel with all the cells.

Two different types of SiPMs can be built, called p–on–n or n–on–p, depending on what doped part is directly exposed to the incoming light, p–type or n–type, respectively. A very simplified cross–section of a cell of the two SiPM types are drawn in Figure 1.7. In the picture, the doped silicon implants and

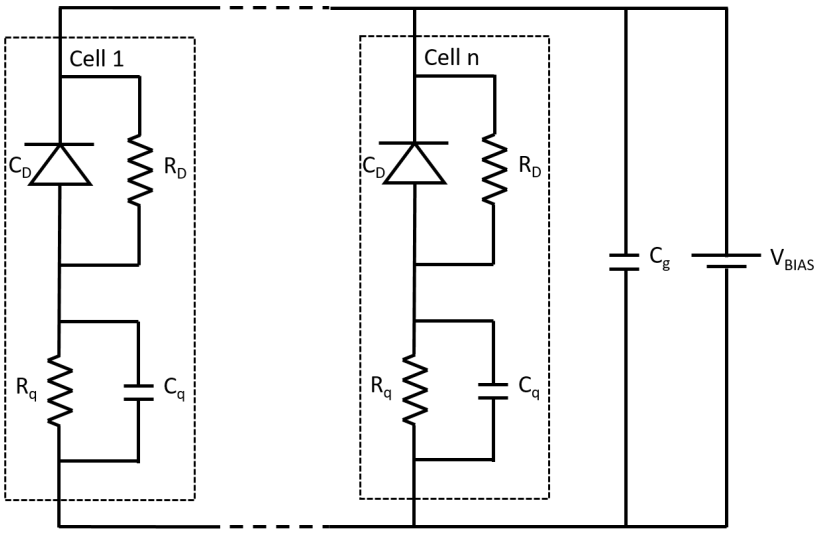

Figure 1.6: Electrical scheme of a typical SiPM. The single cell is highlighted inside a dashed line and numbered from the first to the last, the n–th. Inside every cell, the junction, represented as before with a diode symbol, C_D, and the quenching resistor, R_q, are drawn along with the parasitic junction resistor, R_D, and the stray quenching capacitance, C_q. C_g is the capacitance due to the metal grid covering the cells.

wafer substrates and epitaxial layers are shown along with the anti–reflective coatings (ARC). Other elements (e.g. the series resistors and the trenches or the implants separating the cells) are not indicated in the Figure.

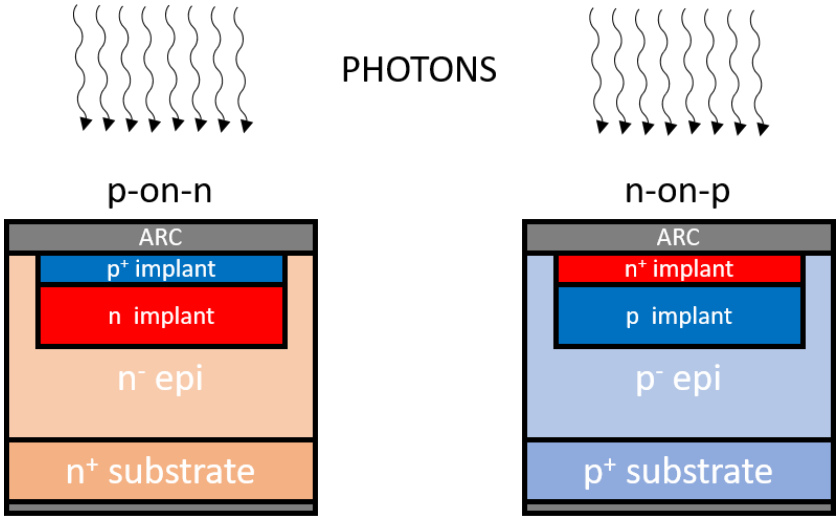

Figure 1.7: Schematic cross–sections of a cell of a p–on–n SiPM (left) and a cell of a n–on–p one (right) are drawn. The implants, the epitaxial layers and substrates are indicated along with the anti–reflective coatings (ARCs).

The two SiPM types have different PDE spectra due to the silicon absorption

depth of photons, that is wavelength dependent, and to the electron and hole triggering probabilities in silicon. A more detailed description of the PDE spectra difference between the two SiPM types will be shown in the section 1.3.2.

As mentioned in the previous section 1.2, every SPAD, or single SiPM cell, can be approximated to a series RC circuit. For this reason, after the avalanche is quenched, the cell restores its operating condition exponentially, with a proper time constant, indicated by the equation (1.1). Considering also the parasitic contributions, the total cell capacitance and resistance can be written as:

$$C = C_D + C_q, \quad R = R_q + R_D \tag{1.2}$$

in which all the terms are defined as before [63, 64]. The R_D value is very small compared to the R_q one, thus it is usually neglected in the equation (1.1), while C_D and C_q can be similar and must be always taken into account.
In Figure 1.8, the single cell signal of a 1x1 mm^2 SiPM with cell pitch equal to 25 μm, produced in Fondazione Bruno Kessler (FBK, Trento, Italy), is shown. The SiPM used for the previous signal plot is p-on-n type. It has a breakdown voltage of about 26 V at room temperature. On the picture title, the working bias voltage is reported, expressed as overvoltage (difference between the applied bias voltage and the breakdown one).

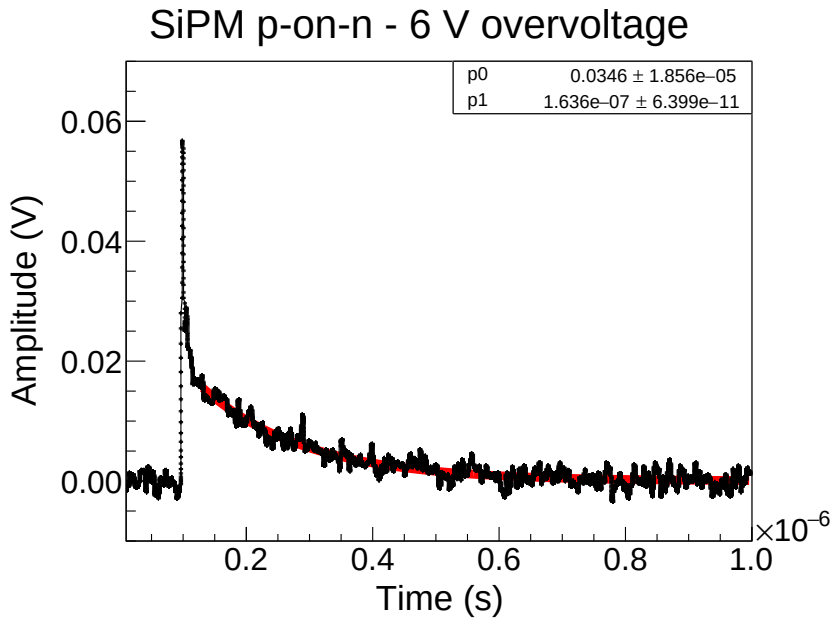

Figure 1.8: A single cell signal of a 1x1 mm^2 FBK SiPM with 25 μm cell pitch is shown. On the picture title, the SiPM type and overvoltage are indicated. The fast peak is visible as a single exponential function used to fit the recharge part of the signal.

The fast peak has a rise time very small that can be approximated by the law (1.3) [63]. A red single exponential function, expressed by the law (1.4), is used to fit the recharge part of the signal.

$$\tau_{rise} = (C_D + C_q)R_S \tag{1.3}$$

$$F = (p0)exp(-\frac{t}{p1}) \tag{1.4}$$

The single exponential fit function shows a perfect agreement with the signal, as expected from the series RC circuit model.

From the cell capacitance, the SiPM gain can be calculated. It is the average number of carriers produced during the firing of a cell and it can be expressed by the equation (1.5).

$$G_{SiPM}(V) = \frac{Q_{cell}}{q_e} = C_{cell}\frac{V_{BIAS} - V_{BD}}{q_e} \tag{1.5}$$

In the equation (1.5), Q_{cell} is the total charge at the cell electrode, equal to the product of the cell capacitance, C_{cell}, by the overvoltage and q_e is the electron elementary charge. From the equation (1.5), it is clear that the SiPM gain is not a constant, but it is voltage dependent.

Since a SiPM is a matrix in which every cell is built with the same technological process, the SPAD signals are expected to be equal. This can be qualitatively shown acquiring many SiPM signals in a oscilloscope persistence mode. In Figure 1.9, a similar acquisition is reported. In this picture, many bands are visible. Every band consists of a large number of superimposed signals having very similar amplitude and shape. Each band corresponds to an increasing number of fired cells. The smaller amplitude band corresponds to the single cell signals. The presence of a band structure and the equal separation between the bands confirm the uniformity of the cells forming the SiPM. A quantitative way to demonstrate the cell uniformity can be shown integrating the SiPM signals over time, obtaining a SiPM charge spectrum. An example of this charge spectrum is represented in Figure 1.10. In such a spectrum, many peaks are visible, each one corresponding to the integration of a different number of fired cells. The amplitude separation between bands becomes a charge difference in a similar spectrum. The first peak, often called pedestal, corresponds to the integration of the baseline, thus no SiPM signal.
If the integration time is properly chosen, at least equal to the signal duration, the charge separation between two consecutive peaks is related to the gain of the SiPM by the equation (1.6).

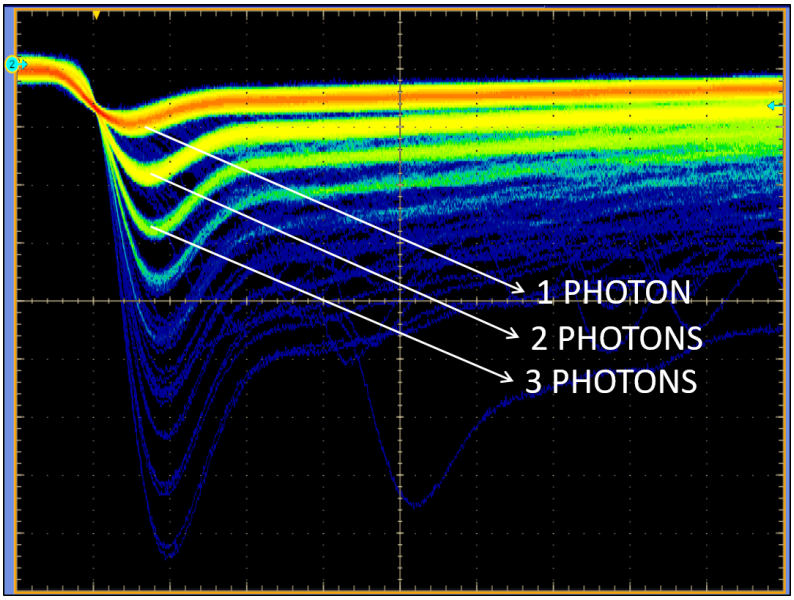

Figure 1.9: A oscilloscope persistence acquisition of a SiPM signals is shown. Different bands are visible, each one corresponding to a different number of SiPM fired cells. The signal bands are equally separated. The presence of the band structure and the equal separation between the bands are clues of the expected uniformity of the cells.

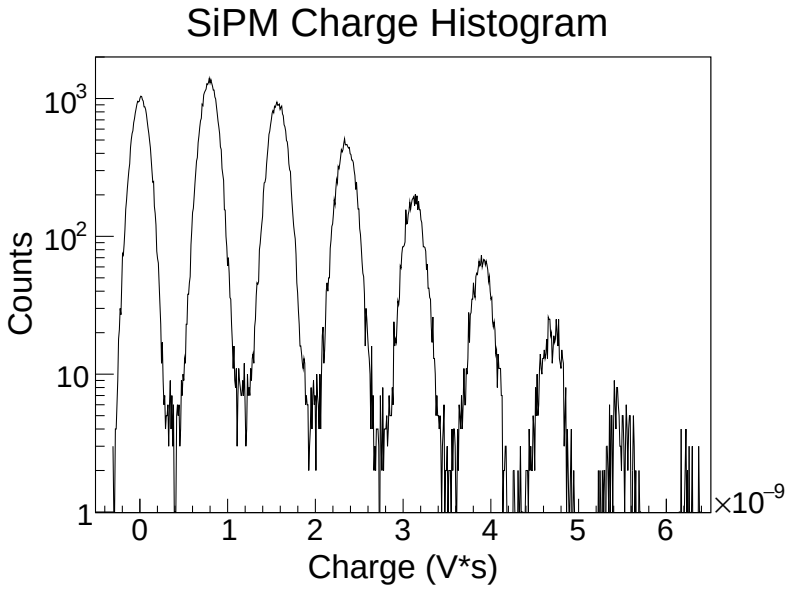

Figure 1.10: A typical charge spectrum of a SiPM obtained integrating the device signals over time in semi–logarithmic scale is drawn. The first peak has an average charge equal to zero, it is called pedestal and represents the integration of the baseline. The other peaks represent the integration of an increasing number of fired cells.

$$G_{SiPM} = \frac{A_n - A_{n-1}}{G_{Ampl} \cdot Z_{OSC} \cdot q_e} \tag{1.6}$$

A_n and A_{n-1} are the charge of the n–th peak and the precedent one, respectively, G_{Ampl} is the amplifier gain, if used, Z_{OSC} is the oscilloscope input impedance, set during the acquisition, and q_e is the electron elementary charge. The equations 1.5 and 1.6 allow to determine the cell gain, but, since the cell capacitance is not easily known, the last equation is a better operative way to calculate it.

The cell gain is also temperature dependent because the breakdown voltage is not constant with the temperature. In the section 1.1, the definition of the breakdown voltage was derived from the IV plot. To reach the critical value and allow a self–sustaining avalanche, every carrier must gain enough energy from the electric field to allow the impact ionisation process to occur. The energy acquired from the electric field can be related to the mean free path of the carrier between two consecutive scatterings. If this path is sufficiently long, the carrier can acquire the required energy to ionise. At a higher temperature, the average atom lattice vibration increases and the mean free path reduces. For this reason, the breakdown voltage is directly proportional to the temperature, as shown in Figure 1.11, at least in a wide temperature range around room temperature.

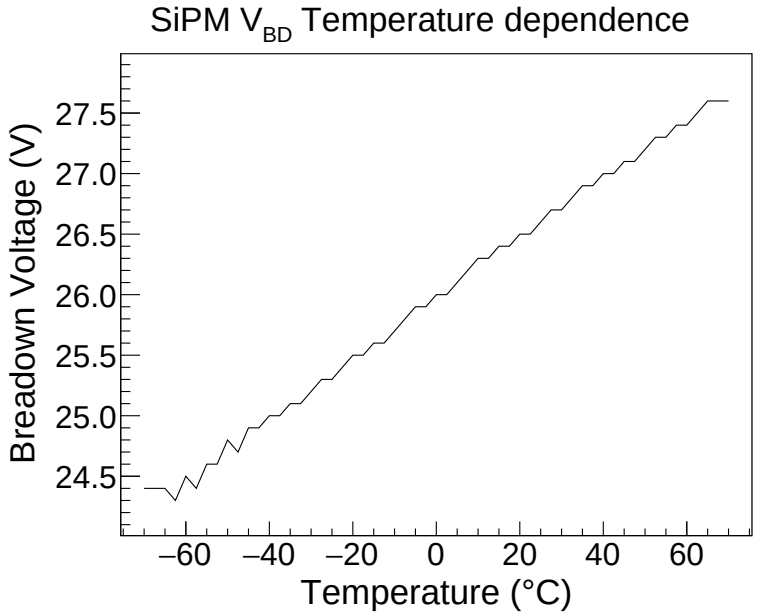

Figure 1.11: The measured breakdown voltage–temperature relationship for a FBK SiPM. The direct proportionality is evident in the temperature range investigated.

In the last years, different manufacturers improved the performance of their SiPMs increasing the cell density with the production of smaller cells. Cell

pitches down to 10 μm are now available [65, 66]. The cell density is a very important parameter in applications in which the devices must detect a high level photon flux (e.g. SiPMs used as readout detectors of scintillating crystals for medical applications and particle physics experiments [6, 67, 68]). In all of these applications, a large number of incoming photons is expected, thus the finite cell number could be a problem because the detector suffers from the saturation by the high level light flux. Under the hyphothesis that the impinging photons follow a spatial Poisson distribution, and that they have a negligible arrival time distribution compared to the typical cell recharge time, the probability that two or more photons income in the same cell, called P(2+), causing a linearity loss due to the discussed digital response of the SPAD, can be calculated using the equation (1.7).

$$P(2+) = 1 - P(0) - P(1) = 1 - e^{-\mu}(1 + \mu) \tag{1.7}$$

In the previous equation, P(0) and P(1) are the probabilities to have 0 or 1 photon per cell, respectively, and μ is the average number of photons per cell, calculated as the total number of impinging photons over the total number of SiPM cells. In Figure 1.12, the value P(2+) for SiPMs having a cell pitch of 100, 50, 25 and 10 μm is drawn as a function of the density of incoming photons, ph_d.

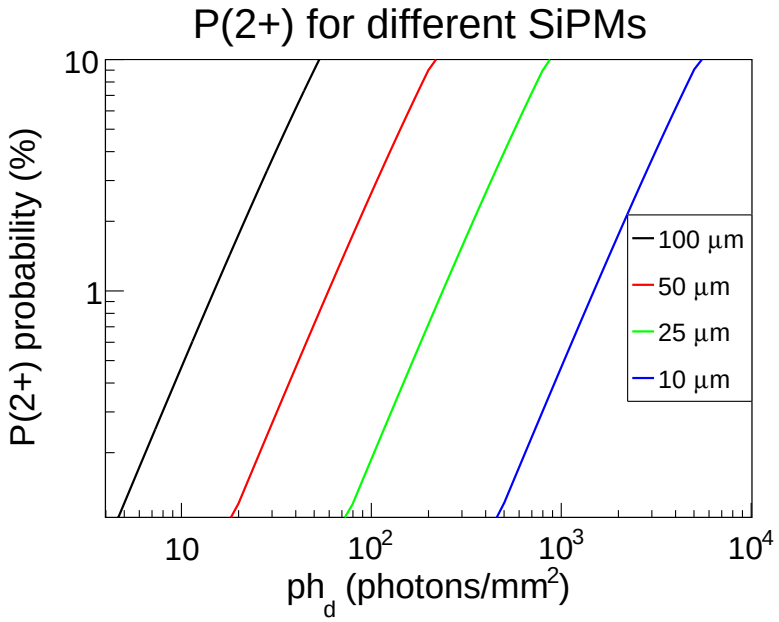

Figure 1.12: The probability P(2+) is drawn in a logarithmic scale for SiPMs having different cell pitches, reported in the legend, as a function of the incoming photon density, ph_d. The probability P(2+) increases with the cell pitch and the photon density, as expected.

P(2+) reduces with the photon density, and thus with μ, but it is never zero. For this reason, the smaller cell SiPMs have lower non linearity problems, but it is impossible to build a segmented detector with a perfectly linear response. If a critical value is chosen to discriminate from linear response detector and the others, e.g. 1 %, the larger cell pitch SiPMs reach this value at a very small number of impinging photons. The 100 μm cell pitch reaches this value with just 15 photons per square millimetre, the other cells with 60, 238 and 1490, respectively. The equation (1.7) can be used in every application in which the incoming photon statistics respects the distribution conditions above written.

The small cell devices become common nowadays also because they have a lower noise, in particular the correlated noise is influenced by the cell pitch. This argument will be explained in the following subsection. In the last part of this chapter, the PDE will be investigated.

1.3.1 SiPM noise

The SiPM, as the other silicon photodetectors, suffers from the dark current. The surface leakage current contribution to the dark current is usually negligible because it is not multiplied, as just written for the APD and the SPAD. The current originating from thermally–generated carriers in the bulk is the dominant contribution to the noise of the SiPM. Due to the presence of high electric fields inside the device, carrier generation through the tunneling process can also happens in the SiPM, but this contribution is, usually, negligible at room temperature.
The generation and recombination processes are well known in semiconductor physics. These processes are related to the carrier lifetimes, that are inversely proportional to the doping concentration. However, in indirect semiconductors, like silicon, the dominant generation mechanism is caused by the presence of defects (traps) introducing energy levels within the bandgap. The process can be analysed using the Shockley–Read–Hall statistics. In this case, the generation rate U for a single–level trap can be written as:

$$U = \frac{\sigma_p \sigma_n v_{th} N_t n_i}{\sigma_p[1 + \frac{p}{n_i}] + \sigma_n[1 + \frac{n}{n_i}]} = \frac{n_i}{\tau_g} \tag{1.8}$$

in which σ_{p} and σ_{n} are the hole and electron capture cross–sections, respectively; $\mathrm{v_{th}}$ is the thermal velocity of the carriers; $\mathrm{N_t}$ is the density of the trap level in the energy bandgap; p, n and $\mathrm{n_i}$ are the hole, electron and intrinsic concentrations, respectively. τ_{g} is the carrier generation lifetime, expressed as:

$$\tau_g = (1 + \frac{n}{n_i})\tau_p + (1 + \frac{p}{n_i})\tau_n \tag{1.9}$$

It is related to the hole and electron lifetimes, τ_{p} and τ_{n}, respectively, and

it is inversely proportional to the trap density. It can be demonstrated that the most effective traps are the mid–gap levels in the energy bandgap, thus elements as copper, gold and iron are very dangerous impurities, whose introduction should be carefully avoided during the silicon devices fabrication [26]. When an electron–hole pair is thermally generated in the high–field region of a SiPM cell, these carriers can ionise and trigger an avalanche in the cell. The detector signal is identical to the one produced in the same cell by a photo-generated pair by an incoming photon. The thermal generation of carriers is an equivalent process to the photovoltaic effect.

In practical applications, the SiPM signal is analysed, after current–to–voltage or current–to–charge conversion, by acquiring only the part of the signal larger than a given threshold. The detector noise consists of signals larger than the imposed threshold but not correlated with impinging photons. The total number of spontaneous SiPM signals can be directly estimated varying the threshold level. This acquisition must be performed with a chosen time gate, used as dead time of the system, to not retrigger the same signal due to the noise fluctuations. The result of a similar analysis is a so–called staircase plot, as the one reported in Figure 1.13.

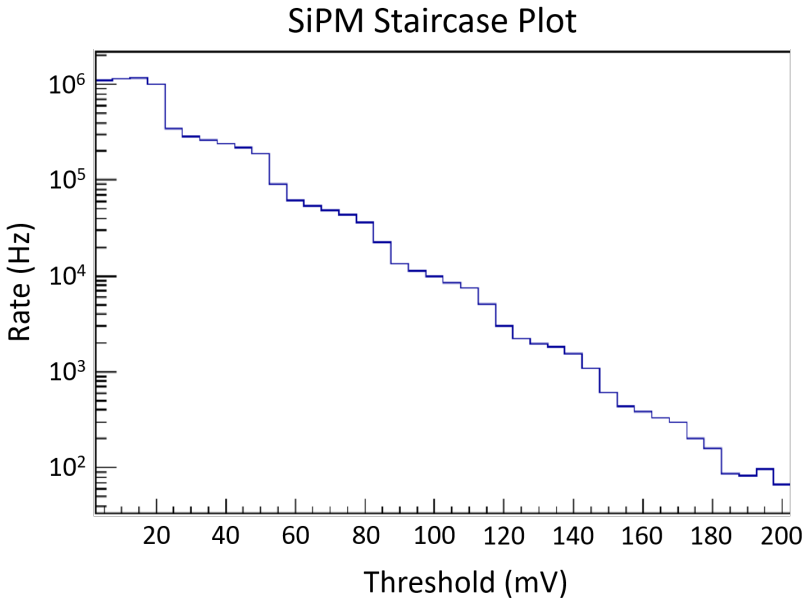

Figure 1.13: A staircase plot of a SiPM, obtained acquiring the detector signals varying the threshold level, is shown in a semi–logarithmic plot.

In a staircase plot, many plateau, or "stairs", are visible varying the threshold. The abrupt variations in the measured rate corresponds to the amplitude of an increasing number of firing cells (e.g. in the previous plot, every ∼30 mV a variation is observed because it corresponds to the average amplitude of a SiPM cell, in the given measurement and temperature conditions, thus, at

higher thresholds, only signals produced by a larger number of fired cells are acquired). Fixing the threshold at half the amplitude of the single cell signal, the average rate of the total noise can be expressed as $R_{0.5}$. In the same way, $R_{1.5}$ can be defined as the rate of every signal having an amplitude larger than at least one and an half the single cell signal. From the $R_{0.5}$ and the signal duration, the rate $R_{1.5}$ could be calculated and compared with the direct measurement. The equation to perform this estimation is:

$$R_{1.5} = (\frac{R_{0.5}}{N_{pixel}})^2 \Delta t \frac{N_{pixel}(N_{pixel}-1)}{2} \tag{1.10}$$

in which N_{pixel} is the number of the SiPM cells and Δt is the time gate in which two firing cells produce a signal larger than the imposed threshold. This time can be estimated neglecting the rise time of the SiPM signal as:

$$\Delta t = -\tau ln(\frac{1}{2}) \tag{1.11}$$

due to the typical exponential recharge of a cell. A comparison between the direct measurement of the rate $R_{1.5}$ and an estimated value using the previous equation (1.10) as a function of the overvoltage is shown in Figure 1.14. This comparison shows the result obtained with the SiPM just used to perform the staircase plot of Figure 1.13.

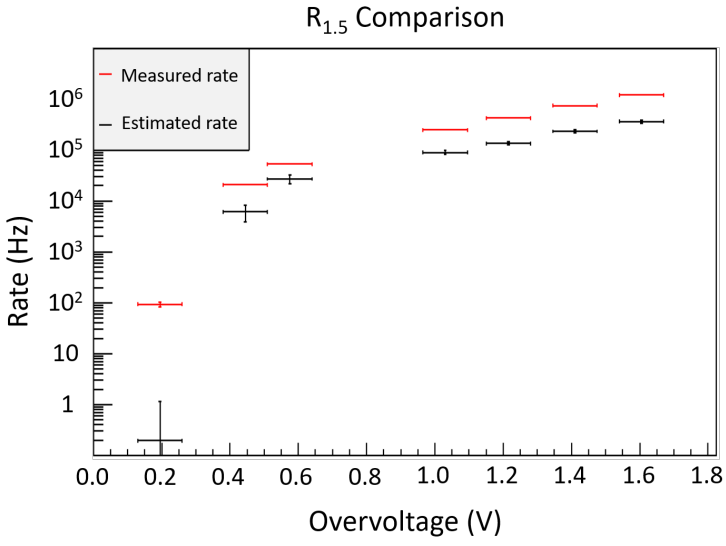

Figure 1.14: A comparison between the $R_{1.5}$ directly measured and estimated using the equation (1.10) as a function of the overvoltage is shown in a semi–logarithmic plot. The comparison is performed using the same SiPM just measured for the staircase plot shown in Figure 1.13. The estimated value is always smaller than the directly measured one.

The difference between the direct measurement and the estimation is evident. In particular, the direct measured $R_{1.5}$ is always larger, implying that the above described noise is not the only noise source. The first noise contribution, due to the spontaneous generated electron–hole pairs, is called primary noise, or Dark Count Rate (DCR). This rate increases with the overvoltage because the triggering probabilities of the carriers, both electrons and holes, increase with the overvoltage. The second noise source is called correlated noise. Such an event is possible only if a primary cell is fired, either by an incoming photon or due to the spontaneously generated pairs. The correlated noise consists of two different types: Afterpulsing (AP) and optical Cross–Talk (CT).
During the avalanche development in a cell, the secondary carriers move inside the high–field region to the electrodes. During this motion, some of the carriers can be trapped by the mid–gap energy levels. The release of these carriers follow an exponential distribution governed by the carrier lifetimes τ_p and τ_n. When the release happens, the carrier has a non–zero probability to retrigger the same cell. This probability increases with the elapsed time from the primary avalanche development. A similar event, called afterpulsing, is reported in Figure 1.15.

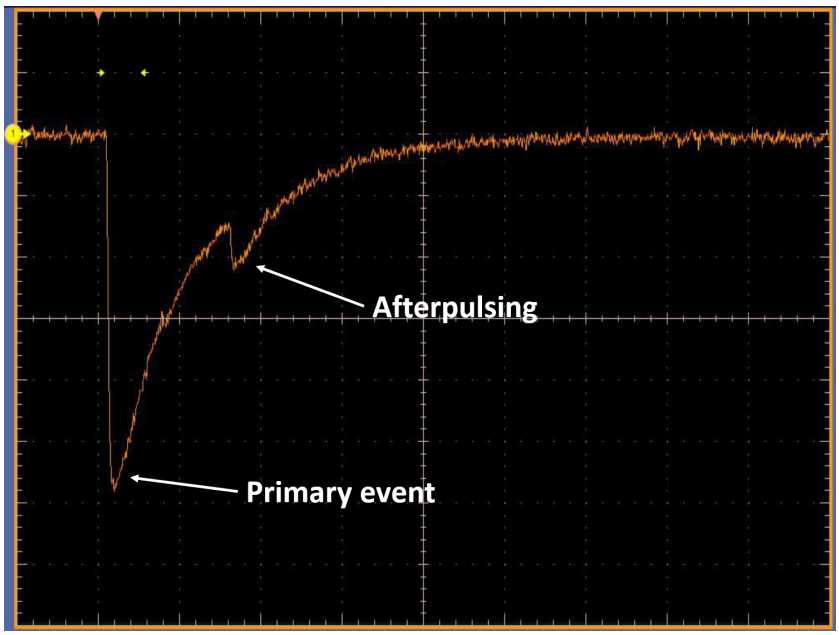

Figure 1.15: A typical afterpulsing event is shown. The release time was about one third of the total signal duration, causing a lower cell effective bias voltage with respect to the operating condition. For this reason a lower amplitude is observed for the AP event.

If it occurs during the recharge of the cell, the AP event has an amplitude lower than a primary one, because the effective bias voltage and the gain are lower. The lower bias voltage also causes a lower carrier triggering probability

(this probability will be later discussed in the section 1.3.2), thus not every released carrier can retrigger the cell.
The AP probability depends on three factors, the capture cross–section of the traps, the number of carriers inside the volume and the triggering probabilities of the carriers. The first is independent from the overvoltage, but the other two quantities increase with the overvoltage, thus, the AP probability increases too. The low triggering probability and the typical reduced number of carriers generated by an AP event make an AP chain a very rare phaenomenon. When a cell is retriggered, the probability to have a second AP on the tail of the first one is much lower than the first probability.
During the avalanche development, the carriers can also recombine emitting secondary photons. These photons can escape from the detector or be absorbed in the active volume of an adjacent cell, then triggering a new avalanche. A similar event is called optical cross–talk and an example is shown in Figure 1.16.

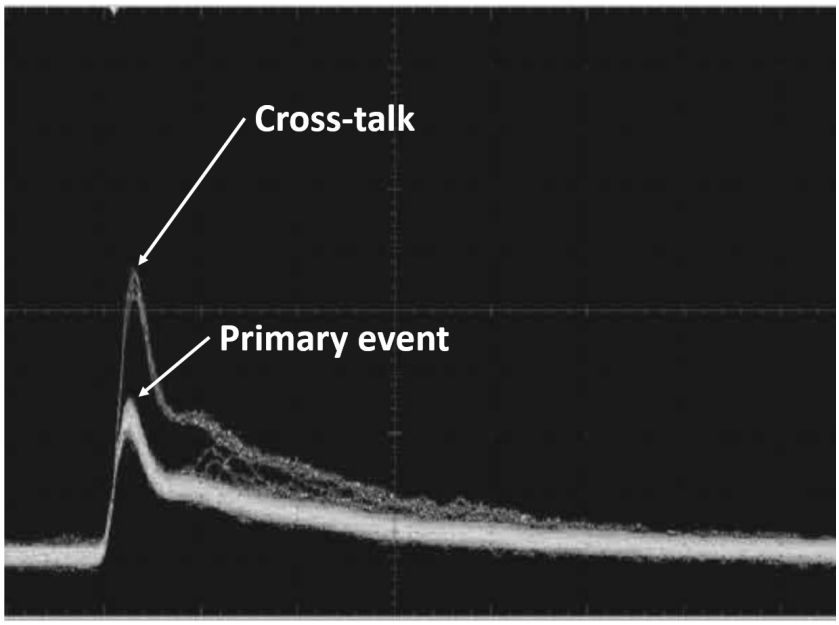

Figure 1.16: A persistence oscilloscope acquisition of a SiPM signals is shown. The optical cross–talk event are the larger amplitude signals. Since the second cell is triggered in its operating bias condition, its signal is identical to the primary event and the detector signal is the sum of the two cell signals. This signal has twice the amplitude of the single cell one.

The optical CT event has a double amplitude because it is the sum of two cell signals, both triggered in the operating bias condition.
The probability to have a CT event depends on four factors: the availability of the adjacent cell, the number of emitted photons, the probability that a photon is absorbed in one the available cells and the triggering probability of

the carriers. The number of emitted photons and the triggering probability are voltage dependent, thus also the CT probability increases with the overvoltage. If the cell availability is considered constant, a CT event has the same probability to generate a second event than the primary one. This type of noise can originate a chain with a higher probability than the afterpulsing one. For example, in Figure 1.9, up to nine different bands are visible, mainly corresponding to CT chain events.

The optical CT can be divided into two subgroups, direct and delayed events. A perfect explanation of these two type of events is given in [69], from which the Figure 1.17 is taken. The direct CT events (DiCT) happen when a photon is absorbed in the high–field region of the adjacent cell, while the delayed events (DeCT) are caused by photons absorbed in the substrate or epitaxial layers of the adjacent cell. Since in this second case the produced carriers drift with a limited velocity, the triggering of the second cell happen with a measurable delay with respect to the primary event. This delay can be, in general, in the order of nanoseconds or tens of nanoseconds.

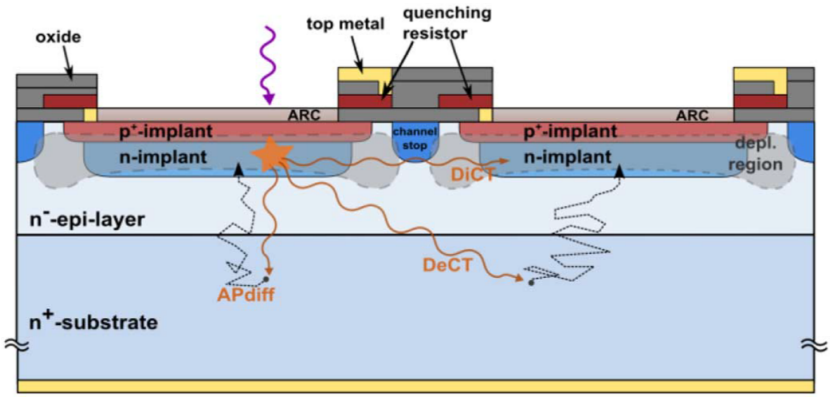

Figure 1.17: Picture taken from [69]. In the above picture, two adjacent cells of a p–on–n SiPM are shown. The correlated noise sources are indicated with acronyms: APdiff, DiCt and DeCT for diffuse AP, direct CT and delayed CT, respectively. The orange lines are the secondary photons, the dashed black lines are the free carriers.

The DeCT and the AP events are called together delayed correlated noise. Even if the delay can be identical, the signals are very different and can be distinguished. Actually, the DeCT events have always amplitude larger than the primary events, and, thus, larger than the AP ones.

Every correlated noise component increases the charge of the SiPM output signal. A CT event, direct or delayed, increases the total charge output by the amount of a single cell one, while an AP event increment is not fixed. It can be a continuous amount of charge between ∼zero and a single cell one depending on the delay time of the afterpulsing signal with respect to the primary one. The charge increment due to the correlated noise is defined as Excess Charge Factor (ECF) [70, 71]. This factor represents the average amount of charge

increment suffered from the single cell signal due to the correlated noise components. For this reason, it can be defined as the ratio between the output current of a SiPM in dark condition, I_{SiPM}, and the equivalent current of the SiPM in the same condition only due to the primary noise events, as shown in the equation (1.12):

$$ECF = \frac{I_{SiPM} - I_{LEAK}}{I_{DCR-SiPM}} = \frac{I_{SiPM} - I_{LEAK}}{q_e \times G_{SiPM} \times DCR} \tag{1.12}$$

in which I_{LEAK} is the surface leakage current of the device, q_e, G_{SiPM} and DCR are defined as before.

All the noises are voltage dependent, as written, because they depend on the triggering probability of the carriers. In the following and last section of this chapter, the triggering probability will be exposed because it is a fundamental part to understand the PDE of the detector.

1.3.2 Photo-Detection Efficiency

Among the various performance parameters of a SiPM, the Photo–Detection Efficiency (PDE) is one of the most important. It is the probability that an incoming photon can trigger a self–sustaining avalanche in a SiPM cell, causing a detector signal. Usually, it is possible to directly estimate it from a simple ratio between the impinging photons and the detected ones, as in the equation (1.13):

$$PDE = \frac{N_L - N_D}{Ph_I} \tag{1.13}$$

in which N_L and N_D are the detector pulses in light and in dark, respectively, and Ph_I is the number of impinging photons.
The PDE is a combined probability depending on three factors. It is defined by the equation (1.14).

$$PDE(V, \lambda) = FF \times QE(\lambda) \times T_P(V, \lambda) \tag{1.14}$$

in which FF is the cell Fill Factor, $QE(\lambda)$ is the device Quantum Efficiency and $T_P(V,\lambda)$ is the device triggering probability. The FF is the ratio between the active area and the total one of a cell (in case of square cell, the total area is equal to the square cell pitch); the $QE(\lambda)$ is defined as in the photodiode; the $T_P(V,\lambda)$ is the probability for an electron–hole pair, photogenerated by a photon with wavelength equal to λ, to trigger an avalanche operating the detector at an overvoltage equal to V .

The FF can be obtained by the detector layout and is considered a constant in the equation (1.14).

The QE(λ) is the product of two probabilities: I) the probability for a photon to be transmitted through the anti–reflective coating (ARC) on the detector surface; II) the probability for a photon to create a carrier that can reach the high–field region before the reabsorption. The first probability is related to the photon transmission, as a function of wavelength, of the ARC, grown on the device surface. The optimisation of the ARC transmission, to improve the performance of the device in a specific application, is a very important process involving many aspects: the photon spectrum to detect, the angle of incidence of impinging photons, the refractive index of the surface material (air, water, scintillator crystals and liquids). The ARC consists of many layers and its transmission is determined by several parameters: order of different layers, number and constituting materials, thickness of every layer are some of them. The second probability is related to the absorption probability of photons in silicon. As well known, this probability is a decreasing exponential governed by the absorption coefficient of photons in silicon. In Figure 1.18, the absorption depth, inverse of the absorption coefficient, as a function of wavelength in silicon, is plotted.

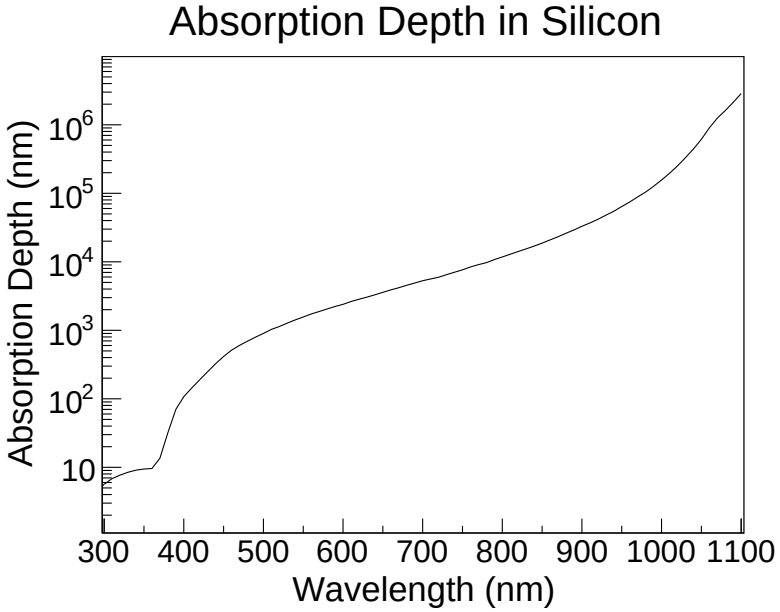

Figure 1.18: The absorption depth plot as a function of wavelength of photons in silicon is drawn in a semi–logarithmic plot. The absorption depth increases with wavelength by five order of magnitudes from NUV to NIR region.

The absorption depth increases with the wavelength. It has a value lower than $\sim$10 nm in the UV range, thus the photons are absorbed very close to the detector surface. Then, it increases very quickly up to $\sim$10 μm in the visible and near IR parts of the spectrum. This strong dependence has a consequence on the QE(λ) because, outside the depleted region, which extends

from the junction to all the epitaxial layer depth, the photogenerated carriers have a recombination probability different from zero [72, 73]. The recombination probability of the superficial layer can be minimized with a suitable design of the junction while the QE(λ), at longer wavelengths, can be improved enlarging the active volume. Examples of photon absorption spectra in NUV, visible and NIR regions are given in Figure 1.19.

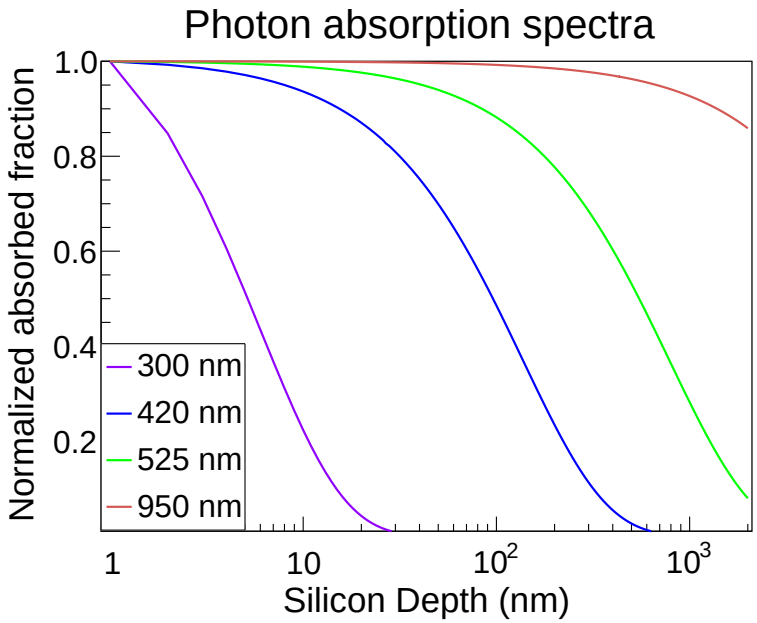

Figure 1.19: Examples of photon absorption spectra at different wavelengths in silicon are drawn in a semi–logarithmic plot.

The triggering probability studies in avalanche photodetectors began at the end of the fifties and continued during the years later [74, 75, 76, 77]. During the first years, the electrical current instabilities observed in devices biased above the breakdown voltage were related to two probabilities called turn–on and turn–off probability of current pulse. W. G. Oldham was the first to explicitly calculate the turn–on probability of an avalanche diode relating it to the ionisation coefficients of electrons and holes in silicon, $\alpha_{\mathrm{e}}(\mathrm{x})$ and $\alpha_{\mathrm{h}}(\mathrm{x})$, respectively. His work can be found in [78, 79]. In those works, the probability that an electron starting at the position x inside the junction triggers an avalanche in the device was called $\mathrm{P_e(x)}$ and the analogue probability for a hole was called $\mathrm{P_h(x)}$. The equations (1.15) were derived from these probabilities and the ionisation coefficients.

$$\frac{dP_e(x)}{dx} = (1 - P_e(x))\alpha_e(x)[P_e(x) + P_h(x) - P_e(x)P_h(x)] \tag{1.15a}$$

$$\frac{dP_h(x)}{dx} = (1 - P_h(x))\alpha_h(x)[P_e(x) + P_h(x) - P_e(x)P_h(x)] \tag{1.15b}$$

The terms in the square brackets in the previous equations derive from the law of the total probability because it is sufficient that at least one of the carriers triggers the avalanche to have an event. Thus, the total probability function $P_T(x)$ is expressed by the equation 1.16.

$$P_T(x) = P_e(x) + P_h(x) - P_e(x)P_h(x) \tag{1.16}$$

W.G. Oldham proposed a method, explained in [78], using the equations (1.15), to determine the breakdown voltage of a n–on–p device with depth equal to W, depending only on the carrier ionisation coefficients and two boundary conditions, $P_e(0) = P_h(W) = 0$, i.e. the electron probability to trigger an avalanche is zero at the surface and, similarly, the hole probability to trigger an avalanche starting at the deepest point is zero. The same equations can be also used to determine the triggering probability, $T_P(V,\lambda)$. As an example, in a n–on–p device with depth equal to 2000 nm, the function $P_T(x)$ has the shape represented in Figure 1.20 (black dashed line), at a fixed overvoltage. The electrons move from depth to the surface (from right to left in Figure 1.20) in a n–on–p device, forced by the electric field. The holes move on the opposite direction [80]. For this reason, the electron and hole triggering probabilities have their maximum values on the right and on the left, respectively. From the equations (1.15), it can be noted that the carrier triggering probability maximum values depend on the ionisation coefficients and, since $\alpha_e(x)$ and $\alpha_h(x)$ grow with the electric field and the first is always larger than the second [81, 82, 83], the maximum value of $P_e(x)$ is expected to be always larger than the corresponding $P_h(x)$ value.
Multiplying the photon absorption distribution (as that of Figure 1.18) for $P_T(x)$ at a particular overvoltage, and integrating over the total depth of the device, allows to obtain $T_P(V,\lambda)$. Since the exact shape of the triggering probability is not easily known, during the past years, a simplified formula was proposed [47, 84]:

$$T_P(V,\lambda) = 1 - e^{-\frac{V-V_{BD}}{V_\lambda}} \tag{1.17}$$

in which V_λ is the rate of growth of $T_P(V,\lambda)$ and it depends on the wavelength.

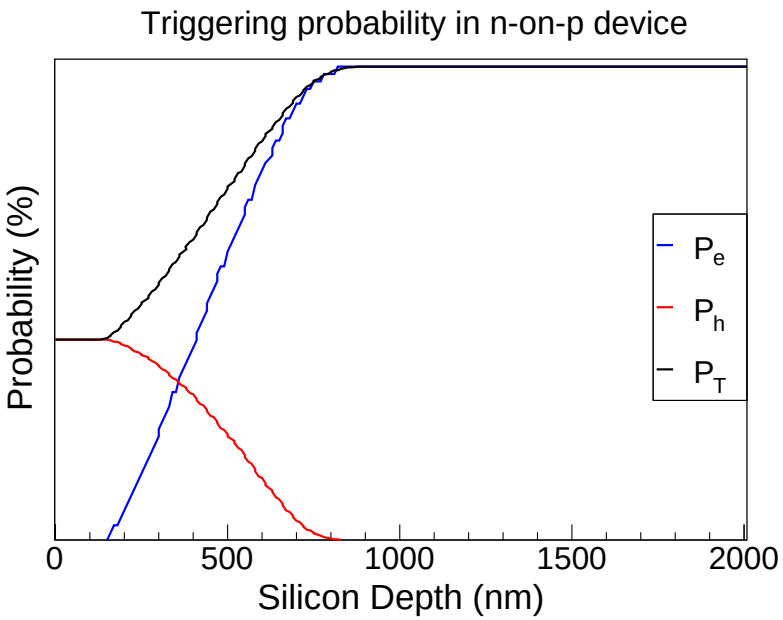

Figure 1.20: A plot representing the triggering probability of electrons (P_e, blue line), holes (P_h, red line) and total (P_T, black line) in a n–on–p SiPM, for a given overvoltage, is shown. P_e is maximum in the depth because the electric field causes the electrons to move from the depth to the surface. P_h is the opposite. The larger value of the P_e is related to the larger ionisation coefficient α_e.

Chapter 2

FBK Technology and Applications

2.1 SiPM development in FBK: First years

The development of Silicon Photomultipliers in FBK began in 2005, when a three–year collaboration between the Italian National Institute for Nuclear Physics (INFN) and the FBK, called DASIPM, aiming at the development and application of SiPMs, was launched. The FBK role was the technological development and the electrical characterisation of the detectors [85, 86].
The first SiPM prototypes produced in FBK were typical n–on–p devices built on p^+–substrate with a lowly doped p–type epitaxial layer having a thickness of about 4 μm. The detectors had a size of 1x1 mm^2 and 40 μm cell pitch. Each cell was quenched with a lowly–doped polysilicon resistor. The doping profile of the junction was fixed to have a very shallow junction ($\sim$100 nm from the surface) and a fully depleted device at the breakdown voltage. The ARC transmission was optimized to increase the transmittance around 420 nm (the wavelength was properly chosen to optimize the coupling to the Lutetium crystals family). A sketch of this prototype, taken from [85], is reported in Figure 2.1.
Since the first SiPM production, some of the actual typical characterisation procedures were used. In particular, the analysis of a single cell having the same layout and doping profile of the larger detector. This analysis is very useful, e.g. the IV of the SiPM was found in between the IV curve of the minimum and maximum current SPADs, multiplied by the number of SiPM cells. This observation suggested that the total current of a SiPM is given by the sum of the non–uniform single cell current contributions (Fig. 15 in [85]).
The most important results obtained with the electrical characterisation were the breakdown voltage uniformity (a mean value of 30 V was found with a maximum variation of $\sim$1 V among devices in the same wafer), the determination of the gain, equal to 10^6 at 3 V of overvoltage, and a DCR in the order of

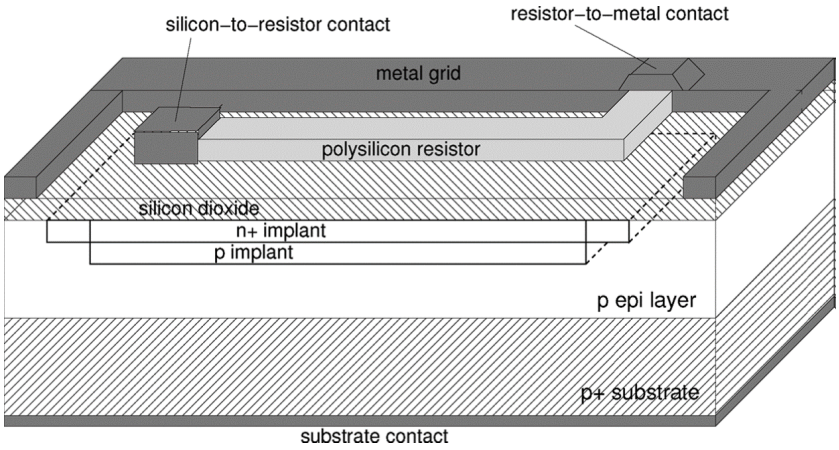

Figure 2.1: Cross–section of the first SiPM prototype produced in FBK. The picture is taken from [85].

2–3 MHz per square millimetre at 3 V of overvoltage. Both the gain and the DCR were found increasing linearly with the overvoltage, as expected. Also, a breakdown voltage temperature dependence of 80 mV/°C was estimated [86]. Even if these first SiPMs had a dead border region around the cell active area of 6 μm, the FF was very low because a large part of the active area was covered by the polysilicon resistor. Two different layouts were produced with a nominal FF of 20 % and 30 %. The small FF had a great influence on the PDE value. The PDE spectrum was quite flat between ∼450 nm and ∼650 nm with a maximum value of 14 %. In the NUV part of the spectrum, the PDE was about the half of the maximum due to the smaller triggering probability for short–wavelength photons (only the holes trigger events for these photons), as expected because the device was a n–on–p [86].
Table 2.1 summarises the first prototype features.

Table 2.1: 2005 FBK SiPM features at room temperature and 3 V of overvoltage.

Cell Pitch	40 μm
FF	20 %
V_{BD}	30-31 V
Gain	$\sim 10^6$
DCR	2–3 MHz
X–Talk	<5 %
PDE @550 nm	10 %
PDE @420 nm	6 %

The first SiPM production was also characterised at cryogenic temperatures. The estimation of the DCR and AP probability, as a function of temperature, are reported in Figures 2.2 and 2.3. The pictures are taken from [87].

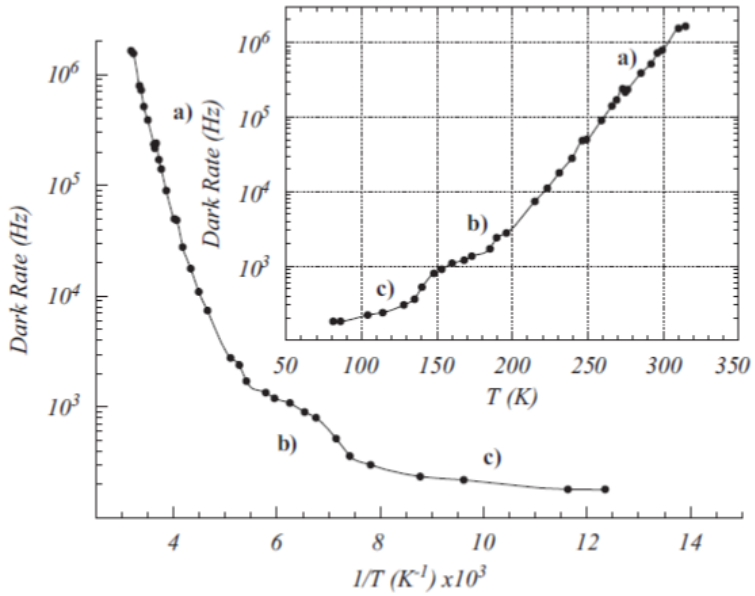

Figure 2.2: DCR as a function of temperature in the FBK SiPM is reported. The picture is taken from [87]. In the region (a), the thermal generation was the dominant contribution to the DCR, in (b), the band–to–band tunnelling was the dominant process. (c) was a region under study.

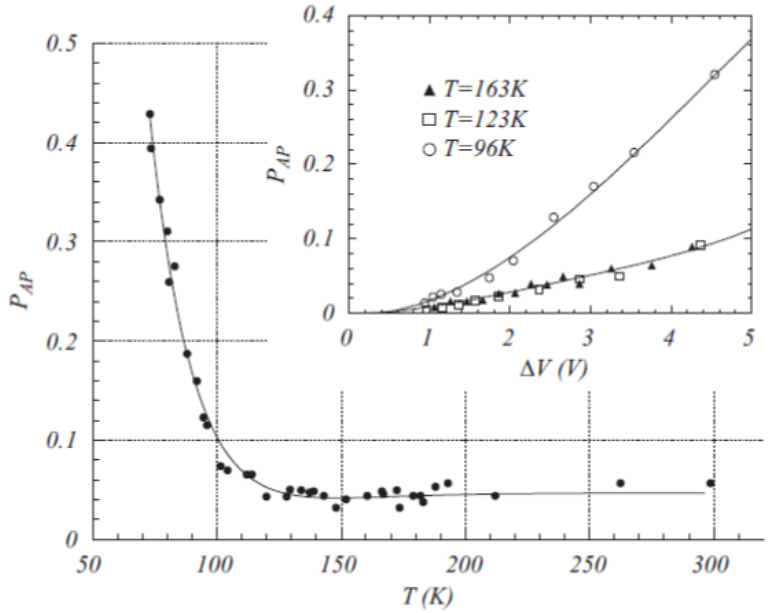

Figure 2.3: The afterpulsing probability as a function of temperature in the FBK SiPM is reported. The picture is taken from [87]. The constant value down to 110 K is shown. The increasing probability for lower temperatures is caused by the longer trap lifetimes.

The DCR dominating contributions are visble, thermal generation above 200 K and band–to–band tunnelling at cryogenic temperatures. The afterpulsing probability increases at temperatures below 110 K because the higher trap lifetimes.

The good results obtained with the first prototypes lead to the development of the technology with new productions starting in 2007. New projects lead to the development of devices designed to be used as read–out detectors in PET scanners. The improvements regard new layouts with increased FF and a new technology reducing the DCR. Larger devices were produced, up to 4x4 mm^2 with different cell pitches ranging from 40 μm to 100 μm. The new 40 μm cell pitch had a FF equal to 40 %, twice the value of the previous generation [88]. From the characterisation of the new generation SiPMs, new knowledge was gained. It was clear that the signal shape is deeply influenced by the device parasitic capacitances. In Figure 2.4, the signals of a 1x1 mm^2 and a 4x4 mm^2 with cell pitch equal to 50 μm are reported (the original plot can be found in [88]). The larger device, having a larger grid capacitance, C_g, in parallel with the read–out resistor of 50 Ω, forms a low–pass filter that clears the signal fast peak. Also, the DCR of the larger device scales exactly by a factor 16, as expected from the area ratio. The gain was equal, depending only on the quenching and diode capacitances, C_q and C_d.

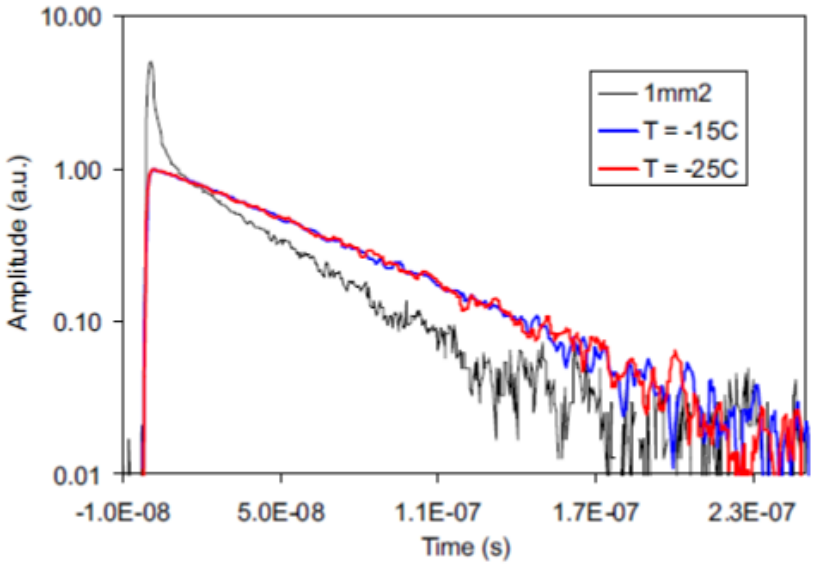

Figure 2.4: Three signals of 1x1 mm^2 (black line) and 4x4 mm^2 (coloured lines at different temperatures) SiPMs with cell pitch equal to 50 μm are shown (plot taken from [88]). In the larger device signals, the fast peak is not present due to the larger grid capacitance, C_g. It is in parallel with the 50 Ω of the read–out resistor forming a low–pass filter.

The new technology SiPMs showed a big DCR reduction. Figure 2.5 shows the DCR as a function of the overvoltage at different temperatures (the original

plot can be found in [88]). At room temperature, a DCR reduction by a factor three was measured.

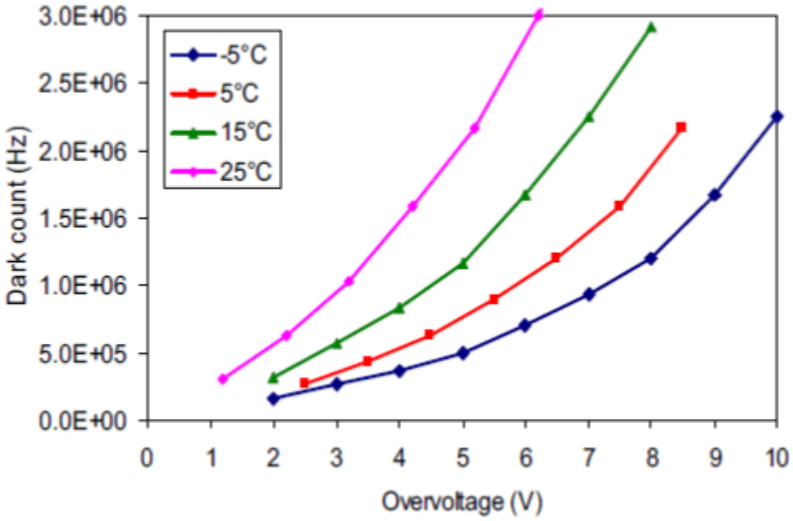

Figure 2.5: DCR as a function of overvoltage for different temperatures are shown (plot taken from [88]).

Having shown very good features in terms of primary noise and PDE, more and more the FBK SiPMs were coupled to Lutetium crystals family to measure the energy resolution and coincidence resolving time (CRT) performance for PET application (projects as HYPERImage, DASIPM2, Sublima). Many works in literature report such measurements using large area SiPMs or matrices [89, 90, 91, 92, 93]. Even if the measurement conditions were not the same (some author used matrices, others single devices; also, the devices had different size), the advancements in the detector performance are evident. In Table 2.2, the results of these measurements are reported.

Table 2.2: First FBK SiPM productions energy resolution at 511 KeV and coincidence resolving time (CRT)

Article	En. Res. FWHM (%)	CRT FWHM(ps)	Crystal size (mm^3)
G. Llosa' et al. [89]	20	~1400	1x1x10
G. Llosa' et al. [90]	14.5	Not measured	12x12x5
C. Piemonte et al. [91]	Not measured	200 (short), 230 (long)	3x3x5, 3x3x15
R. I. Wiener et al. [92]	12.5 (short)	230 (short), 260 (long)	4x4x5, 3.8x3.8x22
C. Piemonte et al. [93]	12	190	3x3x5

The improved results of the last works [91, 93] benefit of the Differential Leading Edge Discriminator (DLED) algorithm applied to the data [94]. In [95], the advantage of using the DLED algorithm was shown. In Figure 2.6, a plot showing the DLED advantage is reported (original plot in [95]).

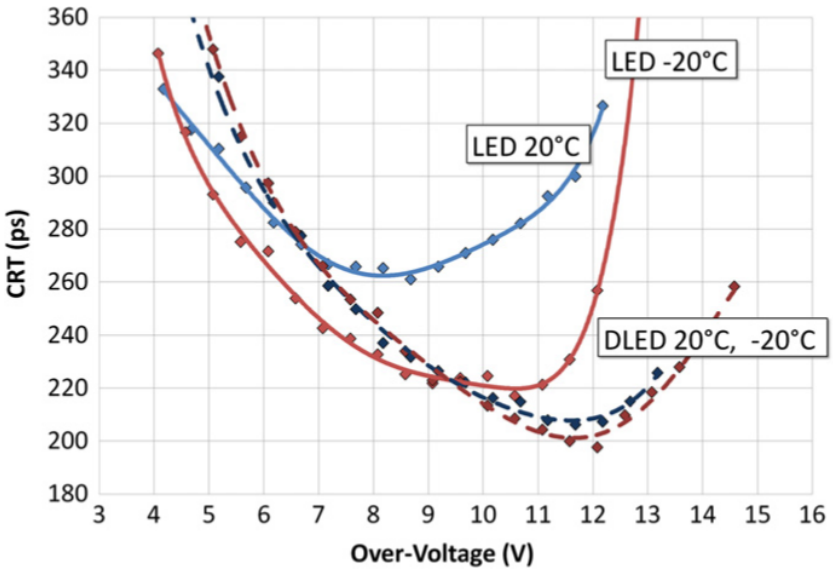

Figure 2.6: CRT of 4x4 mm^2 SiPMs coupled to 1.8x1.8x10 mm^3 LYSO crystals at different temperatures is reported. Plot taken from [95]. The employment of the DLED filter removes the temperature dependence and allows to reduce the CRT by, at least, 20 ps.

In the section 3.1, a complete description of the DLED algorithm will be given.

After many years of continuous improvements of the original technology, in 2013 two new technologies, based on n–on–p and p–on–n junctions, were presented. They were called RGB–SiPMs [96] and NUV–SiPMs [97, 98], respectively, due to the peak efficiency position. All the subsequent SiPM generations took these names.

The RGB–SiPMs are n–on–p devices as the original technology SiPMs, thus a comparison between them was possible. The newer device was modified, starting from the original one, to achieve a lower electric–field profile in the junction. This causes many benefits, as a DCR reduction, a higher V_{BD} uniformity, an increased PDE and a lower gain and V_{BD} temperature dependence. At room temperature and at 4 V of overvoltage, the newer device had a DCR less than 500 KHz/mm^2, a PDE ranging between 20 and 30 % in all the visible spectrum and an energy resolution of $\sim$10 % coupled to a LYSO crystal [96].

The new two technologies, having inverted p–n junctions, show the main differences in the PDE spectrum. In Figure 2.7, a plot comparing the PDE spectrum of the RGB and NUV technologies is reported (the original plot can be found in [98]). The peak PDE reaches similar values in the technologies but the peak wavelength is very different, from NUV to blue light for the NUV technology and from blue to yellow light for the RGB. The different shape of the spectrum is closely related to the junction, the photon absorption coefficient and the different electron and hole triggering probabilities. Due to the junction profile, in the RGB–SiPMs only the holes can trigger the events

of short–wavelength photons, mainly absorbed close to the surface, while the longer–wavelength photon events are triggered by both the carriers. In the NUV–SiPMs the carriers triggering the events are the opposite.

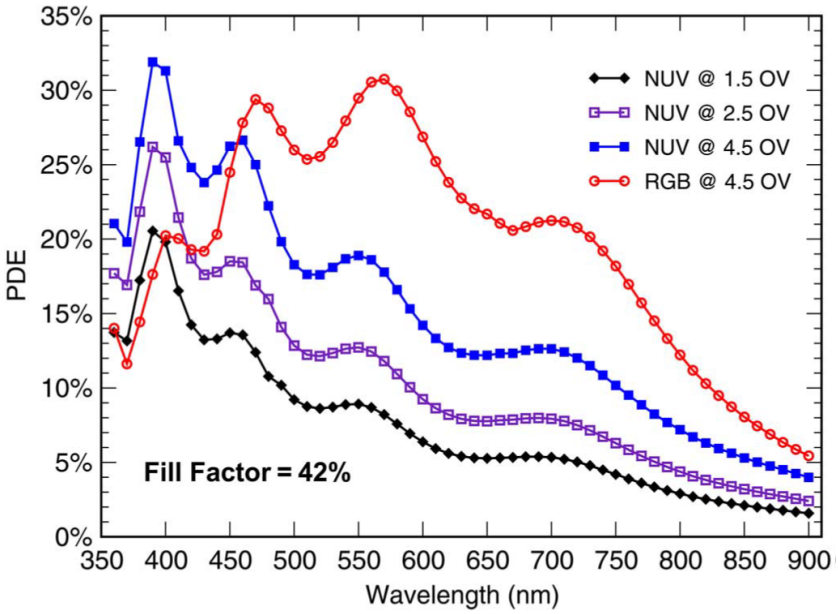

Figure 2.7: A comparison between the PDE spectrum in RGB and NUV technologies is shown. The plot is taken from [98]. Considering only the curves at the same overvoltage, the maximum PDE reached by the two technologies are comparable, exceeding the 30 %, but the peak wavelength is very different.

In this thesis, the focus is on the newer NUV–SiPMs produced in FBK. In the next section, a description of the NUV and NUV–HD (High–Density) technologies are given.

2.2 NUV and NUV–HD technologies

As anticipated in the previous section, the NUV–SiPMs are based on p–on–n junctions to enhance the PDE in the NUV–blue region of the spectrum. A cross–section of the device is shown in Figure 2.8 (original figure taken from [64]).
In a p–on–n device illuminated by short–wavelength photons, the carriers triggering an avalanche are the electrons, photogenerated very close to the surface. Due to the electric field direction, only the electrons can trigger the events of such photons. Since they have a larger ionisation coefficient than the holes, this leads the p–on–n device to have a higher triggering probability, and a faster increase of this probability with the overvoltage, with respect to an equal n–on–p. This implies that, in general, a p–on–n device reaches the same PDE for short–wavelength photons than a n–on–p one at a smaller overvoltage, having

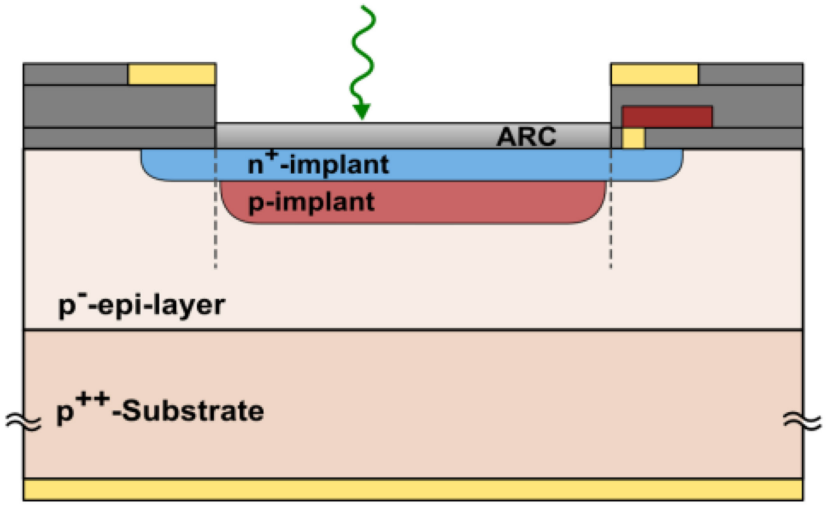

Figure 2.8: A simplified NUV–SiPM cross–section is shown. The plot is taken from [64].

a lower primary noise and gain, thus also a lower correlated noise.
The electro–optical characterisation of the first NUV–SiPM showed very interesting results. The device had the same layout of the subsequent versions, with a cell pitch of 50 μm and a FF equal to 42 %. The PDE of this technology was very good for the detection of short–wavelength photons. It was quite flat between 350 nm and 450 nm and reaches a maximum value ranging between 25 % and 30 %. The big problem of this first prototype was the high electric field causing a V_{BD} around 15 V and a very high noise, both primary and correlated [97]. Through an accurate electric field engineering, the second NUV–SiPM was a much better device than its predecessor. As shown in [98], this detector had a V_{BD} around 25.5 V with a uniformity at wafer level around 100 mV; a very low primary noise, lower than the previous version by an order of magnitude (a plot taken from [98] is reported in Figure 2.9); a direct cross–talk probability lower than 10 % but a very high delayed correlated noise probability, more than 50 % at 4 V of overvoltage. The PDE spectrum was similar to the first version but the values were higher, almost by a factor two at the same overvoltage. It is very interesting to note that the measured energy resolution and CRT of this detector, coupled to a LYSO crystal with dimension 3x3x5 mm^3, were at the same level of the best results obtained with the original technology SiPMs [93], 10 % FWHM and 210 ps FWHM [98].

The NUV–SiPM technology was upgraded two times in the last three years. In [69], the first layout and the technological improvement are described. The layout was modified reducing the cell pitch to 40 μm and reducing the dead border region around the active area, increasing the FF to 60 %. The new SiPM was built on a substrate with a lower carrier lifetime, more than an order of magnitude. This solution reduced the diffusion length of carriers photogen-

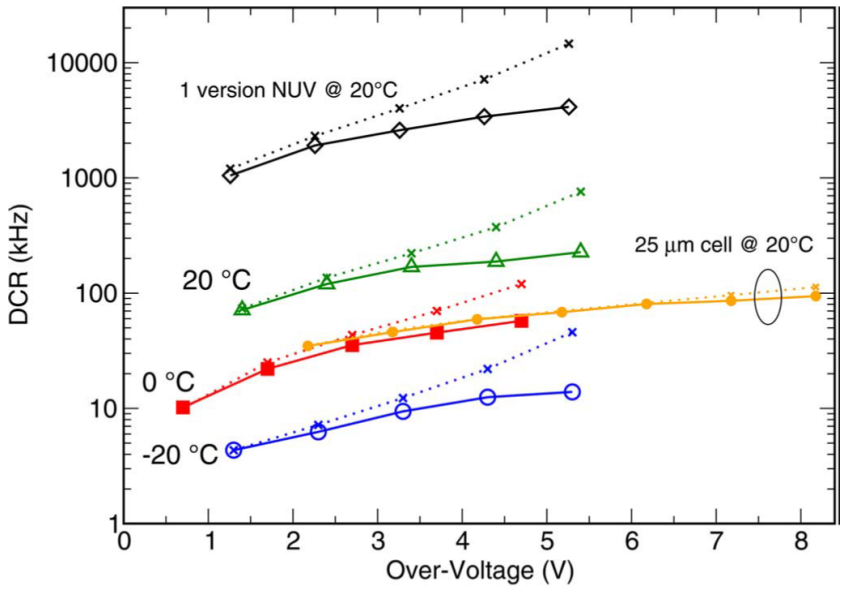

Figure 2.9: A comparison between the measured DCR of the first two NUV versions is shown. The plot is taken from [98]. The second NUV (continuous coloured lines) shows a DCR lower by an order of magnitude than the first version (black continuous line). Every measurement refers to a 1x1 mm^2 with 50 μm cell pitch but one, indicated in the plot as a yellow line, referring to a 1x1 mm^2 with 25 μm cell pitch.

erated in the substrate by secondary photons emitted during the avalanche discharge, thus, also, the delayed noise probability. From a IV measurement comparison, the lower correlated noise contribution can be qualitatively observed. In Figure 2.10, this comparison is shown (original plot taken from [69]). The curves of the two substrate SiPMs are very different after the breakdown voltage. The newer device had a smaller post–breakdown current without the abrupt diverging point visible in the old one at about 3.5 V, overvoltage at which the correlated noise probability diverged.
The correlated noise probabilities were also directly measured and compared. In Figure 2.11, this comparison is reported (original plot taken from [69]). The measured DiCT was larger in the new substrate version, unexpectedly, but the delayed noise components were very low, at the limit of the sensitivity measurement.
The different behaviour of the noise components did not allow to conclude what was the better device between the two substrate types. A comparison between the ECF could solve this doubt. Such a comparison is shown in Figure 2.12 (plot taken from [69]), along with a gain comparison. The new substrate has always a lower ECF, thus a lower amount of charge added to the cell signal due to the presence of the correlated noise, in particular of the delayed noise. For this reason, the new type SiPMs were called NUV–Low–AP SiPMs.
The PDE comparison showed a perfect match between the two types at the

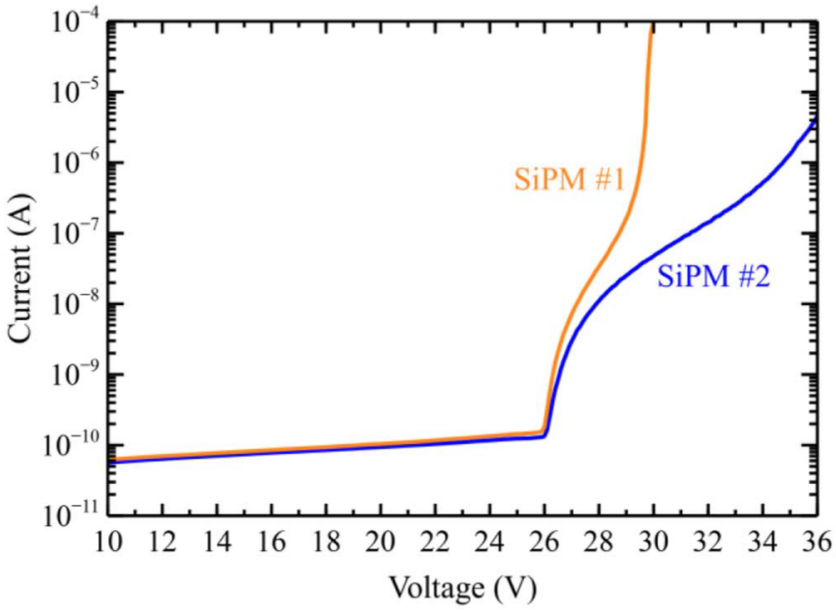

Figure 2.10: A comparison between the measured IV plots of the NUV–SiPMs with different substrates is shown. The plot is taken from [69]. The SiPM #1 is the old substrate version and has a clear diverging point at ∼3.5 V due to the very high correlated noise probability.

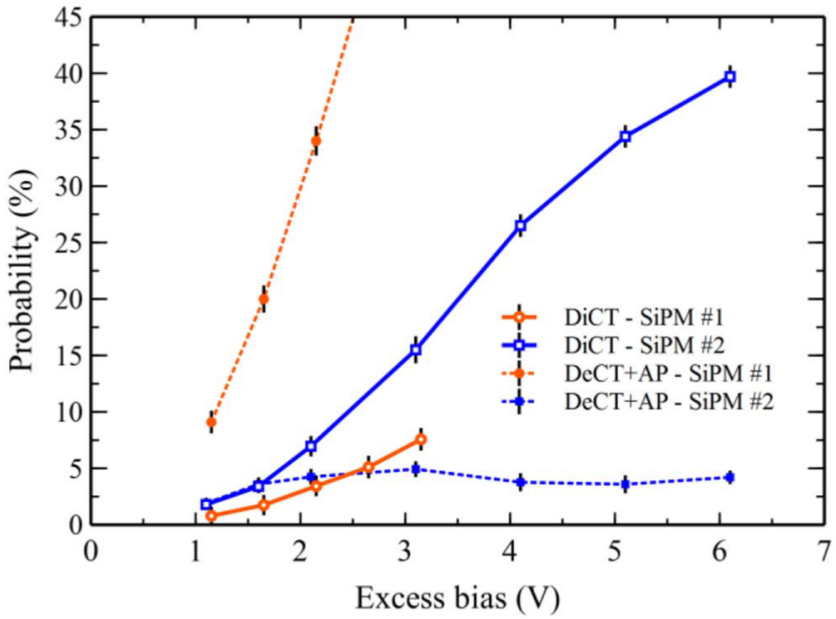

Figure 2.11: A comparison between the measured correlated noise probabilities of the NUV–SiPMs with different substrates is shown. The plot is taken from [69]. The old substrate SiPM has a lower DiCT probability but a much higher delayed noise one at the same excess bias (overvoltage).

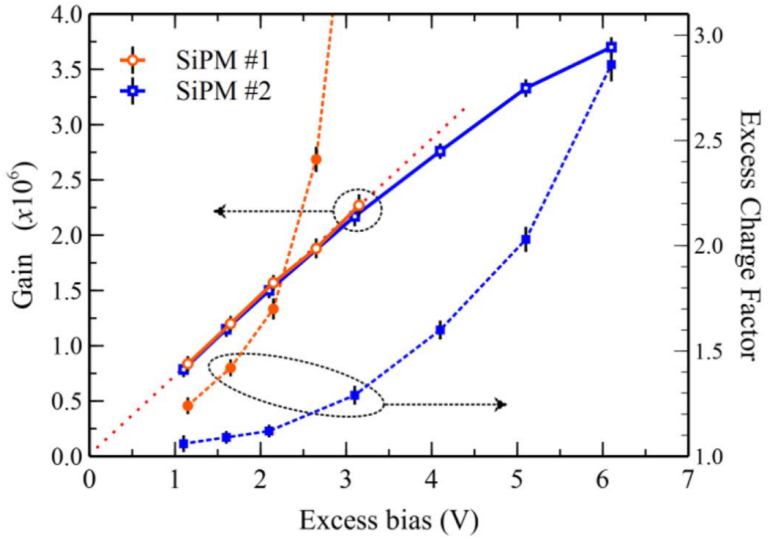

Figure 2.12: A comparison between the measured Gain and ECF of the NUV–SiPMs with different substrates is shown. The plot is taken from [69]. The gain is equal in the devices, showing its independence from the substrate properties. The old substrate SiPM has a larger ECF at every excess bias.

same overvoltage from NUV wavelengths up to ∼450 nm. Above this value, the old substrate SiPM had a higher PDE because it had a larger QE(λ) of the photogenerated carriers in the substrate by the long–wavelength photons. The comparison is shown in Figure 2.13 (plot taken from [69]).

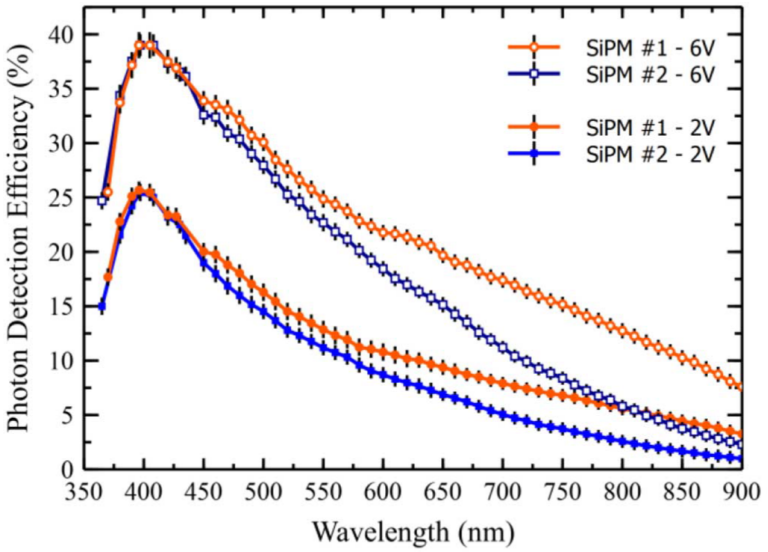

Figure 2.13: A comparison between the measured PDE of the NUV–SiPMs with different substrates is shown. The plot is taken from [69]. The old substrate SiPM reaches larger PDE values above 450 nm because the lower carrier lifetime in the substrate increases the QE(λ) at long–wavelengths.

The NUV–Low–AP demonstrated to be a better device than its predecessor having a similar PDE, in particular in the NUV–blue region, and a lower correlated noise. In addition, the similar PDE was measured on SPADs because the maximum operating overvoltage of the SiPM with the old substrate was lower than 6 V. Comparing the values at realistic biasing conditions, the new SiPMs had a PDE about 50 % higher than its predecessor.

The last upgrade was briefly described in [99]. This last SiPM was produced on the same substrate with smaller carrier lifetime, thus it is a second version of the NUV–Low–AP. In addition, it had a lower electric field to reduce the DCR, not correlated with thermal generation. For this reason, it was called NUV–Low–Field. This production showed a very similar PDE at the same overvoltage and correlated noise probabilities of the NUV–Low–AP but a slightly lower DCR and gain (due to the lower cell capacitance, C_D). The plot representing the DCR comparison is shown in Figure 2.14.

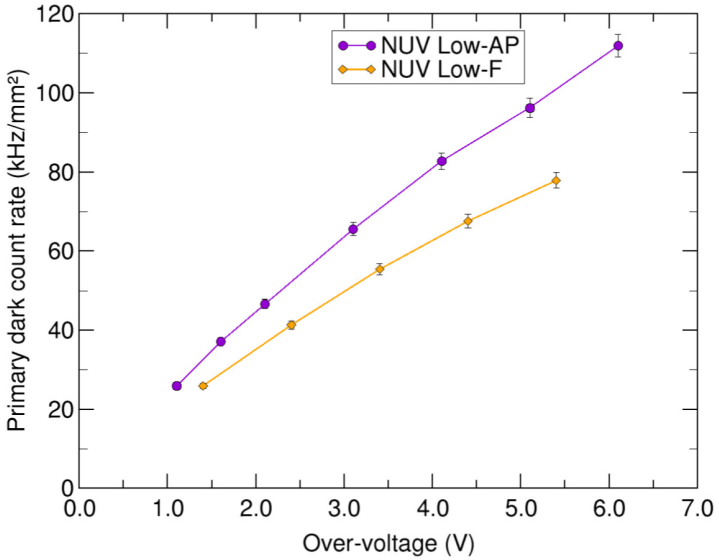

Figure 2.14: A comparison between the measured DCR of the NUV–Low–AP and NUV–Low–Field is reported. The plot is taken from [99]. The Low–Field version has a slightly lower DCR due to the lower electric field.

The NUV–Low–Field did not show a significant technological improvement.

A much better device was obtained applying to the NUV–Low–AP technology the High–Density (HD) concept, successfully introduced some year earlier for the RGB technology [100]. In [101, 102], the description and first characterisation of the new NUV–HD technology is given. In Figure 2.15, a comparison between the standard NUV layout and the HD version one is reported (original figure taken from [101]). From the comparison it is possible to observe the main difference between the two technologies, i.e. the presence of the deep trenches in the HD version. The trenches around the cell reduce the secondary photon transmission probability. In addition, the cells are smaller and they have an

increased FF, because the border region size was reduced to $\sim$2 μm. From these modifications, an increased PDE, a lower correlated noise probability and a similar primary noise were expected.

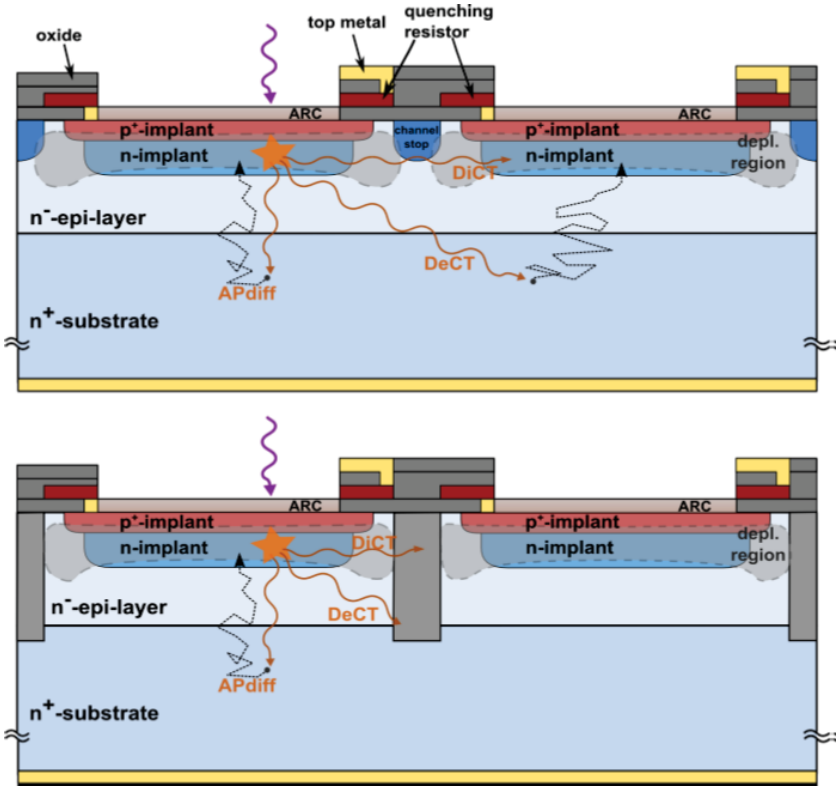

Figure 2.15: A comparison between the layout of the NUV and the NUV–HD technologies is reported. The plot is taken from [101]. In the HD version, the deep trenches allow to reduce the transmission of the secondary photons and the smaller cells reduce the gain. Thus, the correlated noise probability is expected to be lower.

The characterisation of the NUV–HD technology will be shown in the fourth chapter. In the following section, a list of possible applications in which a NUV or NUV–HD device could be useful is given.

2.3 Possible applications

Due to its features, such as the high PDE in the NUV to blue region, the low DCR and correlated noise probability at typical operating conditions and the very good timing performance, the NUV technology is well suited for a large number of applications [103]. In this paragraph, a review of some of them is given. A particular focus will be given to one application, the Cherenkov light detection for astroparticle physics, in the next subsection.

In some application, the photosensor can be coupled to a crystal scintillator and used to read out the light (e.g. High Energy Physics (HEP) experiments

and medical applications). In HEP experiments, the SiPMs can be used to detect the electromagnetic (EMCAL) and hadron (HCAL) calorimeters light. Usually, the calorimeters consist of towers of alternate absorber and scintillator layers. When a ionising particle (also photons in EMCAL and neutrons in HCAL) pass through the calorimeter, it loses its energy via ionisation and excitation processes. Both these processes convert the particle energy in light. The light emission spectrum of the calorimeter depends on the scintillator material. Nowadays, almost all the HEP experiments calorimeters employ PMTs and other type of silicon photosensors, but the possibility to replace the actual detectors with SiPMs was largely investigated in the past years by many collaborations [104, 105]. The advantages of the SiPMs could be the simpler read out electronics due to the high internal gain, the use in environments with strong magnetic fields due to the insensitivity of the silicon, the desired high granularity and the simplicity to build compact modules with low power and material budget. Also, the low radiation damage could be an important point. In [103, 106, 107], the authors presented the status of two prototype detector modules consisting of small extruded plastic scintillators (3x3x0.5 cm^3 and 3x3x0.3 cm^3) coupled to Hamamatsu MPPCs in a side for the CALICE experiment. The plastic scintillators were Saint–Gobain BC–420 and had an emission spectrum peaked in the NUV region, as shown in Figure 2.16 (taken from the Premium Plastic Scintillators Saint–Gobain datasheet [108]). This prototype was the first one in which the MPPCs were directly coupled to the scintillator, without the use of a wavelength shifting fibre (WLS). This was possible because the employed Hamamatsu MPPCs had a high PDE in the NUV region, well matching the emission spectrum of the scintillator.
The medical inspections, in particular the positron emission tomography (PET), were a field in which the use of SiPMs was largely investigated in the last ten years too. During a PET exam, a serum, in which a short lifetime β^+ emitter is, usually, bound to a sugar molecule and injected into the patient. Inside the body, the compound is mainly absorbed by the cancer cells and the β^+ annihilate with the electrons emitting two gammas in coincidence at $\sim$180° to each other. Measuring the arrival position of the gammas in a corona around the patient, it is possible to track a direction connecting the two measured points intersecting the patient. After many reconstructed couple of events, all the directions indicate the presence of a cancer in a limited region in the patient. This region size could be reduced measuring also the gamma rays arrival time. This technique is called time of flight PET (TOF–PET) [67, 103, 109, 110, 111]. By the arrival time difference, the presumed emitting point can be reconstructed along the measurement direction. The time measurement precision is directly related to the emission point reconstruction accuracy. Fast scintillators and detectors, as the SiPMs, must be used. The most used crystal scintillators are the Lutetium compunds as L(Y)SO and LSO, doped with Cerium and Calcium, having a very high light yield and a fast decay time, about 40 ns. The

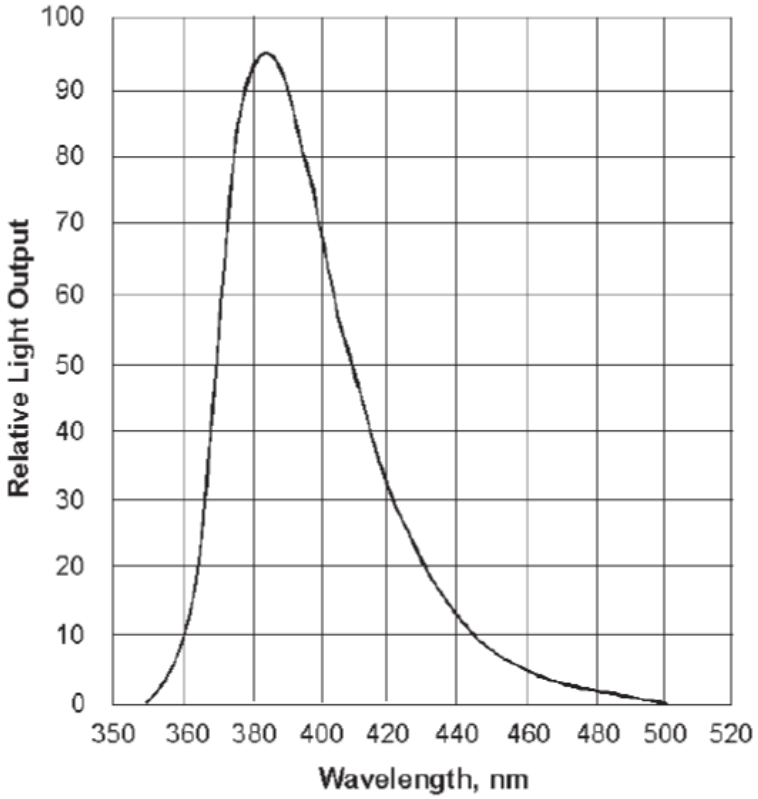

Figure 2.16: Emission spectrum of a BC–420 plastic scintillator produced by Saint–Gobain. Plot taken from [108]. The emission light is centred in the NUV region.

emission spectrum of a LYSO crystal is peaked in the blue region, as reported in Figure 2.17, taken from [112]. The use of the SiPMs could allow to obtain excellent results in terms of coincidence resolving time (CRT), thus the reconstruction point inside the patient could be more accurate. In addition, the possibility to realise a PET/MRI technique, due to the insensitivity to the magnetic fields, obtaining a more complete information is a strong point for the development of the detectors.

In some physics experiment, searching for very rare events, the SiPMs can detect the scintillation light produced by a gas or a liquid. This is the case of the Darkside [113] and NEXT [114] experiments. The DarkSide experiment has the aim to directly detect the Dark Matter. From cosmological and gravitational observations, it seems that the ordinary matter of the Standard Model of Particle Physics (baryons, leptons and bosons) is only a small fraction of the total matter in the universe, less than 20 %. The remaining part of the matter is unknown, for this reason it is called Dark Matter. Up to now, nobody found direct evidence of the Dark Matter existence but the most accredited theories put some constraints on the mass (at least more than

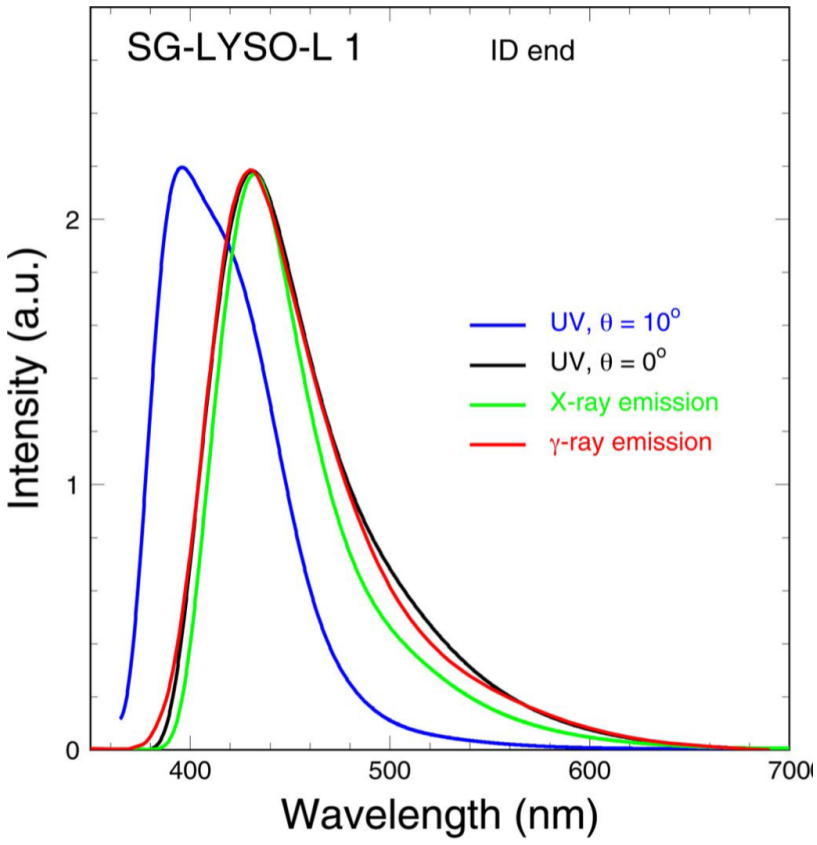

Figure 2.17: Emission spectrum of a LYSO crystal excited by different ionising particles. Plot taken from [112]. If excited by a gamma ray, a LYSO crystal has an emission spectrum centred in the blue region.

10 GeV/c^2), the electrical charge (neutral) and the possible interactions with other elementary particles (gravitational and some weak interaction form) of the Dark Matter. All of these constraints lead to the name WIMPS (Weakly Interacting Massive Particles) for the Dark Matter components. In DarkSide, a time projection chamber (TPC) filled with dual phase liquid Argon, extracted from underground sources to be radiopure, without the ^{39}Ar contamination, is used to detect the Dark Matter. The detection of the Dark Matter could happen measuring the nuclear recoil of the Argon nuclei after a scattering with the WIMPS. During the motion, a recoiling nucleus loses its energy in the medium via scintillation and ionisation processes. The first lead to the prompt emission of extreme UV photons at 128 nm. The ionisation electrons drift inside the TPC and, leaving the liquid phase and entering the gaseous one, excite the medium producing secondary photons at the same wavelength [115]. The TPC must operate at cryogenic temperature to maintain the Argon in a liquid state. At this temperature, the features of the SiPMs must be assured. In [116], a complete characterisation of two NUV–HD versions at cryogenic temperatures was presented.

NEXT is a physics experiment searching for the neutrinoless double beta decay, $\beta\beta0\nu$. This particular decay would demonstrate that the neutrino is a Majorana particle, the only one in the Standard Model, i.e. the neutrino is its own antiparticle. In addition, the decay demonstrates that the total leptonic number is not a perfectly conserved quantum number, and this could be linked to the matter–antimatter asimmetry observed in the universe via a process known as leptogenesis. In NEXT, a high–pressure electroluminescence TPC filled with high purity Xenon gas (HPXe) enriched with ^{136}Xe is used to detect this very rare event. In a double beta decay event, the two beta particles lose their energy in Xenon via ionisation and excitation. The second process lead to the prompt emission of vacuum UV photons (VUV) at 178 nm. The ionisation electrons drift inside the TPC to the anode entering in a region with a stronger electric field emitting other VUV photons via secondary excitation [103, 117, 118]. Since the typical SiPM PDE in this extreme UV region is very low, a protocol [119] was developed for coating the detectors with tetraphenyl butadiene (TPB) shifting the VUV light to the NUV–blue region. In Figure 2.18, the measured TPB emission spectra, obtained from a glass plate coated with 0.1 mg/cm^2 illuminated with 246 nm and 340 nm photons, are shown (plot taken from [119]).

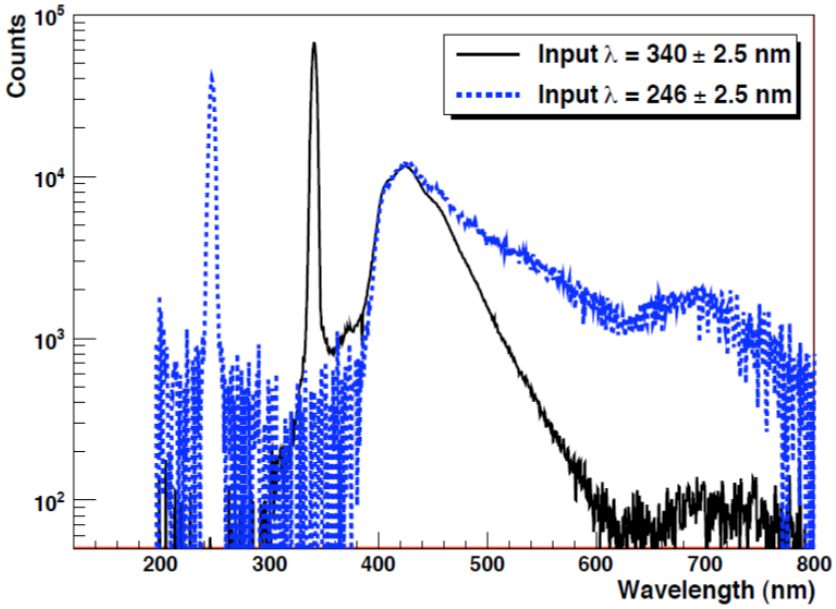

Figure 2.18: TPB emission spectra measured illuminating a glass plate with 246 nm and 340 nm photons. The light is shifted to longer wavelengths, mainly around two peaks located at ∼425 nm (fluorescence) and near 700 nm (phosphorescence). Plot taken from [119].

It is possible to observe the light shifting to longer wavelengths with two clearly visible peaks, the first at ∼425 nm (fluorescence light) and the second near 700 nm (phosphorescence light). The much larger PDE of the p–on–n devices

in the blue region, makes the first peak dominating the light yield, thus almost only the prompt fluorescence emission is detected by the sensors.

In this section, the possibility to use the SiPMs to detect the scintillation light was shown. The NUV technology is also well suited to detect UV light without the use of the scintillators. This is the case of the Cherenkov light detection. In the following subsection, one experiment based on the Cherenkov light detection, the Cherenkov Telescope Array (CTA) [120], will be presented in detail.

2.3.1 The Cherenkov Telescope Array experiment

The Cherenkov Telescope Array (CTA) will be a future ground–based Imaging Atmospheric Cherenkov Telescope (IACT). Its aim will be the detection of cosmic gamma rays with energy in between 20 GeV and 300 TeV. These gamma rays will be used as messengers to study their cosmic sources (e.g. active galactic nuclei (AGN), starburst galaxies, pulsar wind nebulae, shell–type supernova remnants, giant molecular clouds, X–ray binaries) [121].

A very high energy cosmic ray, entering the Earth atmosphere, produces a cascade of secondary particles, called Extensive Air Shower (EAS). The EAS number and type of particles and its footprint at ground are related to the cosmic ray originating it. A hadron induced EAS consists, mainly, of mesons (pions and kaons, above all) and nucleons and has a very large size at ground. The EAS generated by a lepton or a gamma ray consists of photons and electrons and it is very narrow at ground, compared to a hadron induced one. Two typical EASs are represented in Figure 2.19. It is possible to compare the EAS generated by the two different particles. The hadron induced EAS begins at a lower altitude and it develops more in width.
The detection of every particle of the cascade, to reconstruct the original one, is impossible because a huge detector would be needed. Actually, at ground level, the development of an EAS can have a very large area, in the order of 10^5 m^2 or even more. In the past years, to overcome this problem, the collaborations studying the cosmic rays developed a new type of cosmic ray observatory based on the use of an array of detectors covering a large area. Such an array is not able to detect every particle of an EAS but, using sophisticated models, it is possible to reconstruct the shower, and the particle originating it, from this sampling. An example of such detectors, now operating to study the cosmic radiation, is the Pierre Auger Observatory [122].

A ground–based IACT is a type of cosmic ray observatory specifically designed to detect cosmic gamma rays. As above written, a gamma ray induced cascade is mainly composed by photons and electrons. Due to their low mass, the charged particles of the shower travel through the air at a speed larger than the phase velocity of light in medium, thus they emit secondary photons via the Cherenkov effect [123]. The Cherenkov photons are emitted in the forward

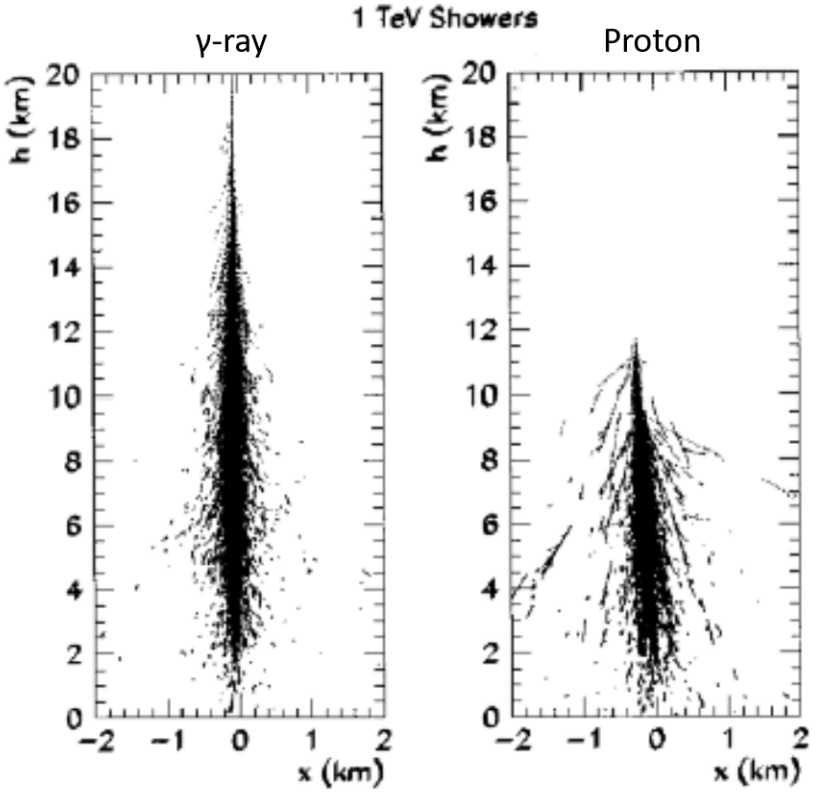

Figure 2.19: Typical Extensive Air Showers (EASs) generated by a gamma ray (left) or a cosmic proton (right). On the Y axis, the altitude is reported, on the X axis, the distance in Km from the vertical direction of the primary cosmic ray at which the cascade particles arrive.

direction and are distributed over the surface of a cone around the particle direction with vertical angle equal to 2θ. The emission angle θ is governed by the law (2.1).

$$cos\theta = \frac{1}{n\beta} \tag{2.1}$$

The Cherenkov photons are not monochromatic, they follow the distribution:

$$dF = \frac{q^2}{c^2}(1 - \frac{1}{n^2\beta^2})\omega d\omega, \tag{2.2}$$

Integrating the equation (2.2) over the frequencies ω for which the traversed medium is transparent, the intensity of the Cherenkov radiation, emitted by every particle having speed equal to β and electrical charge equal to q, can be determined. The Earth atmosphere is not transparent for photons having wavelength smaller than about 300 nm. The Cherenkov photon distribution

generated in a EAS is described by a decreasing function with a maximum at ∼300 nm. Such a spectrum is shown in Figure 2.20.

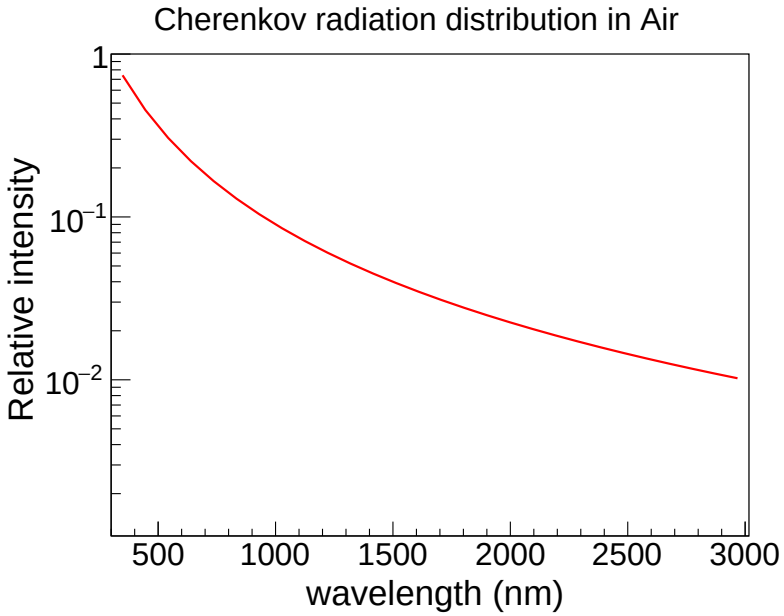

Figure 2.20: The simulated Cherenkov photon distribution in Earth atmosphere is shown. The emission is maximum at about 300 nm because the Earth atmosphere is not transparent for smaller wavelengths.

The emitted photons have wavelength ranging from NUV to MidIR. Dividing the spectrum in the regions NUV, Visible and IR, it is possible to estimate a relative emission in the three regions equal to 25 %, 32 % and 43 %, respectively. Even if the larger fraction of the Cherenkov radiation is emitted in the IR region, the camera detectors have, usually, a poor efficiency in this region (e.g. silicon detectors can not detect photons with wavelength larger than ∼1100 nm, thus only one third of the total Cherenkov radiation can be, theoretically, detected). In addition, the Cherenkov photons must be distinguished from the night sky background radiation that is quite constant between ∼350 nm up to the visible light and increases in the IR. For these reasons, the camera detectors must have a high efficiency in the NUV region and a bad detection in the visible and IR regions to increase the signal–to–noise ratio.
The array detects only parts of the footprint of the Cherenkov cones. For this reason, reconstruction models must be used to rebuild the Cherenkov cones of every particle of the shower, obtaining the energy and momentum of the charged particles in the EAS. From these informations, the primary gamma ray energy and direction can be determined and the source pointed, also by telescopes operating at other wavelengths.

The actual operating IACTs have a small number of telescopes (five in H.E.S.S. [124], four in VERITAS [125] and two in MAGIC [126]). These small

numbers do not allow a complete sky survey in a reasonable amount of time (e.g. H.E.S.S. completed a survey of the Milky Way covering about 600 square degrees but, with the same sensitivity, the full sky coverage would be reached after a decade of observations) and limit the sensitivity region from several tens of GeV up to some tens of TeV. The CTA Collaboration decided to build two sites with a very large number of telescopes in each site to overcome these problems increasing the sensitivity and the sky coverage with respect to the actual observatories of at least one order of magnitude. For the northern array site, the island of La Palma in the Canary Islands was chosen, and for the southern array site, Paranal in Chile. In each site, different size telescopes will be employed because the gamma ray energy range to explore is too large for only one type detector. In detail, the northern site project will consist of 4 Large Size Telescopes (LSTs) and 15 Medium Size Telescopes (MSTs) to explore the energy range from 20 GeV to 20 TeV. In Figure 2.21, the planned array design is shown.

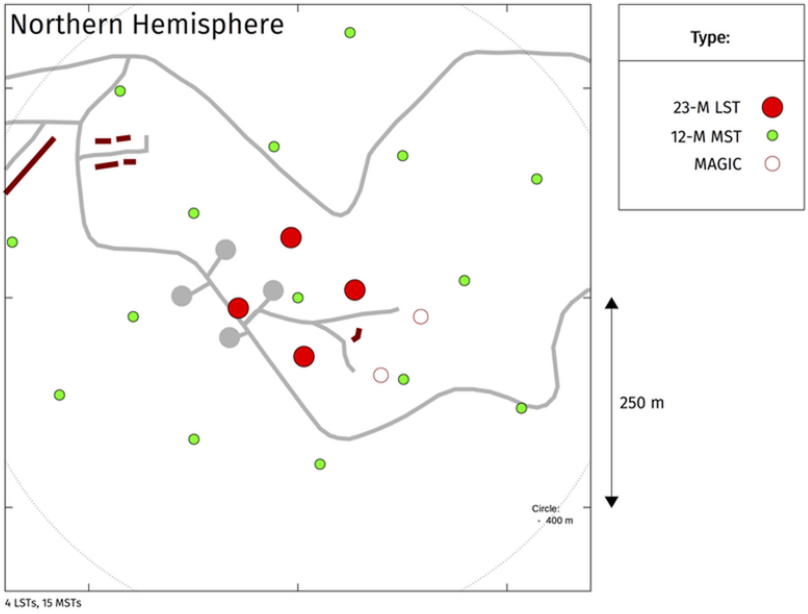

Figure 2.21: The planned CTA array design in the northern site is shown. Picture is taken from the website [120]. In the legend, the telescope types are indicated.

The southern site project will consist of a larger number of telescopes to cover the whole energy range, from 20 GeV to 300 TeV: 4 LSTs, 15 MST and 70 Small Size Telescopes (SSTs). In Figure 2.22, the planned array design is shown. Both the pictures are taken from the official website [120].
The different size telescopes will allow to cover the total energy range. Each type will be used to cover only a part of the energy range to investigate with small overlaps between adjacent regions. In detail, the total energy spectrum to investigate can be divided in the following three subregions:

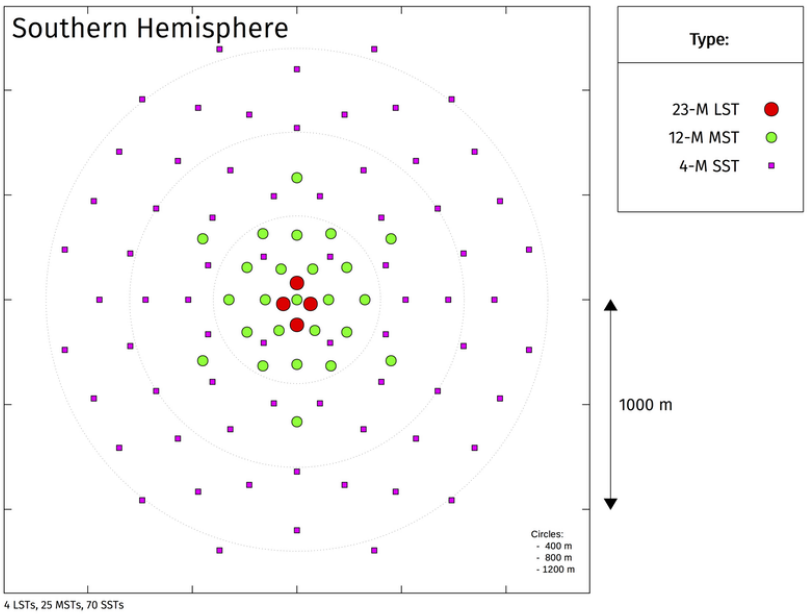

Figure 2.22: The planned CTA array design in the southern site is shown. Picture is taken from the website [120]. In the legend, the telescope types are indicated.

- the low–energy range, up to 100 GeV: the main detector used in this energy range will be the LST. They will have a mirror of 23 m diameter and, in the array, there will be four of them, placed very close to each other covering a total area of more than 10^3 m^2, at least the 10 % of the expected footprint of the Cherenkov cones at ground.

- the core–energy range, from 100 GeV to 10 TeV: the main detector used in this energy range will be the MST. They will have a mirror of 12 m diameter and, in the array, they will be placed at about 100 m to each other covering a total area larger than the expected footprint of the Cherenkov cones at ground. The MST will be similar to the actual observatories detectors, thus the acquired knowledge from the other experiments could be used. In addition, having an array size larger than the Cherenkov cone, in almost every event it will be possible to have detectors close to the optimum distance from the shower axis (about 70–150 m), where the light intensity is large and the intensity fluctuations are small.

- the high–energy range, over 10 TeV: the SST will be the main detector used in this energy range. Since in this region a small number of events per year is expected, the use of many telescopes, having a few m^2 diameter, with spacing of 100–200 m covering a very large area, up to $5{\cdot}10^6$ m^2, seems a good choice to increase the collected events. Even if the SST have small mirrors, they can be used because the high light yield of the Cherenkov cones in this region.

In Figure 2.23, the sensitivity as a function of the cosmic gamma ray energy is shown (original figure can be found in [127]). The subregions in which the LSTs the MSTs and the SSTs will be the most used detectors are highlighted.

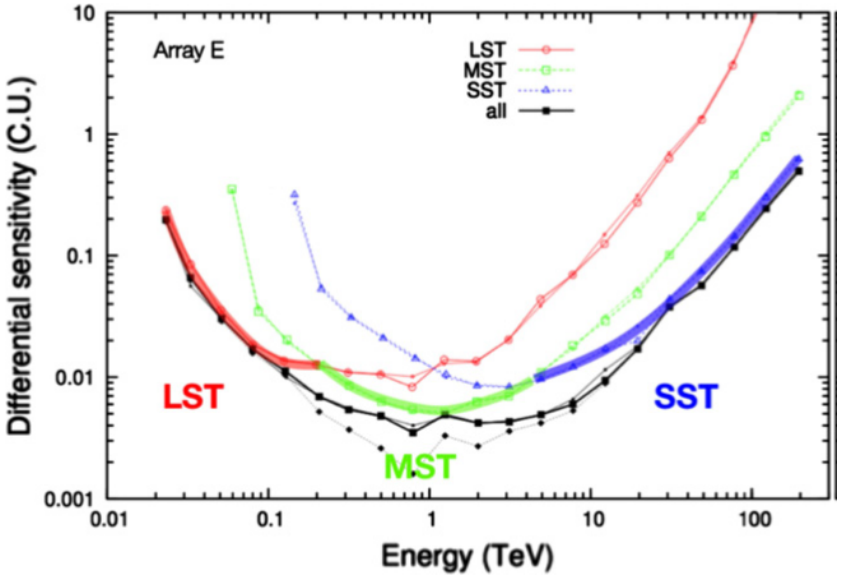

Figure 2.23: The sensitivity of the CTA array as a function of the gamma ray energy is shown (original figure can be found in [127]). Picture is taken from [127]. Every size telescope reaches a better sensitivity than the others in a different energy range.

The LSTs will be parabolic single–mirror telescopes, the MSTs will have a Davies–Cotton design and the SSTs will be Schwarzschild–Couder dual–mirror type. In Figures 2.24, 2.25 and 2.26, the designs are drawn (pictures taken from [127]).
The use of a dual–mirror concept in the SSTs allows to reach a larger Field of View (FoV), about 10°, compared to those of the LSTs, ∼4.5°, and MSTs, ∼7–8°, at the cost of a major complexity and the important shadowing of the secondary mirror over the first.
Regarding the photosensors of the camera, in the actual IACTs, the most commonly used detectors are the PMTs with bialkali photocathodes and electron multipliers based on a chain of dynodes. They are sensitive in the wavelength range of 300–600 nm (200–600 nm if a PMT with a quartz window is used). The bialkali PMT sensitivity curve well matches the spectrum of Cherenkov light arriving at ground level from EASs. These PMTs have a relatively high quantum efficiency, (an average of about 30 % in the wavelength range of interest), high gains, up to 10^6, and low noise, thus allow the reliable measurement even of single photoelectrons. A dynamic range of about 5,000 photoelectrons is obtainable with PMTs. For all of these reasons, these PMTs are the baseline

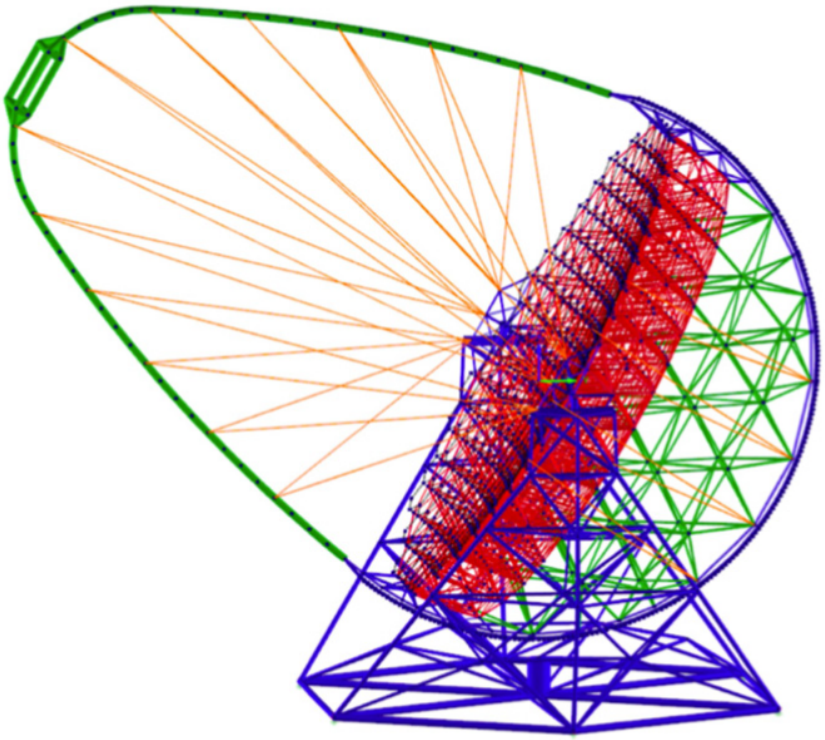

Figure 2.24: The parabolic single–mirror type telescope is shown (original figure can be found in [127])

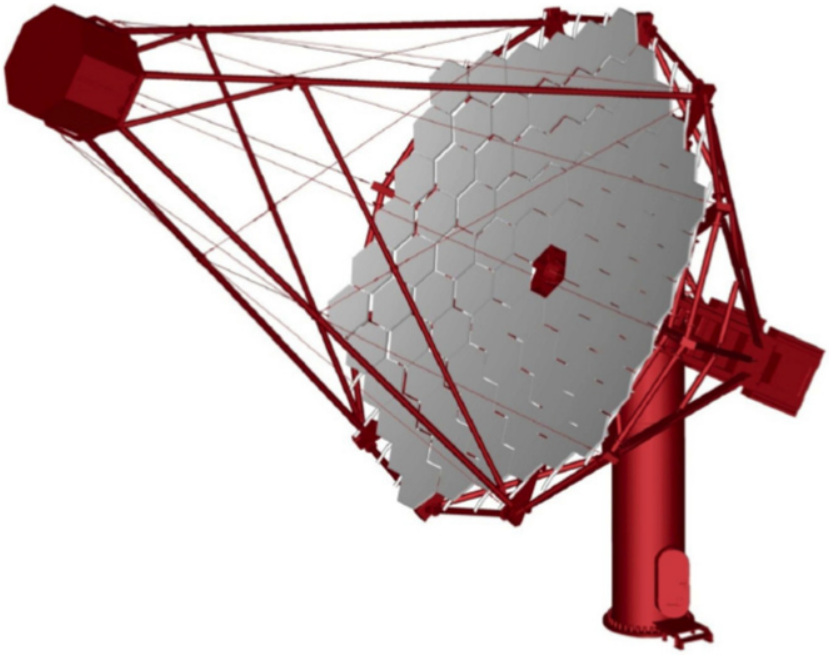

Figure 2.25: The Davies–Cotton type telescope is shown (original figure can be found in [127])

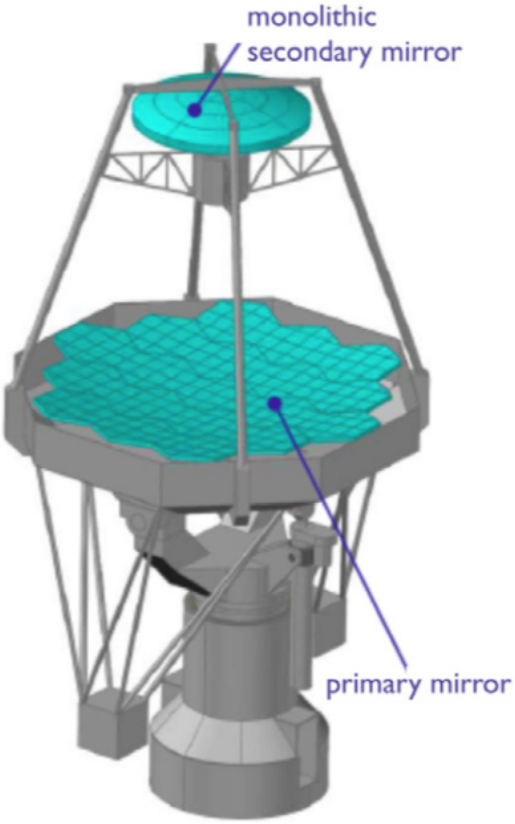

Figure 2.26: The Schwarzschild–Couder dual–mirror telescope is shown (original figure can be found in [127]).

choice also in CTA for the cameras of the different size telescopes. However, in the dual–mirror SSTs, the PMTs could be difficult to employ due to their size. Thus, the possibility to use other detectors, more compact as the SiPMs, is under investigation. To be considered as a valid alternative to the PMTs, the SiPMs must satisfy many requirements (some of them are reported in the list below).

- Match the spectral sensitivity. Due to the night sky background, the Cherenkov photons with wavelength longer than 600 nm have a decreasing signal–to–noise ratio. The desired sensor PDE must be very high in the range 350–550 nm and very low elsewhere.

- Have an adequate sensor area. The desired angular resolution is 0.2°, that, in a dual–mirror SST telescope, imply a maximum sensor size of about 6 mm.

- Have a large dynamic range. It is desired to have a dynamic range from the single photon level up to 5000 photons with a maximum deviation from a perfect linear response of a few percent.

- Have a very fast response. The Cherenkov photons time distribution on the camera strongly depends on the energy of the primary gamma ray but, in general, if the sensor response is under one nanosecond, the light structure of the Cherenkov light pulse can be correctly rebuilt.

- Have low internal noise. Both DCR and correlated noise must be low to ensure a low probability of false trigger.

In this context, two experiments, now taking data, FACT [128] and ASTRI [129], are demonstrating that a small telescope can successfully operate having a SiPM–based camera. In particular ASTRI is a prototype of the CTA dual–mirror SST. The first prototype camera had a size of 50x50 cm^2 and employed Hamamatsu MPPCs with 3x3 mm^2 size and 50 μm cell pitch. The MPPCs were connected in matrices 2x2 forming a single logical pixel of the camera having a square size of about 6.2 mm side. Every single logical pixel had a 0.17° imaging resolving angular size. The characterisation of these prototype camera showed a DCR per MPPC of 700 KHz, a crosstalk up to 25 % and a maximum PDE of 40 %. This values were positively evaluated from the ASTRI collaboration because they would allow sufficiently accurate energy measurements on the field [130].

The NUV–HD SiPMs are expected to have a lower noise and a higher PDE than the measured MPPCs, thus they could be considered a better choice for the replacement of the PMTs in the future CTA SSTs. In the fourth chapter, the complete characterisation of this technology will be shown and the obtained values will be compared to the MPPCs data.

Chapter 3

Experimental characterisation: Set-up and procedures

Once a new lot of SiPMs is produced by a manufacturer, a complete characterisation must be performed. The first step is, usually, the measurement of the forward and reverse electrical currents to identify SiPMs with anomalous behaviour. Then, a number of samples are packaged and tested, both in dark and under illumination to extract all the informations. In particular, the characterisation in dark allows to obtain informations about the noise components, primary DCR and afterpulsing and optical cross–talk probabilities, and electrical parameters as the single cell gain and signal shape. The characterisation under illumination gives the PDE of the device. Reliable hardware set–ups and automated acquisition procedures are suggested to reduce the needed time and produce useful data for the comparison of different technologies.

In this chapter, the set–ups and characterisation procedures employed in FBK for every new SiPM production are illustrated. The characterisation in dark is reported in [70] and the one under illumination in [71].

3.1 Characterisation in dark

The hardware set–up used for the dark characterization is shown in Figure 3.1 (original plot taken from [70]). It consists of a light–tight thermostatic chamber containing the SiPM under test with its amplifier board and an outside located oscilloscope. The amplifier board consists of a low–noise, high–bandwidth voltage–feedback operational amplifier with JFET input, connected in a trans–impedance configuration. The low bias–current input stage and the use of an inverting configuration preserve the total signal charge of the SiPM pulses. The gain of the amplifier is $\sim$5000 V/A. The used oscilloscopes have high–bandwidth (typically 1 GHz) and at least 10 GS/s. The operating parameters of the chamber (temperature and humidity rate) as the acquisition parameters of the oscilloscope (e.g. acquisition channel) are re-

motely controlled by the acquisition software at the PC, written in LabView.

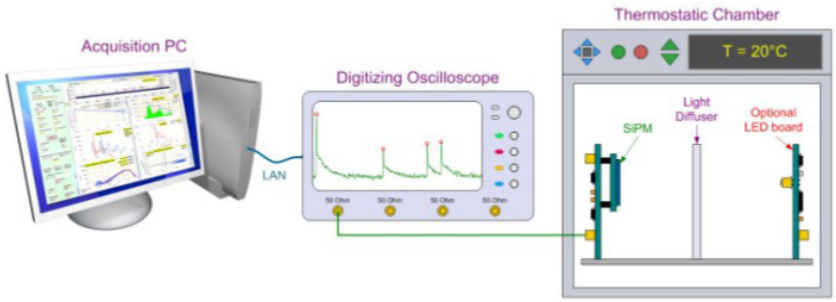

Figure 3.1: The set–up for the characterisation in dark is represented. The picture is taken from [70]. The SiPM is placed inside a thermostatic light–tight chamber with the amplifier board. The signal is sent to an external oscilloscope and then to the acquisition software in the PC.

The on–line analysis is performed acquiring random millisecond–long waveforms of SiPM output signals.

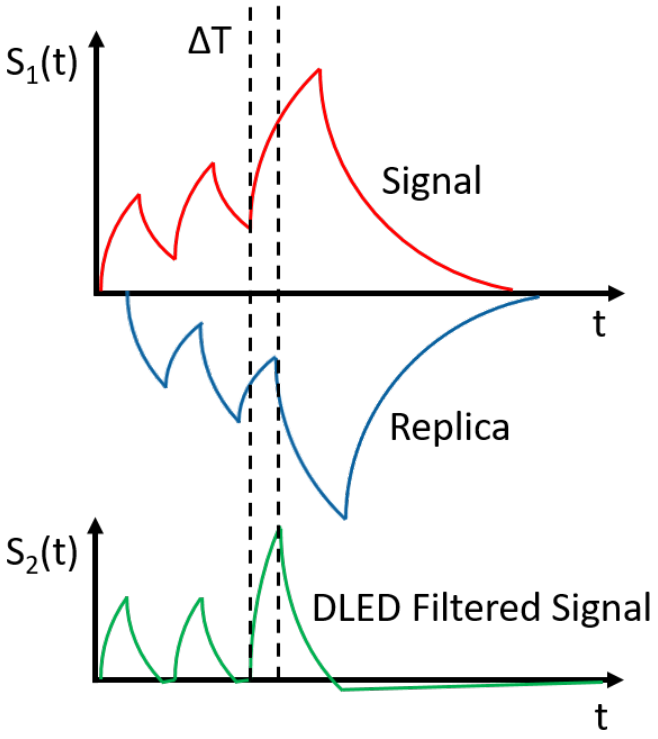

Figure 3.2: The DLED technique is represented. A replica of the original waveform (blue line) is delayed and subtracted from the original one (red line), to reduce the slow exponential tail. In the original waveform a pile–up of signals is visible, in the filtered one this phenomenon is absent.

A filter, called Differential Leading Edge Discriminator (DLED) [94], is employed in order to better identify the signals and avoid possible baseline fluctuations and pile–up of consecutive ones. The DLED concept uses the original SiPM waveform to obtain a baseline–compensated signal by calculating the difference between the measured signal and its delayed replica by a time interval ΔT. Then, a standard leading edge discriminator (LED) is applied to the obtained waveform for the estimation of the arrival time of the event. A schematic representation is presented in Figure 3.2. The $S_2(t)$ is the filtered waveform. In the original waveform, the pile–up of consecutive signals is present, while it is compensated in the filtered waveform.
The effects of the DLED method are the reduction of the signal long tail and its amplitude. The set ΔT has influence on the amplitude of the filtered signal because this is equal to the variation of the original signal during the delay. This delay must not be too small, otherwise also the rising edge of the signal would be attenuated down to a level such as the electronic noise starts affecting the waveform, and not larger than the rise time of the signal, to avoid a too big undershoot. Usually, a value of several hundreds of picoseconds, less than 1 ns, is a good compromise. The effect of the ΔT choice on the filtered signal is shown in Figure 3.3 (original plot taken from [94]).

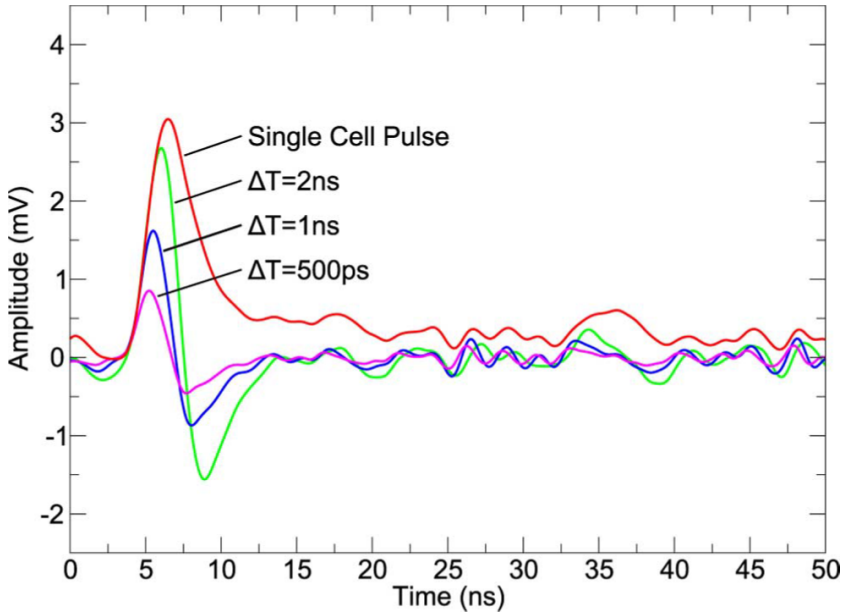

Figure 3.3: A SiPM signal and three DLED filetered ones, with different chosen ΔT, are represented. The picture is taken from [94]. The filtered signal amplitude reduces with ΔT.

To get rid of the undershoot, a small number of signals, well separated from previous and subsequent ones, are initially acquired during the on–line analysis and the average DLED signal is calculated. Then, this is subtracted to the filtered acquired waveforms.

In each filtered acquired long waveform, the amplitude and the arrival time of every identified pulse, imposing a threshold (usually set to half of the single cell amplitude), are saved. The pulse amplitudes, scaled to the single cell signal one, and the time distances (time between a pulse and the precedent one) are used to build a scatter plot, as the one represented in Figure 3.4. In this scatter plot, all the noise components are visible:

- the events with single amplitude and time distance up to tens of microseconds are mainly the primary dark counts;
- the events with fractional amplitude are afterpulsing (events occurring after the total recharge of the cell, having integer amplitude, are included in the primary dark counts cloud and are separated by the analysis procedure);
- the events with double amplitude and same time distribution of the primary dark counts are the DiCT events;
- the events with single amplitude and very small time distance, up to a few tens of nanoseconds, are the DeCT events (as for the afterpulsing, they are separated from the primary dark counts by the analysis procedure).

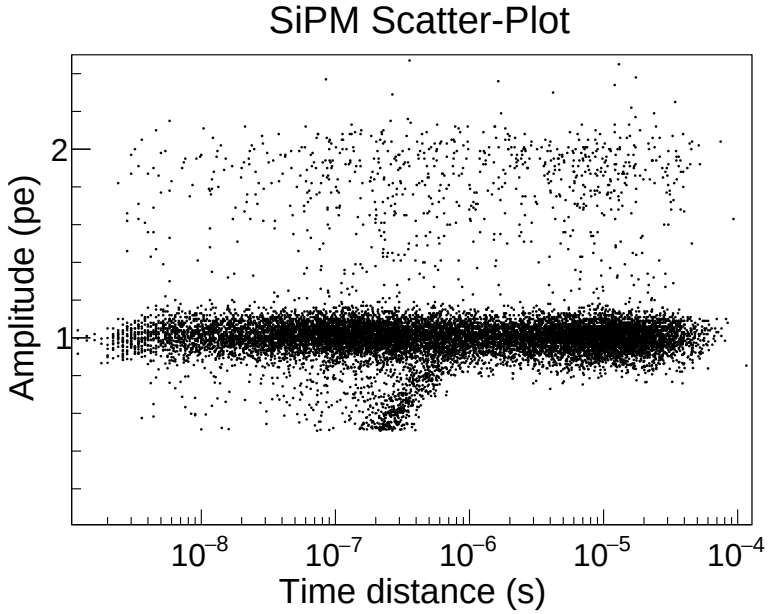

Figure 3.4: Example of a scatter plot amplitude - time distance of SiPM signals obtained with the characterisation explained in [70]. In the Y axis, the ratio between the acquired signal amplitude and that of the single cell is reported to express the acquired data as number of fired cells (photoelectrons, pe). The X axis reports the time between two consecutive pulses.

The projection of the scatter plot along the amplitude axis is reported in Figure 3.5. The event rate is obtained by dividing the number of events in every acquired waveform by the time window. The black histogram represents the acquired data, the red curve is the cumulative histogram. The red histogram is a staircase plot, as the one shown in Figure 1.13.

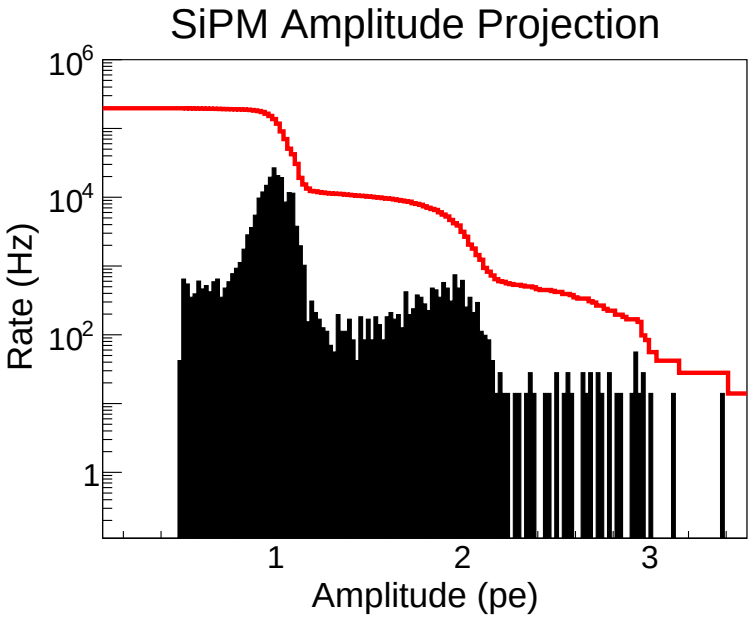

Figure 3.5: The projection of the scatter plot reported in Figure 3.4 along the amplitude axis. The cumulative histogram is also shown in red. The cumulative histogram is a staircase plot from which the total noise and the DiCT probability can be calculated.

The first "stair" is the total noise, including the DCR and all the delayed correlated noise events. In this projection, the total noise corresponds to the maximum of the red histogram, because the trigger acquisition is set at half the amplitude of the single cell. The following equations (3.1) give the DiCT probability, P_{DiCT}, and its uncertainty, ΔP_{DiCT}.

$$P_{DiCT} = \frac{R_{1.5}}{R_{0.5}}, \qquad \Delta P_{DiCT} = P_{DiCT}\sqrt{\frac{1}{R_{1.5}} + \frac{1}{R_{0.5}}} \tag{3.1}$$

In the equations (3.1), $R_{0.5}$ and $R_{1.5}$ are defined as in the section 1.3.1. The probability to have a primary double amplitude event is completely neglected because it is always very small, much less than the DiCT uncertainty. It can be derived from the law (1.10) with Δt equal to a few ns, due to the use of the DLED filter.

In Figure 3.6, the projection of the scatter plot along the time distance axis is reported. Due to the used variable bin size, the aspect of this projection

differs from what is expected, a decreasing exponential distribution. The used fit function to represent the primary dark counts is defined by the law (3.2).

$$F(t) = aP(t) = a(te^{-bt}) \tag{3.2}$$

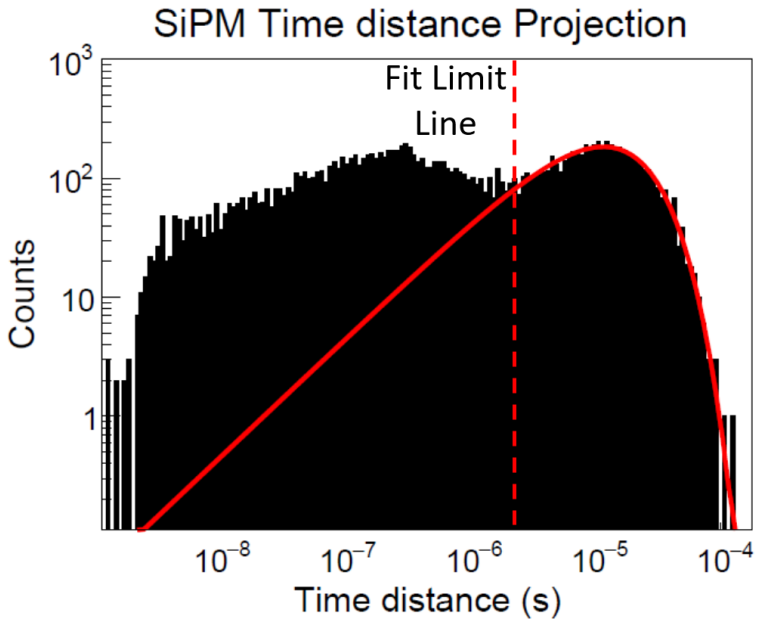

Figure 3.6: The time distance projection of the scatter plot in Figure 3.4, with a variable bin size, is shown. The function (3.2) is used to fit the primary dark counts and is drawn in red. Only data with time distance larger than the Fit Limit Line are used in the fit procedure. The visible excess of events at time distances smaller than the Fit Limit Line are delayed correlated noise, both DeCT and AP.

In the equation (3.2), a is a normalization factor and P(t) is the probability to have an event at the time distance t. The b parameter is the primary dark count rate, the DCR. The fit procedure uses the right part of the experimental data (data with time distance larger than the Fit Limit Line). On the right part of this limit, the fit well describes the experimental data, while at shorter times, the histogram is altered by the delayed correlated noise events. Including these events in the fit procedure, the measured DCR would result artificially increased, as shown in Figure 3.7, in which the extracted DCR of the data in Figure 3.6, as a function of the Fit Limit Line position, is reported. The plot can be divided into three regions:

- I)positions between the maximum time distance and the maximum measured counts (10^{-5} s): the obtained DCR changes from very low values to $\sim 10^5$ Hz, about the inverse of the maximum measured counts time distance;

- II)positions between the maximum measured counts and the beginning of the visible delayed correlated noise components ($\sim 2\times10^{-6}$ s): all the extracted DCRs are in agreement within 1σ;
- III)positions between the beginning of the visible delayed correlated noise components ($\sim 2\times10^{-6}$ s) and the minimum time distance: the DCR increases to values not in agreement with those measured in the region II.

The plot in Figure 3.7 shows the importance to correctly position the Fit Limit Line in the region II to estimate the DCR without errors. From Figure 3.7, the relative DCR uncertainty is visible, it is about 2–3 %.

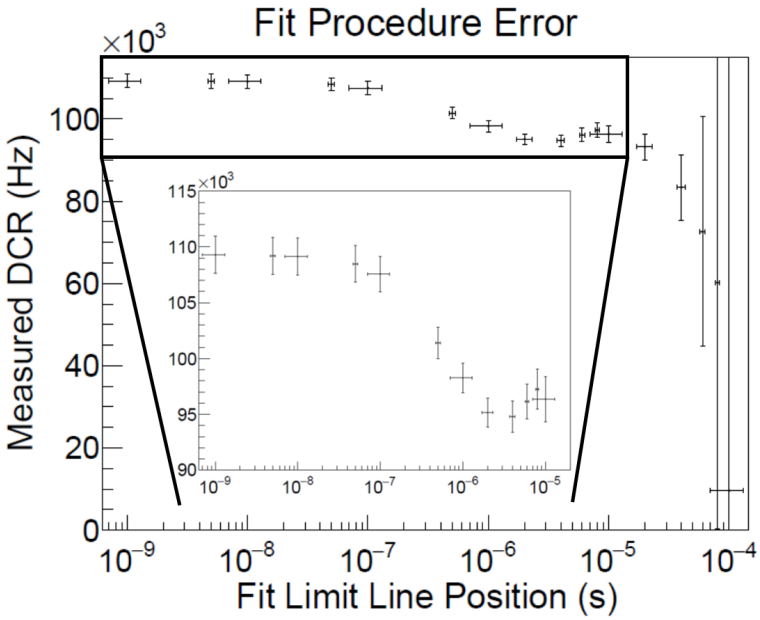

Figure 3.7: The measured DCR, as a function of the Fit Limit Line position, is shown. Inside the plot an enlargement shows the increasing DCR including the delayed correlated noise events in the fit procedure.

In the region III of Figure 3.6, the delayed cross–talk events and the afterpulsing ones are present. Both the probabilities of the delayed noise components are calculated as the ratio between the counts in excess and the total acquired events in a chosen time interval (t_2-t_1). For clarity, the used equations to calculate a generic delayed noise probability and its uncertainty are the (3.3).

$$P_{DN} = \frac{N_{DN} - N_{Fit}}{N_{Ev}}, \qquad \Delta P_{DN} = P_{DN}\sqrt{\frac{N_{DN} + \Delta N_{Fit}{}^2}{(N_{DN} - N_{Fit})^2}} \tag{3.3}$$

N_{DN} is the number of acquired events and N_{Fit} is the integral of the fit function in the considered time interval. It allows to calculate the expected number of

primary events. N_{Ev} is the total number of acquired events. The error on N_{Fit}, ΔN_{Fit}, must be propagated from the equation (3.2) and it is proportional to the parameter errors, Δa and Δb. Since these errors are usually very small, less than 1 %, the ΔN_{Fit} is small too. The error on the delayed correlated noise probability is strongly dependent from the number of acquired events due to the difference $(N_{DN}\text{-}N_{Fit})^2$. If this number is not large enough, the results are nor reliable. This aspect is critical when Low–AP devices must be measured because the expected small number of delayed correlated noise events. The two noise components can be clearly separated because the AP cloud of events do not occur at time distances shortest than a minimum due to the set threshold (in Figure 3.4 this minimum is observable at about 100 ns). For this reason, in the case of the AP probability estimation, t_1 can be chosen as the minimum measured AP cloud time distance and t_2 as the time distance at which the excess of events begins visible (usually it coincides with the Fit Limit Line time). In the case of the DeCT probability estimation, t_1 can be chosen as the minimum measured time and t_2 as the chosen t_1 of the AP case. In general, for the Low–AP devices it is better to sum the delayed correlated noise probabilities to increase the acquired events and reduce the errors.

The on–line analysis allows also to calculate the single–cell gain, signal features as the average amplitude and the recharge time and the Excess Charge Factor (ECF). These informations are obtained from the original waveform, not filtered by the DLED method.
The time stamp of every acquired signal is used to integrate the original waveform after and before this time for a set window. If the window is set equal to the signal duration, the measured area after the time stamp is the signal area while the other can be considered as a baseline estimation. Two histograms with the calculated areas are then built, as the ones represented in Figure 3.8. The first peak of each histogram is then fitted with a Gaussian function to obtain the peak areas and errors. The single–cell gain of the device is calculated using the equation (1.6) considering the first peak of the baseline histogram as the pedestal (A_0) and the first peak of the signal area histogram as the term A_1 of this equation.
After an imposed number of events is acquired, and the peaks in the charge spectrum shown in Figure 3.8 are clearly visible, every additional signal having an area falling in the first peak of the signal area histogram is summed up and averaged. The average signal is the single–cell output of the detector without the baseline fluctuations, compensated by the average. On this signal, it is possible to define the average amplitude and the typical recharge time.
At last, having measured the IV of the device and calculated the DCR and the gain of the single–cell signal, the electrical current due to the primary events can be calculated and the ECF obtained from the equation (1.12).

The reported characterisation must be performed at different overvoltages and, possibly, at different temperatures to observe how the important param-

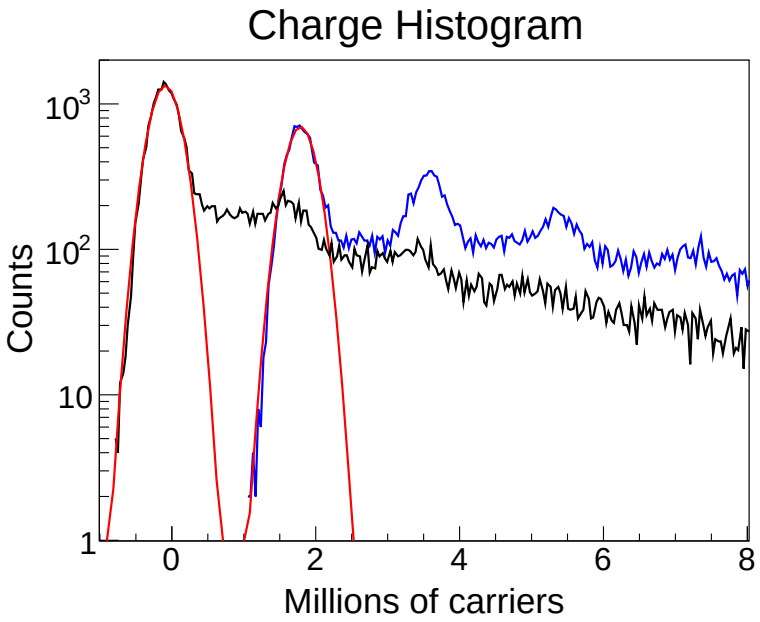

Figure 3.8: The measured signal area and baseline histograms are plotted. The first peak of each histogram is fitted with a Gaussian function to obtain the corresponding area and error.

eters of a new lot vary with the bias voltage and environment temperature.

3.2 PDE measurement

In this section, the set–up and methods used to estimate the PDE of a device are illustrated [71]. A large number of preliminary operations and precautions are performed to have a reliable set–up. For this reason, it seems better to divide this section into two subsections and fully describe the set–up calibration and uncertainty sources in the first one and the PDE estimation methods and analysis in the last.

3.2.1 Set-up calibration and uncertainty sources

The main elements of the employed optical bench set–up are contained in a light–tight box. A scheme representing them is shown in Figure 3.9 (original plot taken from [71]). The set–up consists of an integrating sphere with inner diameter of about 5 cm and three circular ports of about 1 cm diameter placed at 90 degrees one with respect to each other. One port (a) is used to introduce the light into the sphere, either with an optical fibre or by directly mounting an LED on it; on a second port (b), a reference photodiode (not necessarily calibrated) is mounted on to monitor the optical power inside the sphere (this port is recessed to avoid direct light exposure from the incident light to the

active area of the photodiode); the last port is used to illuminate the device, placed at a fixed distance from the sphere. As already shown in [131], locating the device at some distance from the sphere, instead of directly mounting on it, has two advantages. The first one is the possibility to have a very different light flux on the device under test and on the reference photodiode used for calibration (as explained in the following). This is important because the photodiode has not an internal gain, thus it needs a larger light flux to give a measurable signal. The second advantage is a better light uniformity on the device surface. The tested device can be either connected to an amplifier board, and then the output signal acquired by an oscilloscope (this solution is very similar to that shown in the section 3.1), or simply connected to a picoammeter to measure its current, depending on the chosen measurement method. The set–up is so compact that it can be put inside the thermostatic chamber, instead of inside the light–tight box, to perform measurements at different temperatures to investigate any possible variation.

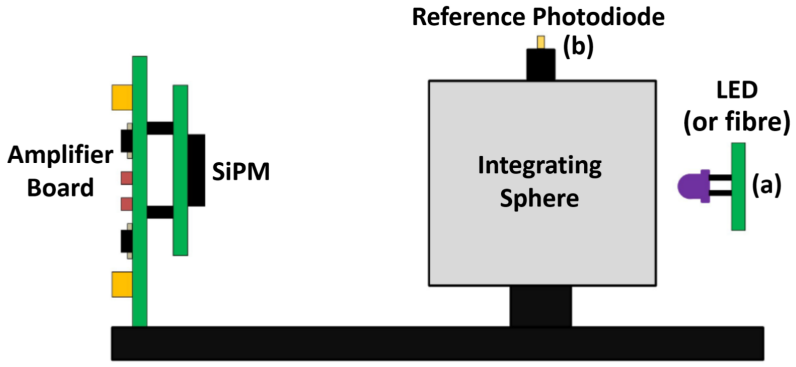

Figure 3.9: Scheme of the main components of the experimental set–up inside the light–tight box. The original plot is taken from [71]. An integrating sphere with three ports is present. On a port, an optical fibre, or an LED, is connected to send the photons inside the sphere; on a second port, a reference photodiode monitors the light stability; the last port is used to illuminate the device under test.

Two different light sources can be used in the employed set–up: a 20 W tungsten halogen lamp with a color temperature of about 3000 K having a broadband spectrum peaked in the near IR region (in this case the desired wavelength is selected with a monochromator [132] with 9 nm FWHM resolution); a set of LEDs with peak wavelength ranging from UV to near IR region. The main reason to have two different light sources is the possibility to use the LEDs for a pulsed measurement method. Table 3.1 lists the main characteristics of the used LEDs (central wavelength and expected FWHM) as reported in the manufacturers datasheets. The datasheets do not allow to perfectly know the LEDs emission spectra. An uncertainty on the central wavelength of at least 10 nm is given for almost all the LEDs by the manufacturers. For this

reason, a procedure is employed to directly measure the LEDs emission spectra using the monochromator. The procedure is the following: an LED is placed as the light source of the monochromator and the light output is measured, as a function of wavelength, using a calibrated photodiode. This operation is then repeated varying the applied bias voltage to the LED. Examples of the obtained spectra are shown in Figure 3.10.

Table 3.1: LEDs manufacturer characteristics (Roithner LaserTechnik[(a)][133], Thorlabs[(b)])[134].

LED id.	Nominal WL (nm)	Central WL (nm)	FWHM (nm)
UVTOP295-HL-TO39[(a)]	300	295 ÷ 305	12 ÷ 15
UVTOP315-HL-TO39[(a)]	320	315 ÷ 325	10 ÷ 20
UVTOP335-HL-TO39[(a)]	340	335 ÷ 345	15 ÷ 20
XSL-365-5E[(a)]	365	363 ÷ 370	10 ÷ 20
LED380L[(b)]	380	375 ÷ 380	12
VL390-5-15[(a)]	390	385 ÷ 395	N/A
XRL-400-5O[(a)]	400	400 ÷ 410	10 ÷ 20
LED410L[(b)]	410	405 ÷ 410	20
LED420-33[(a)]	420	415 ÷ 425	15
LED435-12-30[(a)]	435	430 ÷ 435	N/A
LED450-06[(a)]	450	440 ÷ 460	25
LED465E[(b)]	465	455 ÷ 475	25
LED525EHP[(b)]	525	520 ÷ 530	35
LED545-06[(a)]	545	535 ÷ 555	40
LED591E[(b)]	590	580 ÷ 600	17 ÷ 23
LED630E[(b)]	630	629 ÷ 649	17
LED700-02AU[(a)]	700	700	30
LED780E[(b)]	780	770 ÷ 790	30
ELD-950-535[(a)]	950	935 ÷ 960	65

After the measurement, along with the correct emission spectra of the LEDs, an unpredictable and unexpected correlation is found between the applied bias voltage and the emission spectra central–wavelength. In particular, a central–wavelength shift is observed. In some cases, the shift is toward longer wavelengths, as for the LEDs 700 nm and 780 nm, while in others, toward shorter ones, as for the LED 525 nm. No reason is found yet for this different behaviour. It is very interesting to note that this correlation is found even if the applied bias voltage is always in the linear region of the forward IV curve of the LEDs and the measurements are performed after a warm–up time in which the LEDs stabilise. These measurements allow to specify a proper applied bias voltage range for each LED in which no appreciable variation in the emission spectra is observed. This range is always respected during the following measurements.

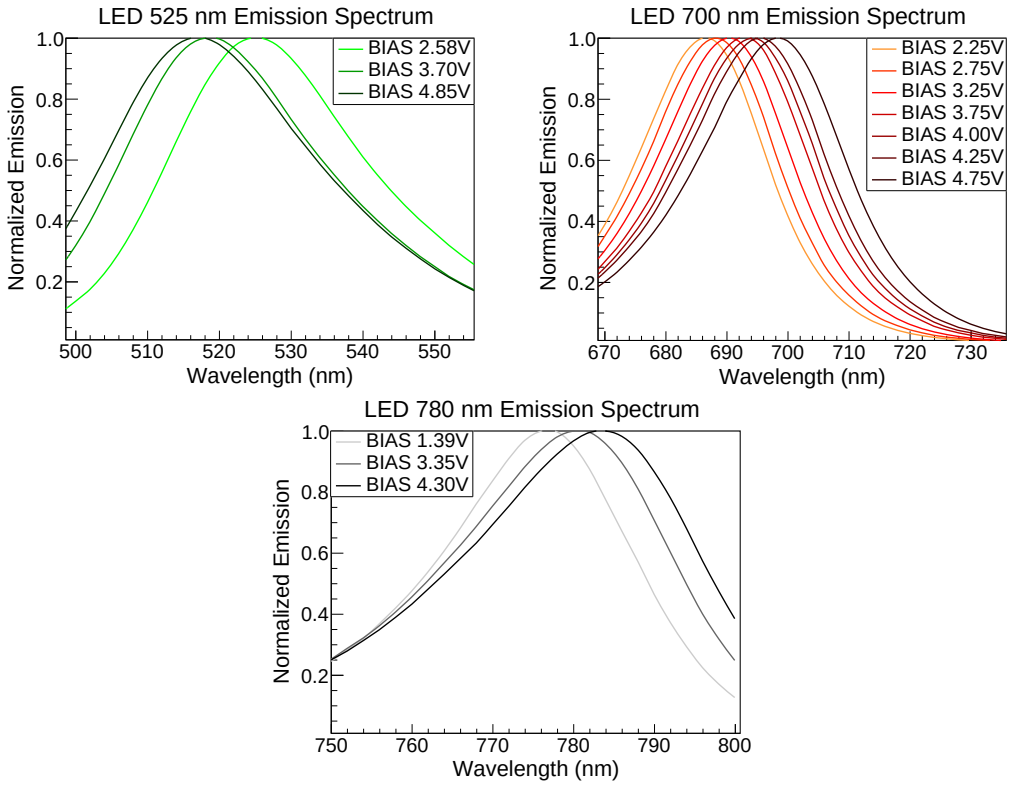

Figure 3.10: Measurement of the emission spectra, as a function of wavelength, for different applied bias voltages, of the LEDs with nominal peak wavelength 525 nm (top left), 700 nm (top right) and 780 nm (bottom). A central wavelength shift is observable. In the first plot, the central wavelength reduces with the bias voltage, in the other two the measured behaviour is the opposite.

In Table 3.2, the emission spectra characteristics of the measured LEDs, in the operating conditions, are reported. Since the employed monochromator has an operating range from 360 to 800 nm, five LEDs can not be measured (with nominal wavelength equal to 300 nm, 320 nm, 340 nm, 365 nm and 950 nm), thus the datasheet features are considered during the measurements. Their characteristics are not reported in Table 3.2 because they are just shown in Table 3.1.

The emitted light, both by the lamp and by the LEDs, is collected on a multimode optical fibre with inner diameter of 1 mm and sent to the integrating sphere through its port. This arrangement allows to place the light sources outside the light–tight box, assuring that the environmental conditions of the device under test did not suffer large variations during the change of the investigated wavelength. The deepest UV LEDs, with peak wavelength shorter than 350 nm, are an exception because they are directly mounted on the sphere. This is necessary to avoid unwanted effects of the fibre on the outgoing light, as discussed later in this subsection.

Table 3.2: Measured characteristics of the LEDs emission spectra.

LED id.	Central WL (nm)	FWHM (nm)
LED380L[(b)]	380	18
VL390-5-15[(a)]	393	18
XRL-400-5O[(a)]	398	16
LED410L[(b)]	407	20
LED420-33[(a)]	417	24
LED435-12-30[(a)]	428	22
LED450-06[(a)]	443	27
LED465E[(b)]	468	32
LED525EHP[(b)]	519	34
LED545-06[(a)]	533	41
LED591E[(b)]	590	19
LED630E[(b)]	639	23
LED700-02AU[(a)]	697	29
LED780E[(b)]	782	33

The calibration of the light sources allows to obtain the relation between the electrical current measured by the reference photodiode and the number of photons per unit time and area reaching the SiPM location (Ph_I). The calibration procedure is performed using a calibrated photodiode and paying attention that its active area is in the exact position of the SiPM during the subsequent measurements. Knowing the responsivity of the calibrated photodiode, η, and its active area, A, Ph_I can be expressed as:

$$Ph_I = \frac{I_{CAL-L} - I_{CAL-D}}{Ah\nu\eta} \tag{3.4}$$

in which $I_{CAL\text{-}L}$ and $I_{CAL\text{-}D}$ are the electrical currents read in light and in dark condition by the calibrated photodiode, respectively, h is the Planck constant and ν the frequency of the adopted light. The error on Ph_I must be propagated from the electrical current measurement errors, always lower than 1 %, and from the errors of the other parameters. To minimise the uncertainty related to this procedure, the calibration is usually repeated for different light intensities. Using the LEDs, this can be obtained varying the bias voltage, always inside the found acceptable range in which the emission spectrum do not show variations, while using the monochromator, varying the size of a collimator in front of the entrance slit. This procedure gives plots similar to the one reported in Figure 3.11. A typical uncertainty in the order of 1 % or less is found for all the LEDs and in the order of 5 % or less for the monochromator lamp.

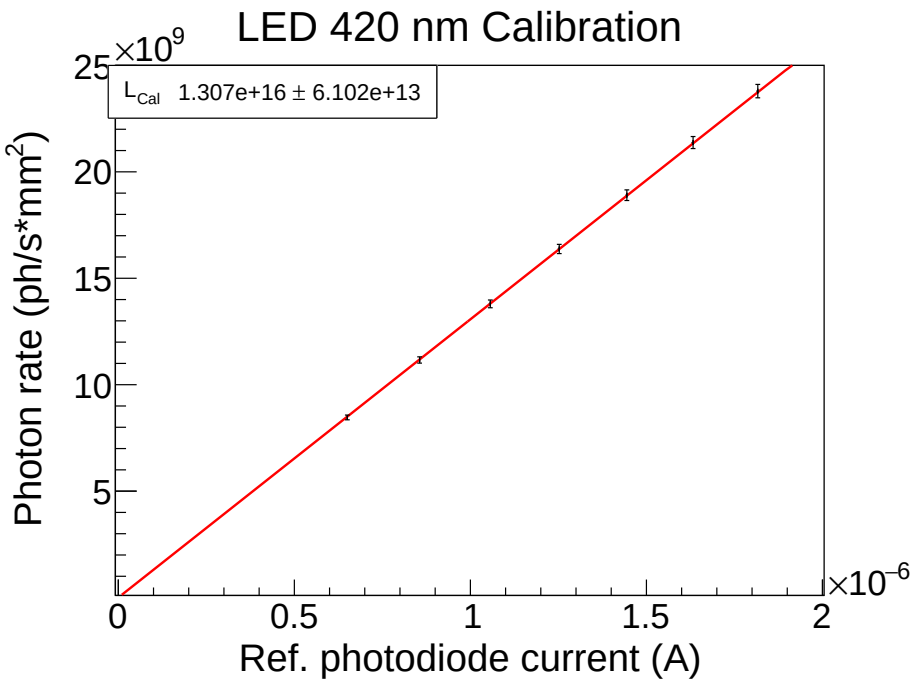

Figure 3.11: Example of calibration plot for the LED with nominal wavelength equal to 420 nm. Inside the plot, the obtained calibration value with its error is reported.

A comparison between the calibration values of the LEDs and the monochromator lamp is reported in Figure 3.12. A very good agreement between the light sources is found for wavelengths longer than 420 nm. For shorter wavelengths, the LED calibration values are always larger than the corresponding ones calculated with the monochromator. The poor emission light of the 20 W lamp at these short wavelengths does not allow a reliable current measurement with the calibrated photodiode. For these reasons, the monochromator values are considered not reliable and only the LEDs are used to measure the PDE of the devices in the short wavelength range, up to about 420 nm.

One of the proposed PDE measurement methods, discussed in the following subsection 3.2.2, uses LEDs operated in pulsed mode, so the calibration procedure was repeated for LEDs driven by a pulser with 50 MHz bandwidth. In these tests, many parameters of the voltage pulse applied to the LED were varied. Among these, the repetition period of the pulser in the range $(10^{-7} \div 10^{-3})$ s and the pulse duty cycle, from 0.1 % to 50 %. The obtained results were consistent with the predictions derived from the continuous calibrations for all the LEDs. As an example of these tests, the pulsed calibration of the LED with nominal wavelength equal to 420 nm is shown in Figure 3.13. The repetition period of the pulse generator was varied from 1 μs to 100 μs, maintaining a fixed pulse width equal to 100 ns. As expected, the reference photodiode electrical current linearly increases with the pulse frequency (inverse of the repetition period).

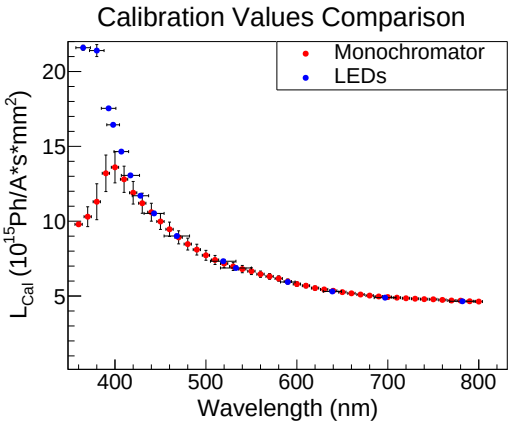

Figure 3.12: Comparison between the calibration values of the LEDs and the 20 W lamp. A good agreement is found for the LEDs with nominal wavelength longer than 420 nm.

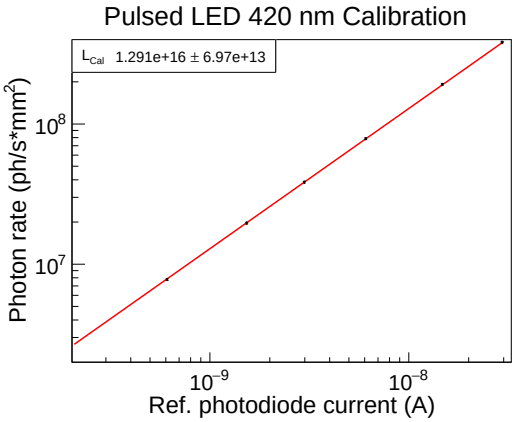

Figure 3.13: Example of calibration plot for the LED 420 nm operated in pulsed mode. The period of the pulse generator was varied in the range (1÷100) μs, fixing the pulse width to 100 ns.

Another important parameter to be checked is the spatial uniformity of the light at the SiPM location. As written above, the distance of the SiPM from the sphere would help to obtain a good spatial uniformity. To measure it, a square SPAD with 40 μm size is used. Since the SiPM position is at about 10 cm from the sphere, the SPAD can be considered as a point–like detector. The SPAD is moved, using two micropositioners, in an x–y plane orthogonal to the light propagation at the SiPM distance. Its current is measured on a set of grid points (500 μm far apart each other) creating the intensity plot shown in Figure 3.14. As expected, the light intensity shows a maximum in the center and a decreasing value increasing the distance from this point following a circular symmetry. In Figure 3.15, a plot shows the light intensity measured along the central axis. The maximum measured variation in the

spatial range investigated (about 2x2 cm^2 around the SiPM location, i.e. the center of the plot) is about 3 %. However, since the SiPM holder limits the maximum misalignment of the device to about 5 mm, the maximum light intensity variation reduces to about 2 %. This is chosen as the error associated to the SiPM positioning and the angle of incidence of incoming photons.

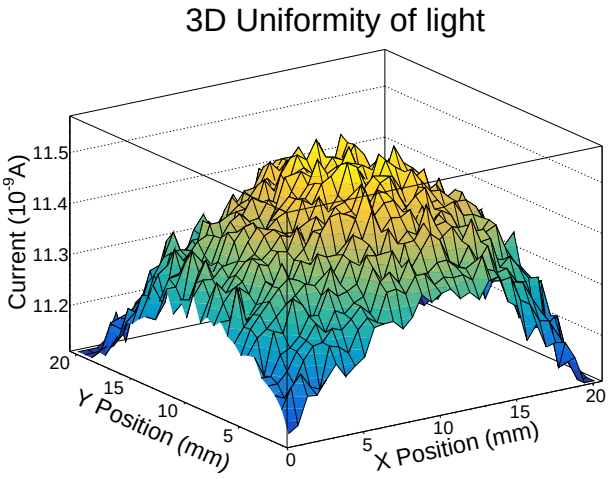

Figure 3.14: Uniformity of the incoming light at the SiPM location obtained measuring the electrical current of a square SPAD with 40 μm cell pitch moved in a x–y plane orthogonal to the light propagation.

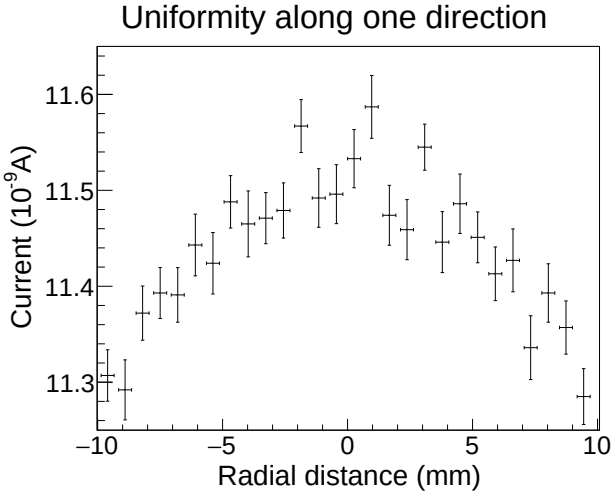

Figure 3.15: Projection of the light intensity along the central axis of the uniformity measurement.

At last, the transmission of the optical fibre is verified. Since the fibre is not optimised to transmit deep UV light, the calibration procedure described

above is repeated connecting all the LEDs directly to the port of the integrating sphere. If the light emission spectrum of the source is not influenced by the optical fibre, a perfect match between the measurements with and without the fibre is expected. This is found for all the LEDs having nominal wavelength larger than 350 nm. For the deepest UV LEDs, a large variation is measured. An example of these last measurements, the calibration of the LED with wavelength equal to 300 nm inside and outside the light–tight box, is shown in Figure 3.16. The different and incompatible calibration values found in the two conditions, LED inside and outside the sphere, are an important clue that the optical fibre is not perfectly transparent in the deep UV range. For this reason, the fibre can not be used to transport the light of the deep UV LEDs and it is chosen to place them directly mounted on the sphere.

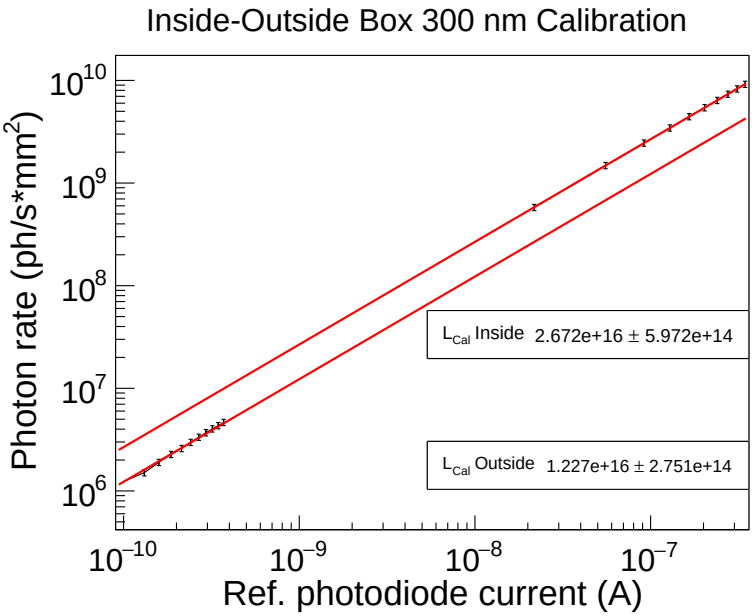

Figure 3.16: Example of calibration for the LED with nominal wavelength equal to 300 nm directly mounted on the sphere inside the box (dashed line) or connected to the optical fibre outside the box (continuous line). The calibration values, reported inside the plots with their errors, are clearly different and incompatible.

Besides the set–up errors discussed above (associated to the light calibration, to the SiPM positioning and to the transparency of the optical fibre), the statistical errors, due to the chosen measurement method, are summed up during the measurement. These kind of errors will be discussed for each method in the following subsection 3.2.2.

3.2.2 Methods and analysis

Three different methods are developed to measure the PDE of the SiPMs. In this subsection, they are shown with the possible drawbacks and solutions. In the first two presented methods, a continuous light source must be used, thus both the monochromator lamp and the LEDs can be employed. In the last method, a pulsed light is needed, thus only the LEDs, driven by a fast pulser, can be used.

The first presented method is based on the pulse counting under continuous light illumination and is called Continuous Counting Method (CCM). This method is derived from the procedure developed for the characterisation in dark of SiPM discussed in detail in the section 3.1. The analysis is performed both in dark and in light condition. The equation (3.2) allows to calculate the Count Rate (N_L) under illumination and the DCR (N_D) in dark. The N_L is the sum of events generated by impinging photons and by thermal/tunnelling excitations. Subtracting N_D from N_L, the required number of detected photons, N_P, is obtained. From the current of the reference photodiode, measured both in light ($I_{REF\text{-}L}$) and in dark ($I_{REF\text{-}D}$), and knowing the light calibration value for the employed light (L_{Cal}), the number of impinging photons (Ph_I) is also known. Then, the equation (3.5) is used to calculate the PDE of the device.

$$PDE = \frac{N_P}{Ph_I} = \frac{N_L - N_D}{(I_{REF-L} - I_{REF-D}) \times L_{Cal}} \tag{3.5}$$

This method allows to calculate the PDE free from every type of correlated noise influences because only the primary events are considered during the estimation of N_L and N_D. The main drawback is the measurement duration, especially in dark condition. Actually, it can take several minutes to reach the needed statistics and it has to be repeated for every bias voltage and interested wavelength. The sources of error of this method are the determination of N_L and N_D and the statistical fluctuations of the reference photodiode electrical current. Typical uncertainties for these quantities are a few percent or less. The N_L uncertainty is related to the statistics of the fit procedure. This statistics can be low if N_L is very high or the delayed noise probability is large. Actually, in both cases, a small number of the acquired events are useful to calculate N_L (only those events on the right of the Fit Limit Line position of Figure 3.6). For this reason, during the light measurements, a low level light regime is required. It is also better to use small devices to deal with a low N_D (1x1 mm^2 is usually a good compromise).

The second method is based on the photocurrent measurement and is called Photocurrent Method (PM). It is not very different from some methods just described in literature [135] but it improves these techniques considering the influence of the correlated noise components to the electrical current. Once

the ECF factor is known from the characterisation in dark, it is possible to use this parameter also illuminating the device, because the correlated noise probabilities are independent from the light condition (actually, the afterpulsing probability depends on the trap release time and the cross–talk probability on the secondary photons transmitted from a cell to an adjacent one). From the formula (1.12) it is easy to derive the equation (3.6) from which the PDE can be calculated.

$$PDE = \frac{I_{SiPM-L} - I_{SiPM-D}}{G \times q_e \times ECF \times Ph_I} \tag{3.6}$$

In the equation (3.6) $I_{SiPM\text{-}L}$ and $I_{SiPM\text{-}D}$ are the SiPM currents in light and in dark conditions, respectively, G is the gain of the SiPM at the operated bias voltage and q_e is the electron elementary charge. With this method it is possible to get rid of the contributions from all the noise components, both primary and correlated, because the estimation of the ECF and the dark current subtraction. In addition, it is relatively fast, so it is particularly useful for measurements with the monochromator, in which, in general, a wide range of wavelengths is investigated, so the measurement time is a critical aspect. The typical sources of error are the estimation of the ECF and the statistical fluctuations of the photodiode and SiPM currents. These errors are, usually, in the order of 1 % or less. The ECF error is calculated propagating the errors of the free parameters in the equation (1.12). Typical uncertainty for the ECF is a few percent.

The last proposed method is based on the use of pulsed light using a fast pulser, with typical rising and falling edges of a few nanoseconds, to drive the LED and provide also the trigger to the oscilloscope. It is called Pulsed Counting Method (PCM). To be sure that any photogenerated event is acquired, a preliminary time characterisation of the LED signal is required. A time histogram of the SiPM pulse delay with respect to the trigger signal is built, using a very short pulse (typically several tens of nanoseconds). In general, the LED time emission spectrum is very similar to the voltage pulse applied, thus the LED does not emit photons after the the voltage signal is turned off. In some case, however, the LED emits photons far after the bias voltage signal is turned off, thus this characterisation has a critical importance.
The PDE measurement consists of acquiring the saved waveforms on the oscilloscope, then, a dedicated software, calculates the charge of every pulse and builds a charge histogram. The same procedure is performed both in light and dark conditions, simply setting the LED bias voltage to zero, while still triggering the oscilloscope. From the two charge histograms, the average number of fired cells in light and in dark can be calculated, knowing that the pedestal peak, being the peak of events in which no event is detected, is the only one not affected by the correlated noise. Actually, the charge spectrum should follow a Poisson statistics, as the incoming photons do, but only the pedestal peak

really follows this statistics. For this reason, it is possible to calculate the average number of detected photons from its statistics, using the equation (3.7). This kind of analysis is well known in literature, as explained in [131, 136, 137].

$$P_0 = e^{-N_F} \frac{N_F^0}{0!} = e^{-N_F} \tag{3.7}$$

In the equation (3.7), P_0 is the probability to have no detection in the charge spectrum and N_F is the average number of the fired cells. Subtracting the N_F calculated in the dark measurement from the one calculated in the light, the average number of detected photons, N_P, is determined. The ratio between N_P and the impinging photons gives the PDE.

$$PDE = \frac{N_P}{Ph_I} \tag{3.8}$$

This method can be used for every LED (covering the entire spectrum from deep UV to NIR region) getting rid of both cross–talk and afterpulsing events in the N_P estimation. Only afterpulsing happening with a time delay equal to the repetition period of the pulser can artificially increase N_P because these events can be acquired in the following oscilloscope time window. Thus, the repetition period must be set long enough to reduce this probability. The main drawback of this method is the total required time to perform a measurement because it has to be repeated for every bias voltage and every LED. The statistical fluctuations of the reference photodiode current and the statistical errors related to the pedestal peak are the main sources of errors. The statistical error on the pedestal peak is reduced acquiring a high number of events and the instrument error on the current measurement is usually lower than 1 %.

The previously discussed methods can be adapted to measure the PDE of the SPADs. The measurement of a SPAD is much easier and precise than the corresponding one of a SiPM because it has no optical cross–talk, so its correlated noise component is only the afterpulsing.
In particular, the CCM can be used with a SPAD without any variation. The main problem is that, due to the low DCR of a single cell device, the measurement time increases to hours to reach a good statistics.
The PM could be used without any variation too, but usually it is not feasible because the SPAD dark current is usually very small, under the sensitivity of the current measurement instrument. For this reason, it can be very difficult to correctly subtract it from the measured photocurrent in light condition and the equation (3.6) could not be used anymore in a reliable way.
The PCM can be used as described before but it is also possible to acquire the SPAD signals and measure the maximum amplitudes in every time window, instead of the signal charges, and build an amplitude histogram. The afterpulsing events happening during the recharge of the device are not present in

the amplitude histogram because they have always a smaller amplitude than the primary ones, as written in the section 1.3.1. As just written for the SiPMs, the repetition period of the pulser must be set long enough to reduce the probability that afterpulsing events, happening after the total recharge of the device, can affect the measurement. In Figures 3.17 and 3.18, a charge and an amplitude histogram of a SPAD, under the same light illumination and at the same bias voltage, can be compared.

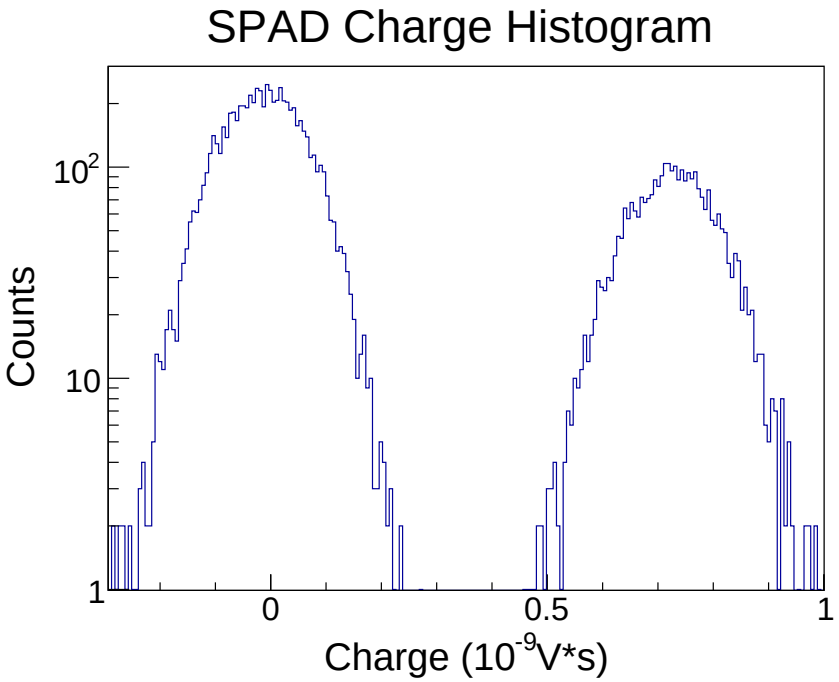

Figure 3.17: Charge spectrum of a SPAD, operated at a bias voltage 1 V over the breakdown voltage.

The two histograms appear very similar, thus the two possibilities can be considered equivalent to calculate the average number of detected photons.

In the next section, a comparison between the written methods will be shown. In addition, a comparison between the measurements on a SiPM and on a SPAD, having the same layout of a SiPM cell, is shown.

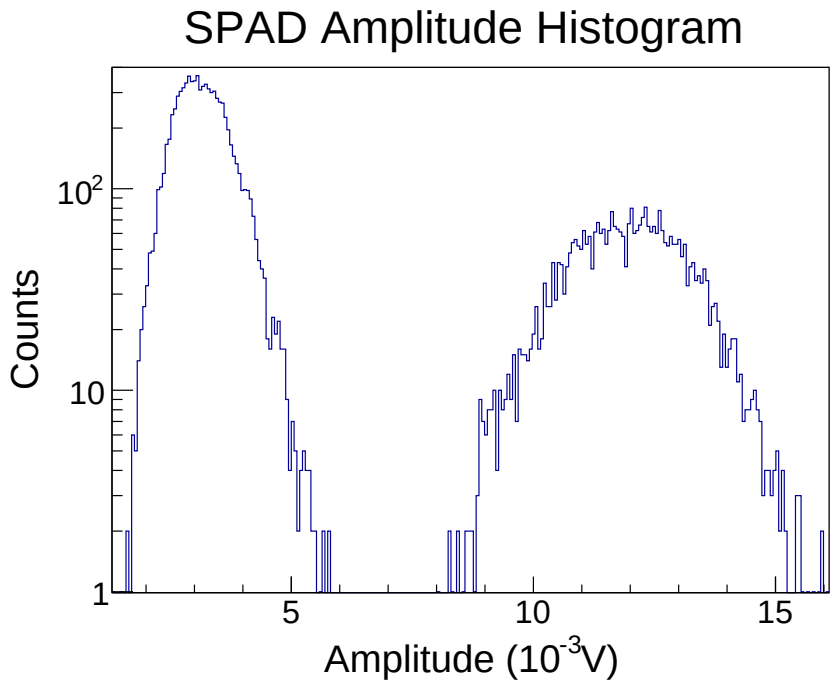

Figure 3.18: Amplitude spectrum of a SPAD, operated at a bias voltage 1 V over the breakdown voltage.

3.3 Methods and device comparison

To compare the previously written methods, four devices are chosen: two 1x1 mm^2 SiPMs with cell pitch of 25 μm and 40 μm, respectively, and two SPADs with the same layout and quenching resistors of single cells of the SiPMs. All the devices are produced in NUV–HD technology [102]. In Table 3.3, the main parameters of the SiPMs are summarised.

Table 3.3: SiPMs 1x1 mm^2 main parameters at 20 °C and 5 V overvoltage

Parameter	SiPM 1x1 mm^2 25 μm	SiPM 1x1 mm^2 40 μm
Cell pitch (μm)	25	40
Gain (x10^6)	∼1.5	∼3.5
Nominal Fill Factor (%)	73	83
Peak PDE (nm)	400 - 420	
Dark Count Rate (kHz/mm^2)	50	
Delayed noise probability (%)	<1	
Direct optical cross–talk probability (%)	<15	

In Figures 3.19, two micrographs of the SPAD with 40 μm cell pitch, with independent connection, and a portion of the SiPM with the same cell pitch are shown, using the same magnification. From the figures, it is possible observe

the equal structure of the SPAD and the single SiPM cell.

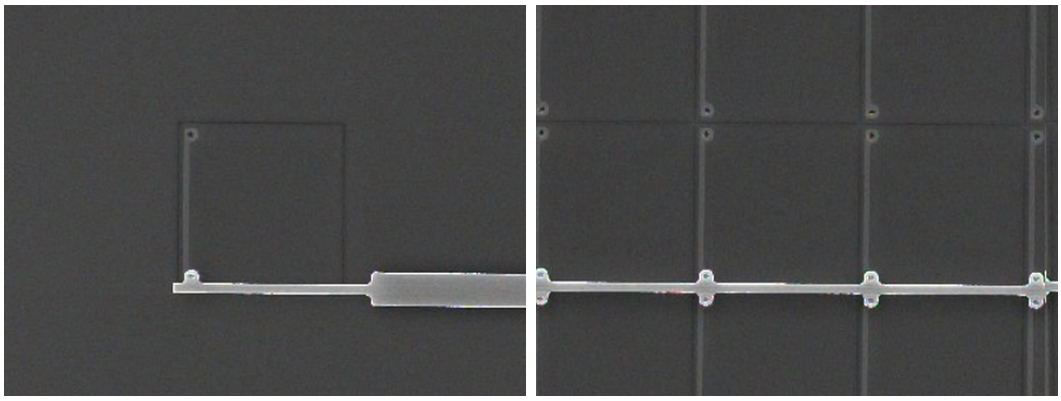

Figure 3.19: Pictures of the SPAD (left) and the SiPM with the 40 μm cell pitch (right). The pictures are taken with the same magnification and main elements of the devices (electrical contacts, quenching resistors and trenches) are visible. The equivalence in the layout between the two devices is evident.

A comparison between the methods is presented measuring the SiPMs PDE at three different wavelengths from NUV to NIR. The sources of light are the LEDs with nominal wavelength equal to 400, 545 and 700 nm. Figure 3.20 shows the PDE measurements as a function of the overvoltage. The dashed lines refer to the SiPM with 25 μm cell pitch and the continuous ones to the SiPM with 40 μm cell pitch. In every plot, the same color is used to represent a particular method (red for the CCM, green for the PM and blue for the PCM). The plots show a good agreement within the errors for both SiPMs. Typical measurement uncertainty is below 5 % for each method. The total time required for the shown measurements is different among the methods but similar for different devices and wavelengths. With the CCM, the time is in the order of two hours, mainly due to the measurement in dark condition; with the PM, the time is a few minutes and it depends only on the current measurement instrument, but the time for the noise characterisation in dark must be added because the calculation of the ECF in dark condition is necessary; with the PCM, the time is several minutes and it is dominated by the number of acquired events, triggered by the pulser. The methods can be considered comparable in terms of precision and equally reliable but different for the complexity of the set–up and also for the required time. On these basis, the CCM is preferable if only a single measurement, just after the characterisation in dark of a device, is needed because the set–up can be used without variations; the PCM can be chosen for a few wavelength measurements; for a complete PDE scan, the PM is the better choice, but in the UV and violet regions, up to 420 nm, the LEDs must be used because the not reliable light calibration of the monochromator lamp discussed in the subsection 3.2.1. In this last wavelength range, the PCM remains the best choice.

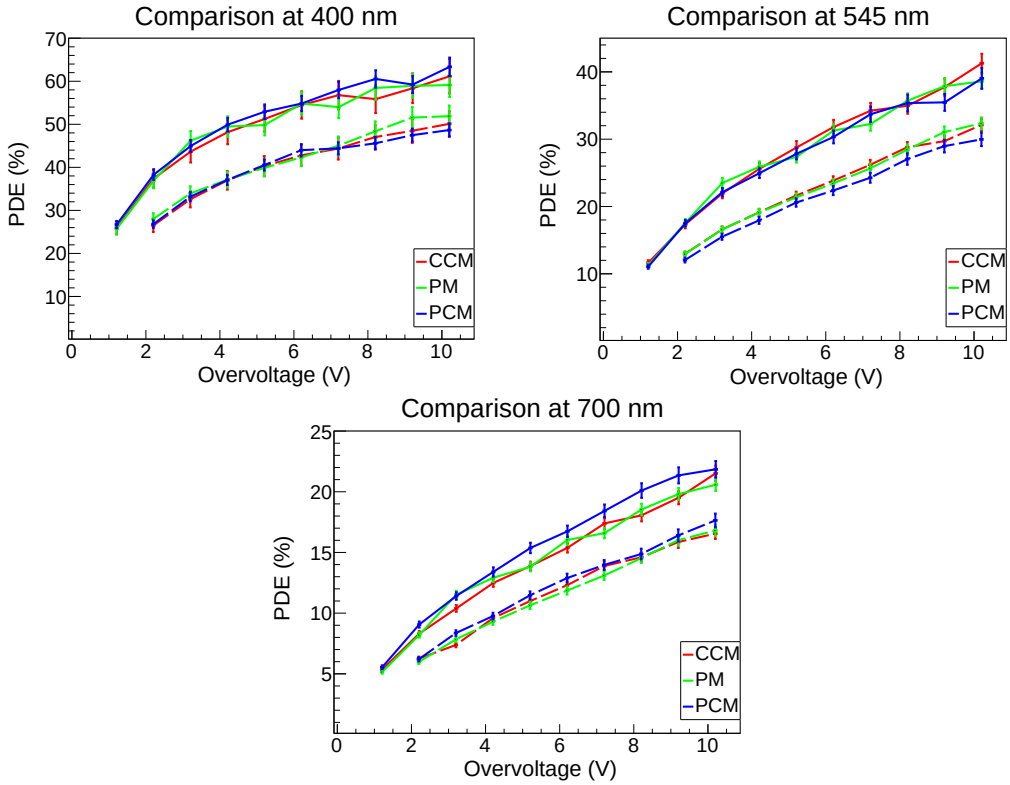

Figure 3.20: PDE measurements as a function of the overvoltage with all the methods at about 400 nm (top left), 545 nm (top right) and 700 nm (bottom) of the SiPMs 1x1 mm^2. The dashed lines refer to the SiPM with 25 μm cell pitch, the continuous ones to the SiPM with 40 μm cell pitch. Each method is represented by a different color, indicated in the plot legends.

A second, and more interesting, comparison can be shown between measurements on the SiPMs and SPADs, having the same layout of single SiPM cells. Since the equivalence of the three presented methods in terms of measurement precision and reliability was just proven, this comparison can be shown using only one method, the PCM. This method is chosen because it is the most reliable for the SPAD measurements, as discussed in the subsection 3.2.2. In Figure 3.21, the PDE measurements as a function of the overvoltage of the devices are shown. The dashed lines refer to the SiPM and to the SPAD with 25 μm cell pitch and the continuous ones to the SiPM and SPAD with 40 μm cell pitch. The red lines represent the SiPM results and the blue ones the SPAD. The average uncertainty in the SPAD measurements is about 3 %, lower with respect to the corresponding SiPMs. The plots show a good agreement between the SiPM and the SPAD for both the cell pitches and for every tested wavelength. The required time for the SPAD and SiPM measurements is also comparable, in the order of several minutes per wavelength. The found agreement is not trivial. It means that the PDE of a new technology can be

obtained measuring SPADs instead of SiPMs, reducing the measurement complexity and errors. In addition to these advantages, it is possible to apply a larger overvoltage to the SPADs because they have a very low DCR, and no cross–talk, thus, the pedestal peak is always observable, and the measurement is always feasible. Only the quenching resistor ability to stop the avalanche limits the applied overvoltage. The SPAD measurements allow to measure the PDE in extreme conditions at which no SiPM, independently from its size, can be tested any more, giving a better knowledge of the SiPM behaviour in such conditions. At such high overvoltage, it is also possible to better appreciate the different behaviour at the three tested wavelengths. The PDE at 400 nm reaches the highest value and saturates while at longer wavelengths the PDE increases almost linearly and does not show the saturation. This is an expected result because the tested devices are built on p–on–n technology.

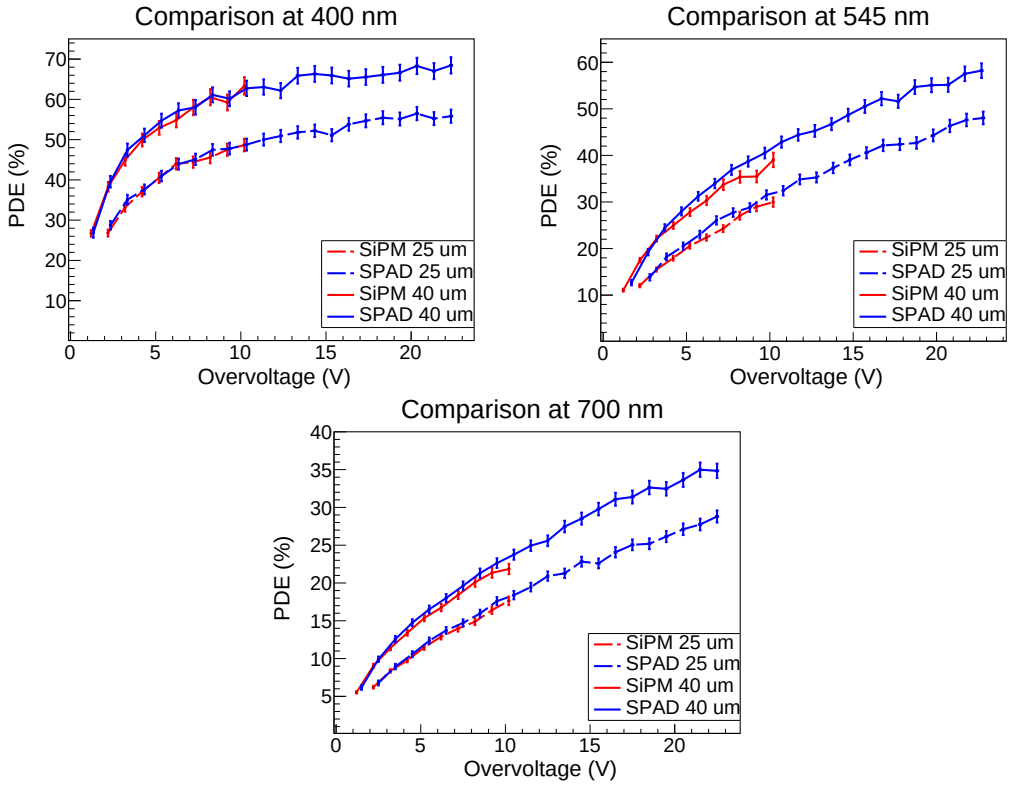

Figure 3.21: Comparison of the PDE measurements of SiPMs and SPADs at 400 nm (top left), 545 nm (top right) and 700 nm (bottom). The measurements are performed employing the PCM. The dashed lines refer to the devices with 25 μm cell pitch, the continuous line to those with 40 μm cell pitch.

The demonstrated equivalence between the PDE measured on SiPMs and SPADs will be fully exploited in the next section, in which the complete characterisation of a NUV–HD production will be shown.

Chapter 4

Experimental results

In this chapter, the characterisation of the first large cells NUV–HD SiPMs is presented. Four different SiPMs are tested with cell pitch of 25 μm, 30 μm, 35 μm and 40 μm, respectively. They have a V_{BD} of about 28 V. In the first section, the characterisation in dark, from which all the noise contributions and the electrical parameters are extracted, is presented. This characterisation is performed on 1x1 mm^2 SiPMs at 20 °C. In the subsequent section, the PDE measurements are also shown. These measurements are performed on SPADs having the same layout of the above written single SiPM cells and they are taken at room temperature (about 25 °C).

All the results reported in this section were just presented at the Vienna Conference on Instrumentation 2016 [138].

4.1 Characterisation in dark

In this section, the noise and electrical parameters of 1x1 mm^2 SiPMs, with cell pitches ranging from 25 μm to 40 μm, are reported. The results presented in this section were obtained following the characterisation in dark reported in the section 3.1 [70]. To verify if the SiPM parameters are affected by possible statistical fluctuations, it was chosen to measure four different silicon dies, everyone including all the four 1x1 mm^2 SiPMs, taken from two wafers of the same NUV–HD production, named W1 and W2 in this section. The four dies are indicated as W1 #1 and W2 #1, W2 #2 and W2 #3.

The gain of the devices is expected to be directly proportional to the overvoltage, according to the equation (1.5), through the cell capacitance. In Figure 4.1, the measured gain of the SiPMs are reported. In every plot, the measurement results of three devices among the above written are compared. For every cell pitch, the results are in agreement within the errors, showing that the statistical fluctuations among different devices, if present, are smaller, and thus negligible, than the measurement errors. The measured gain does not perfectly increase linearly as expected. The less than linear trend implies that

the cell capacitance decreases with the overvoltage. Assuming that the cell can be approximated to a flat capacitor, the observed behaviour means that the dielectric material increases its dimension with the overvoltage. In the cell, this can be explained assuming that the depleted region increases its size with the overvoltage, at least till it reaches the epitaxial layer–substrate interface.

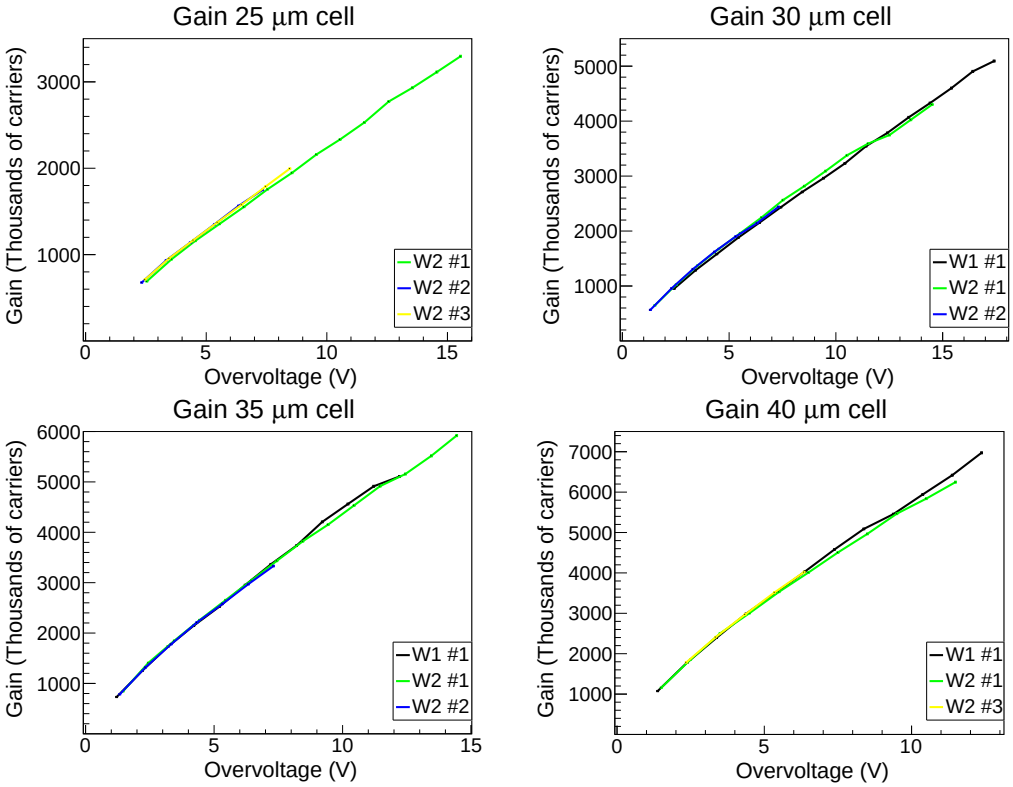

Figure 4.1: Measured gain of the NUV–HD 1x1 mm^2 SiPMs with cell pitch equal to 25 μm (top left), 30 μm (top right), 35 μm (bottom left) and 40 μm (bottom right) as a function of the overvoltage. In every plot, results on three different devices can be observed. The results are in agreement in every plot.

The SiPMs belonging to the silicon die W2 #1 are used to compare the gain among the different cell pitches. The comparison is shown in Figure 4.2. As expected, the gain increases with the cell pitch. In particular, under the assumption that the cell can be approximated to a flat capacitor, the capacitance must be directly proportional to the cell area, equal to the surface of the flat capacitor. Since the depletion region increases in the devices independently from the cell pitch (because it depends only on the electric field profile that is equal in every device), the same proportionality is expected between the gain and the cell area too. For this reason, the ratio between the measured gain of the cells must be equal to the ratio between the cell areas at every overvoltage. These ratios are shown in Figure 4.3. Every continuous line represents the ratio between the measured gain of the SiPM having cell pitch shown in the

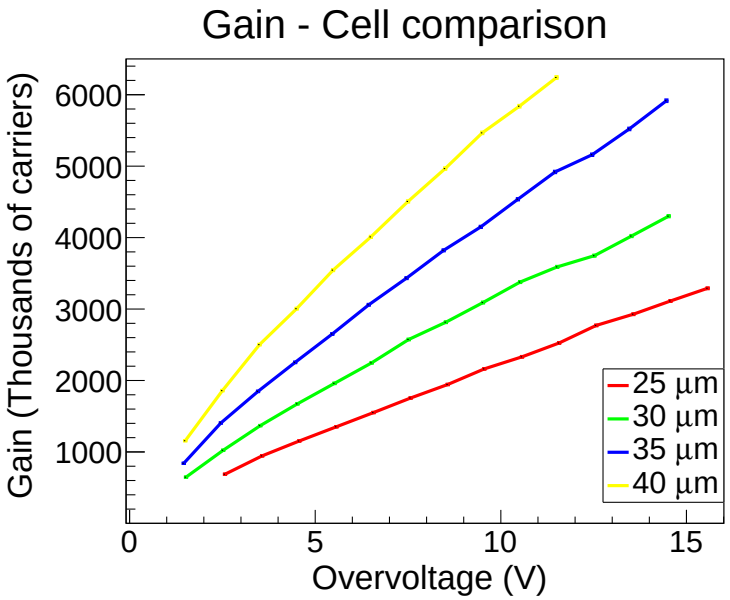

Figure 4.2: Comparison between the measured gain of the NUV–HD 1x1 mm^2 SiPMs. The devices belong to the same silicon die, the W2 #1. The gain increases with the cell pitch due to the increasing cell capacitance with the cell pitch.

legend and the one with 40 μm cell pitch. The dashed lines are the measured ratios between the cell areas. The agreement between the two ratios is very good, always within the measurement errors, for all the cell pitches.

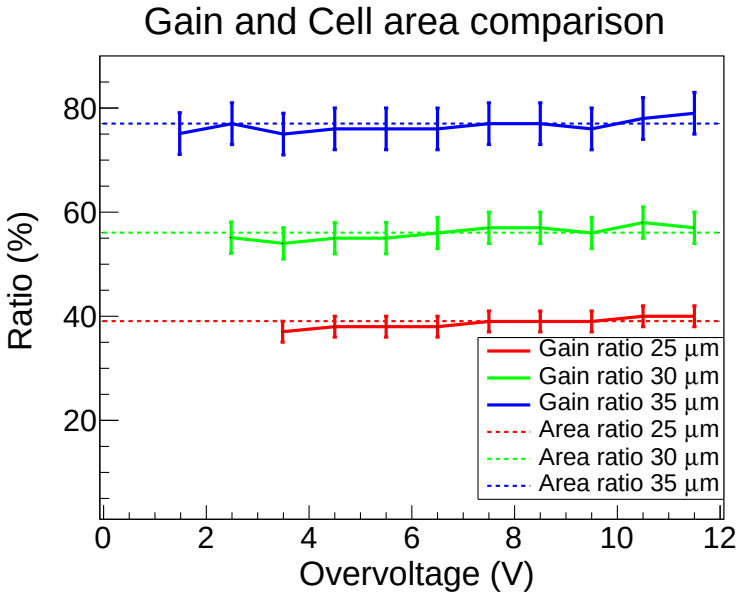

Figure 4.3: Comparison between the measured gain ratios, continuous lines, and the cell area ratios, dashed lines, of the NUV–HD 1x1 mm^2 SiPMs, as a function of the overvoltage. The ratios are in agreement within the errors.

From the cell gain, it is possible to extract the effective cell capacitance, as the tangent of the gain curve in every point. The comparison between the measured cell capacitances of the four SiPMs is shown in Figure 4.4. The decreasing behaviour is evident, as the approximately constant value at large overvoltage, because the depleted region reaches the epitaxial layer–substrate interface and stops its enlargement.

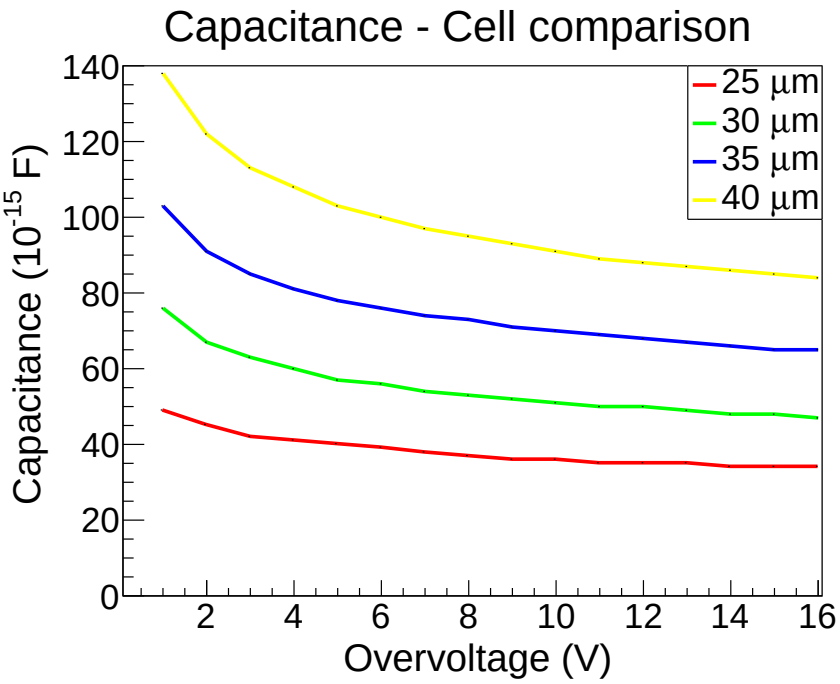

Figure 4.4: Comparison between the measured effective cell capacitance, as a function of the overvoltage, of the NUV–HD 1x1 mm^2 SiPMs belonging to the W2 #1. The capacitance increases with the cell pitch and decreases with the overvoltage. At large overvoltage it becomes approximately constant.

In Figure 4.5, the measured direct cross–talk probability of the SiPMs are reported. The results are in agreement within the measurement errors for all the cell pitches. Also in this case, as for the gain measurement, this agreement shows that the DiCT probability does not suffer from the statistical fluctuations among the devices, or, at least, they are negligible. The SiPMs belonging to the same silicon die (W2 #1) are used to compare the DiCT probability among the different cell pitches. The comparison is shown in Figure 4.6. As expected, the DiCT probability increases with the cell pitch. This is mainly due to the larger cell gain. The comparison of the DiCT probability at the same gain is very different, as shown in Figure 4.7. Actually, at the same gain, every SiPM cell emits the same number of secondary photons, on average, independently from its size. But, the smaller cells reach the same gain at a larger overvoltage, thus they also have a larger triggering probability. For this reason, the smaller cells have a larger DiCT probability at the same gain.

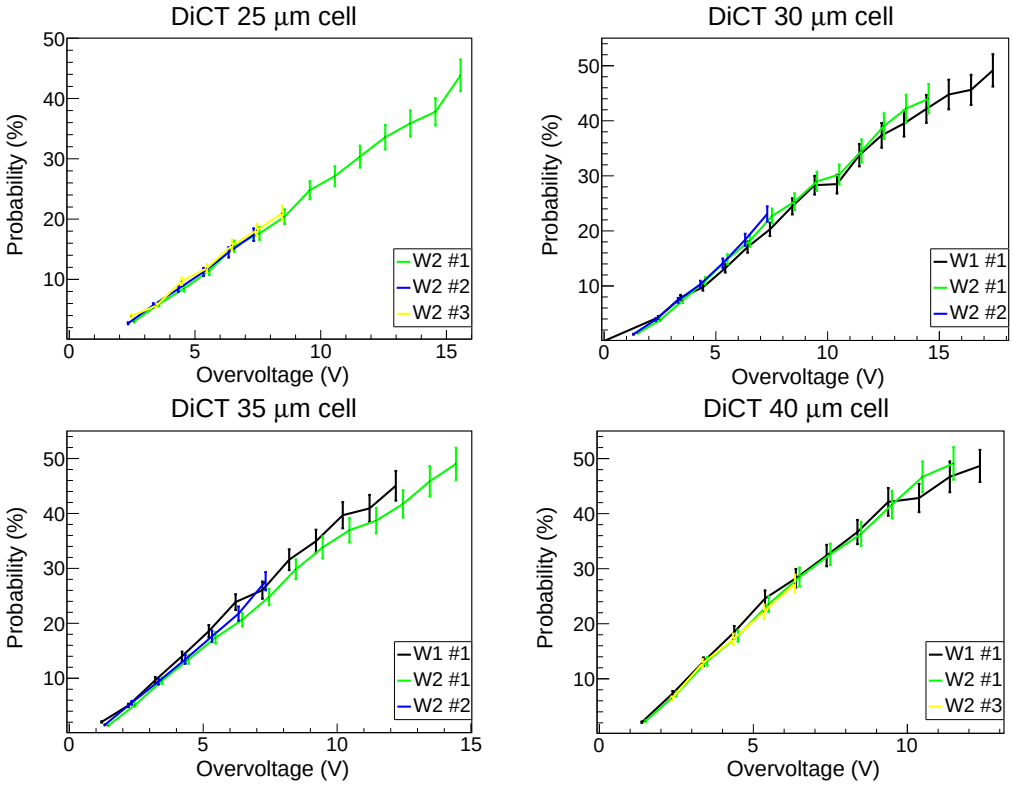

Figure 4.5: Measured DiCT probabilities of the NUV–HD 1x1 mm^2 SiPMs with cell pitch equal to 25 μm (top left), 30 μm (top right), 35 μm (bottom left) and 40 μm (bottom right) as a function of the overvoltage. In every plot, three different devices results can be observed. The agreement between the devices with the same cell pitch is good.

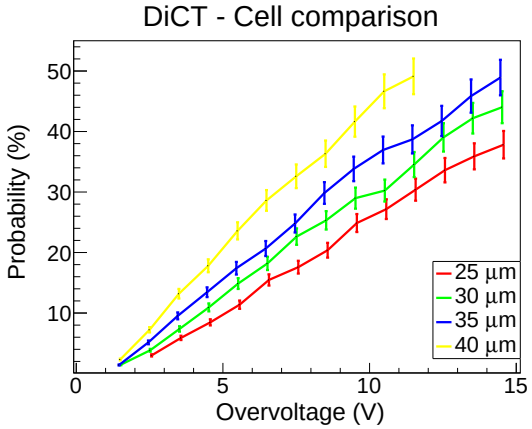

Figure 4.6: Comparison between the measured DiCT probabilities of the NUV–HD 1x1 mm^2 SiPMs. The devices belong to the same silicon die, indicated as W2 #1 in the previous plots. The DiCT probability increases with the cell pitch due to the increasing gain.

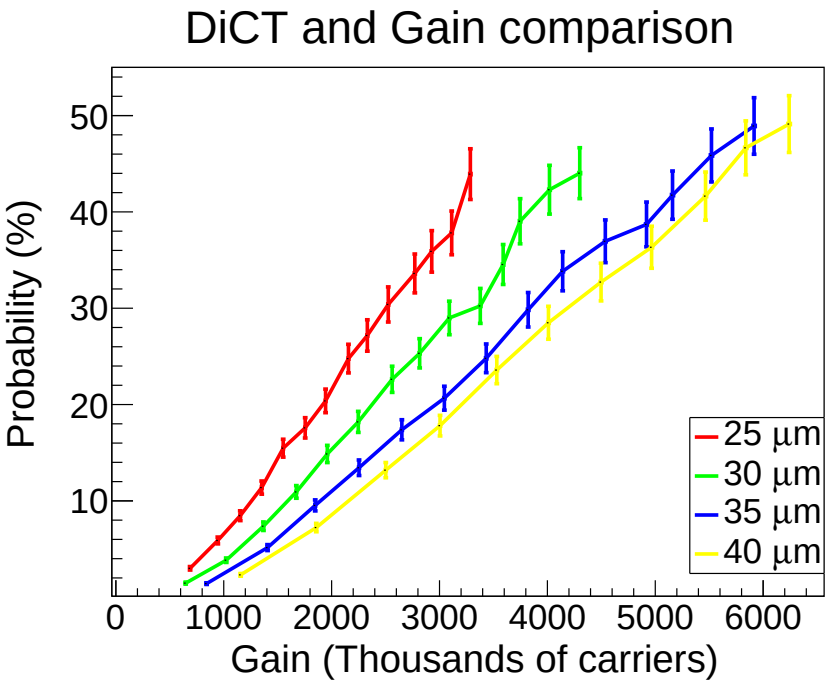

Figure 4.7: Comparison between the measured DiCT probabilities of the NUV–HD 1x1 mm^2 SiPMs as a function of their gain. The DiCT probability increases reducing the cell pitch because the smaller cell devices must be operated at a higher overvoltage to have the same gain and have a larger triggering probability.

In Figure 4.8, the sum of the delayed noise probabilities (delayed cross–talk and afterpulsing) of the SiPMs are reported. These noises are considered together because it is not possible to completely separate the afterpulsing events with very small time delay with respect to the primary events from the delayed cross–talk ones. The results seem in agreement within the measurement errors for all the cell pitches. The measurement errors are very large compared to the obtained values, thus the comparison is not conclusive. The SiPMs belonging to the same silicon die (W2 #1) are used to compare the delayed noise probabilities among the different cell pitches. The comparison is shown in Figure 4.9.
The delayed noise probabilities are very small because the NUV–HD are built on the same substrate of the NUV–Low–AP.

In Figure 4.10, the measured DCRs, as a function of the overvoltage, for SiPMs belonging to the same silicon die, are shown. The measured DCR is different between the various cells at every tested overvoltage. The differences can not be attributed to the measurement errors. In Figure 4.11, the measured IV plots, in dark condition, of the 1x1 mm^2 SiPMs of the wafer W2, are shown. The dashed lines represent the IV of the device in the die W2 #1. In every plot, a broad measurement range can be observed. The minimum measured current is smaller than the maximum one by a factor between two and three.

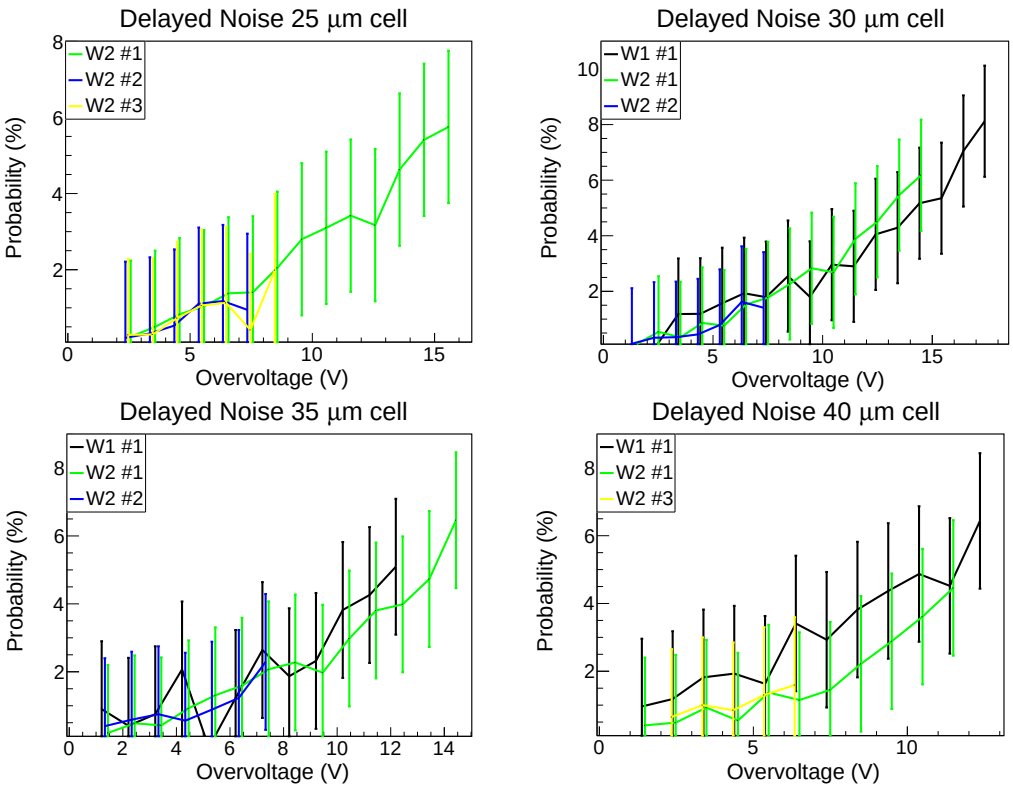

Figure 4.8: Measured delayed noise probabilities of the NUV–HD 1x1 mm^2 SiPMs with cell pitch equal to 25 μm (top left), 30 μm (top right), 35 μm (bottom left) and 40 μm (bottom right) as a function of the overvoltage. In every plot, three different devices results can be observed. The measurement errors are too large to evidence any possible systematic difference.

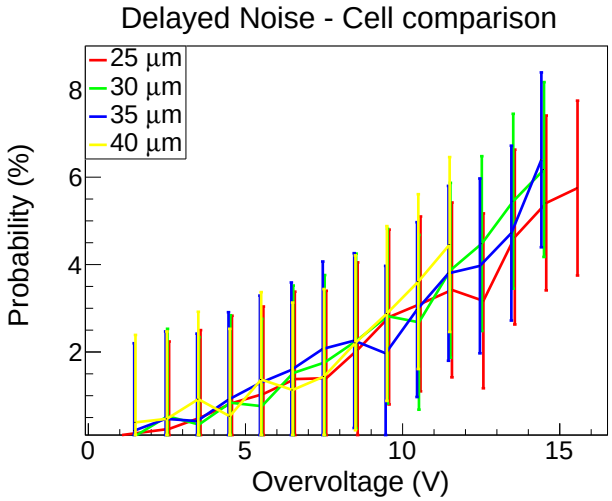

Figure 4.9: Comparison between the measured delayed noise probabilities of the NUV–HD 1x1 mm^2 SiPMs. The devices belong to the same silicon die, the W2 #1.

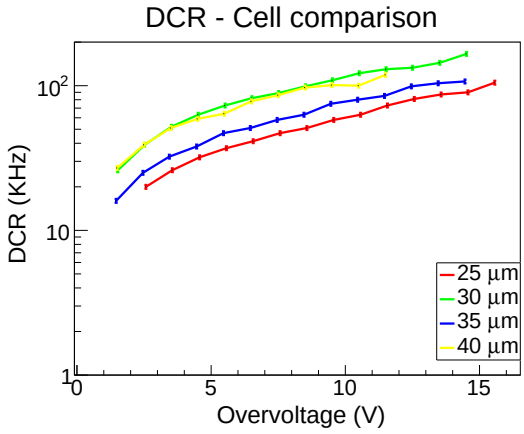

Figure 4.10: Comparison between the measured DCR of the NUV–HD 1x1 mm^2 SiPMs as a function of the overvoltage. Every color represents a different cell pitch, as reported in the plot legend. The SiPMs belong to the same silicon die, W2 #1. No trend is observable.

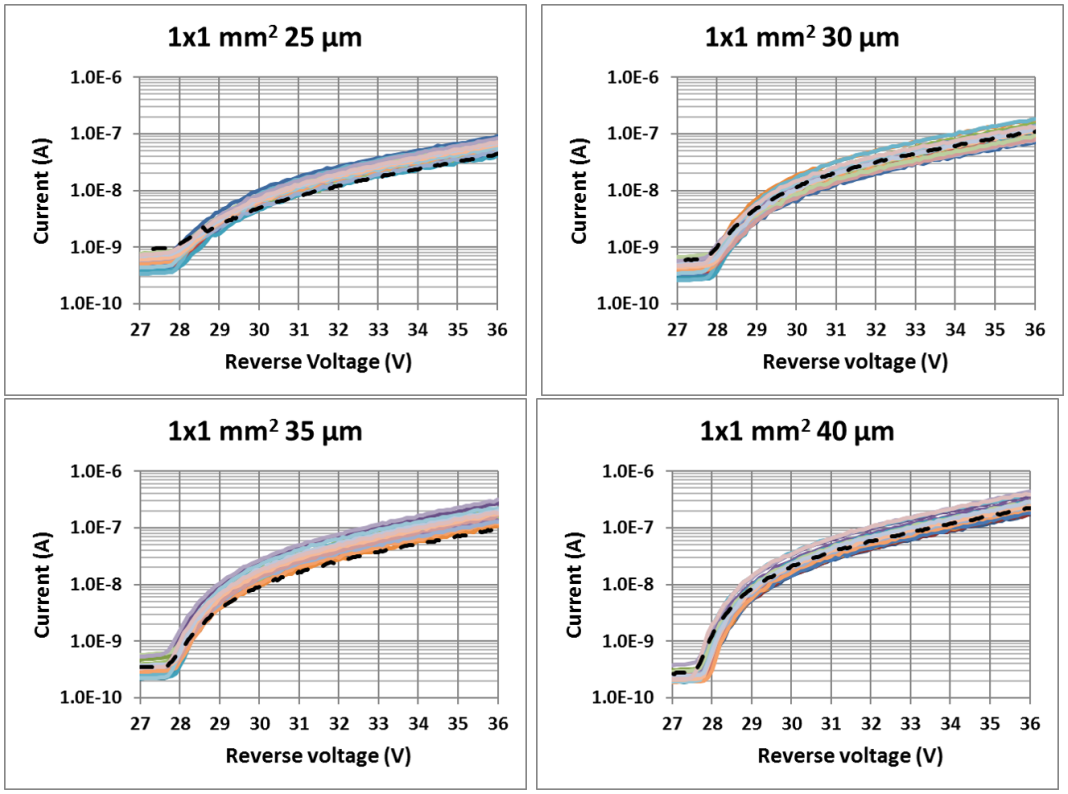

Figure 4.11: Measured IV plot of the NUV–HD 1x1 mm^2 SiPMs with cell pitch equal to 25 μm (top left), 30 μm (top right), 35 μm (bottom left) and 40 μm (bottom right) as a function of the bias voltage (only the part at larger voltages than V_{BD} are shown). The dashed lines represent the IV measurements of the device in the die W2 #1.

Remembering that the electrical current of a SiPM, at bias voltage larger than the breakdown one, can be expressed as:

$$I_{SiPM} = I_{LEAK} + G_{SiPM} \times q_e \times DCR \times ECF \tag{4.1}$$

in which every term is defined as in the previous chapters, the broad range must be attributed to the variation of one or more SiPM parameters among the same devices on the wafer. Since the surface leakage current is order of magnitudes lower than the multiplied current, the gain and the DiCT probability were found equal among different devices and the delayed noise components are almost absent in the Low–AP technology, the observed variation in the IV plot can be attributed only to an equal variation of the DCR on the wafer. This variation is much larger than the DCR measurement error, thus this becomes negligible to define the technology DCR and its uncertainty. Observing the Figure 4.11, the IV of the devices W2 #1 with cell pitches equal to 25 μm and 35 μm are near the minimum of the current spread, while the other two devices have an IV near the middle of the range. For this reason, it is possible to affirm that the DCR measured on the 25 μm and 35 μm cell pitch devices are the minimum DCR of the technology and the result of the 30 μm and 40 μm is the average DCR of the technology.

4.2 PDE Measurements

In this section, the PDE measurements of the NUV–HD technology is reported. The results presented in this section are obtained employing SPADs with size equal to 25 μm, 30 μm, 35 μm and 40 μm. The result presented here can be considered valid also for the corresponding SiPMs because the equivalence between the devices was just shown in the section 3.3.

A device with cell size equal to 30 μm is used to measure the PDE spectrum of the technology. The result is shown in Figure 4.12. The measurement is performed with the pulsed counting method, just described in the section 3.2.2, employing the LEDs with nominal wavelength from 300 nm to 700 nm reported in Table 3.1. As expected for a p–on–n technology, the PDE spectrum is peaked at small wavelengths. In particular, this technology has its maximum in the region between 380 nm and 420 nm, and it exceeds the 50 % at large overvoltages.
From Figure 4.12 an important aspect can be derived regarding the technology triggering probability. At large overvoltage, the measured PDE increasing rate decreases due to the triggering probability saturation. At short wavelengths, the observed decrease happens at smaller overvoltage, thus the triggering probability saturates faster in this range, as expected from a p–on–n device.

To verify that the PDE does not vary among the same devices on the wafer,

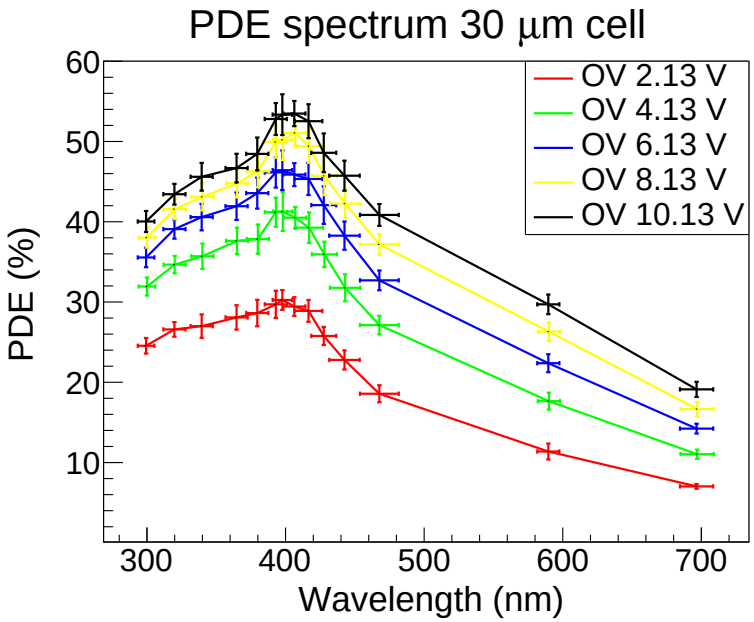

Figure 4.12: Measured PDE spectrum of the NUV–HD SPAD with cell pitch equal to 30 μm as a function of the wavelength, at different overvoltages (reported in the plot legend). The measurement is performed with the pulsed counting method and employing the LEDs from deep NUV up to all the visible spectrum. The peak PDE is in the NUV–violet region as expected.

it was chosen to compare three different silicon dies, everyone including all the four SPADs, taken from two wafers of the same NUV–HD production, named W1 and W2, as before. The three dies are indicated as W1 #2 and W2 #4 and W2 #5.

The comparison is performed illuminating the devices with the LED with 400 nm nominal wavelength. The results are shown in Figure 4.13. In every plot, the measurement results are in agreement within the errors, showing that the statistical fluctuations among different devices, if present, are smaller, and thus negligible, than the measurement errors. The SPADs belonging to the silicon die W2 #4 are used to compare the PDE among the different cell pitches as a function of the overvoltage. The comparison, performed at the same wavelength, is shown in Figure 4.14. As expected the PDE increases with the cell pitch, due to the larger FF of the larger cells.

The measured PDE at 400 nm of the 30 μm cell size SPAD can be fitted by the equation (1.17) to obtain the technology saturation rate at small wavelengths. A saturation rate of a bit more than 4 V is found, thus the PDE reaches the 90 % of its maximum at about 10 V of overvoltage. The same fit can be performed at long wavelengths, e.g. 700 nm, finding a larger saturation rate, equal to about 15 V. This difference between the saturation rate is very important in all the applications in which a very high PDE is desired

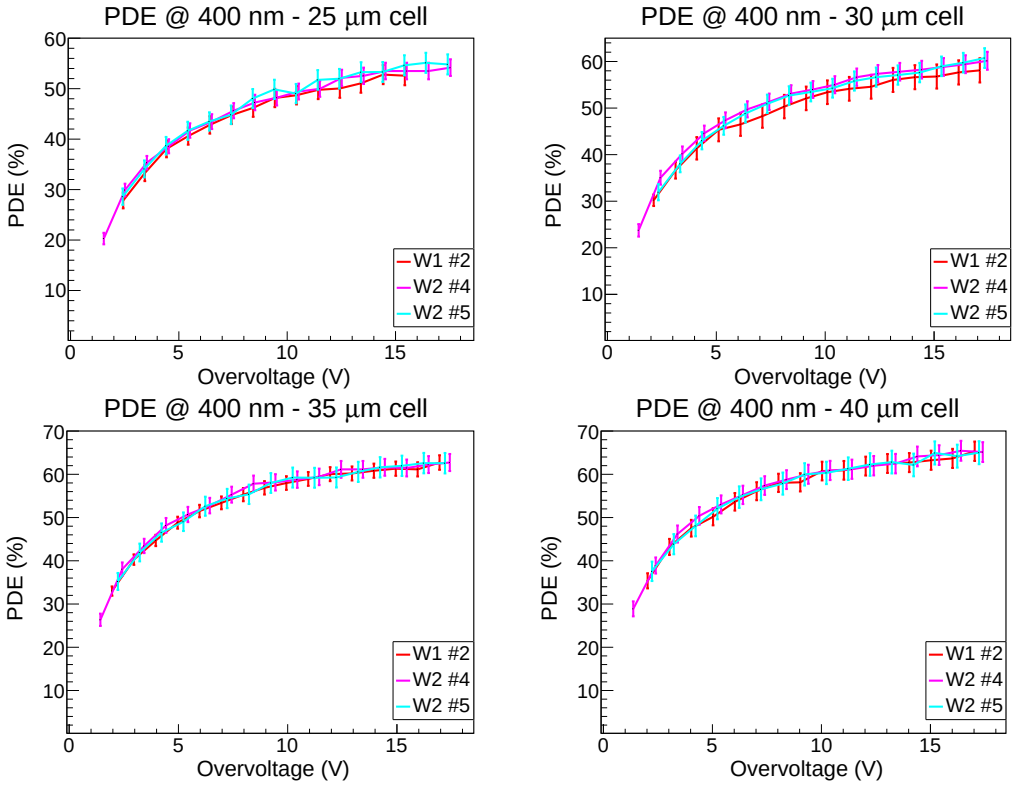

Figure 4.13: Measured PDE of the NUV–HD SPADs with cell size equal to 25 μm (top left), 30 μm (top right), 35 μm (bottom left) and 40 μm (bottom right) as a function of the overvoltage, illuminating the devices with the LED with 400 nm nominal wavelength. In every plot, results on three different devices can be observed. The result are in agreement in every plot.

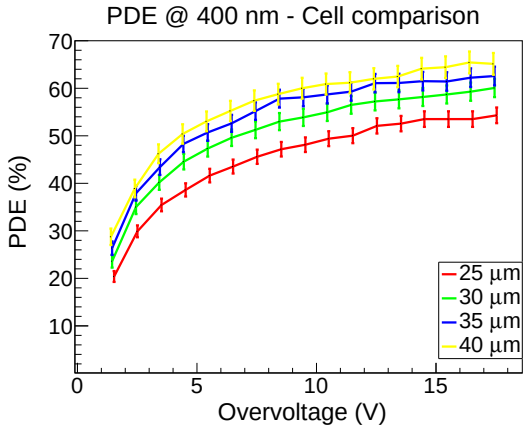

Figure 4.14: Comparison between the measured PDE of the NUV–HD SPADs at about 400 nm as a function of the overvoltage. The devices belong to the same silicon die, the W2 #4. The PDE increases with the cell size due to the increasing FF.

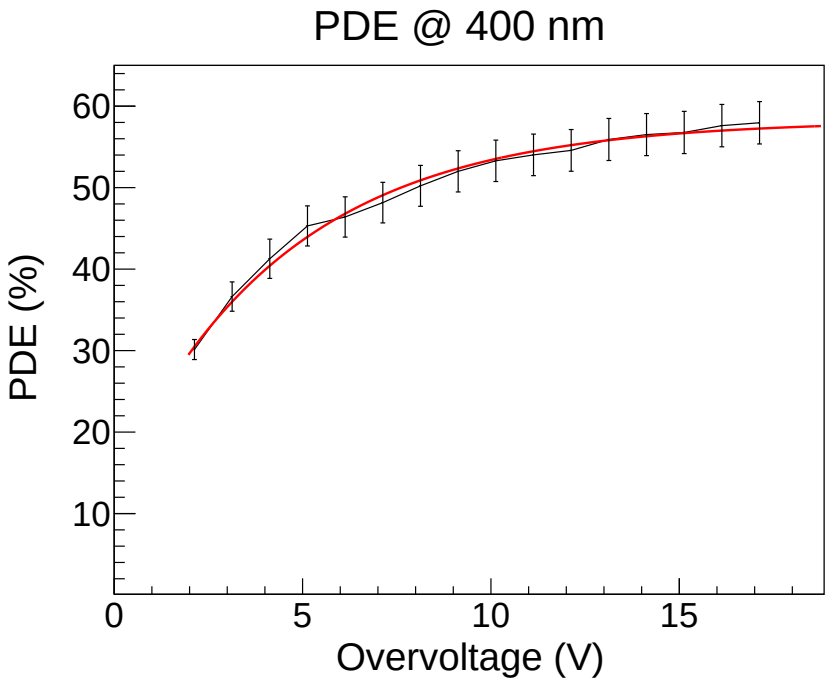

Figure 4.15: Measured PDE of the NUV–HD SPAD with 30 μm cell size at about 400 nm (black line) and relative fit function (red line).

only at short wavelengths, as the CTA experiment. Since the night sky background consists mainly of long wavelength photons, while the useful signal, the Cherenkov radiation, is peaked at small wavelengths, this large difference between the saturation rates allows to operate the device at a relatively large overvoltage having a very high PDE in the useful region, and, at the same time, a small detection of the background radiation. The ratio between the measured PDEs becomes a signal–to–noise ratio. The measured PDE at 400 nm as a function of the measured one at 700 nm is shown in Figure 4.16. Until the PDE at 400 nm increases more than the one at 700 nm, it can be convenient to increase the overvoltage. The maximum overvoltage can be derived from the following equation (4.2).

$$\frac{d(PDE_{400})}{dV} > \frac{d(PDE_{700})}{dV} \Longrightarrow OV < \frac{V_{700}V_{400}}{V_{700}-V_{400}} ln(\frac{QE_{400}V_{700}}{QE_{700}V_{400}}) \qquad (4.2)$$

In the case presented here, in which QE_{400} and QE_{700} are about 80 % and 50 % and V_{400} and V_{700}, the saturation rates, are written before, the maximum overvoltage is about 11 V.

At last, the ratio between any two measured PDE shown in Figure 4.14, $R_{\frac{A}{B}}$, must be equal to the fill factor ratio, due to the identity of the quantum efficiency and the triggering probability between the devices, at the same wavelength, as shown by the equation (4.3).

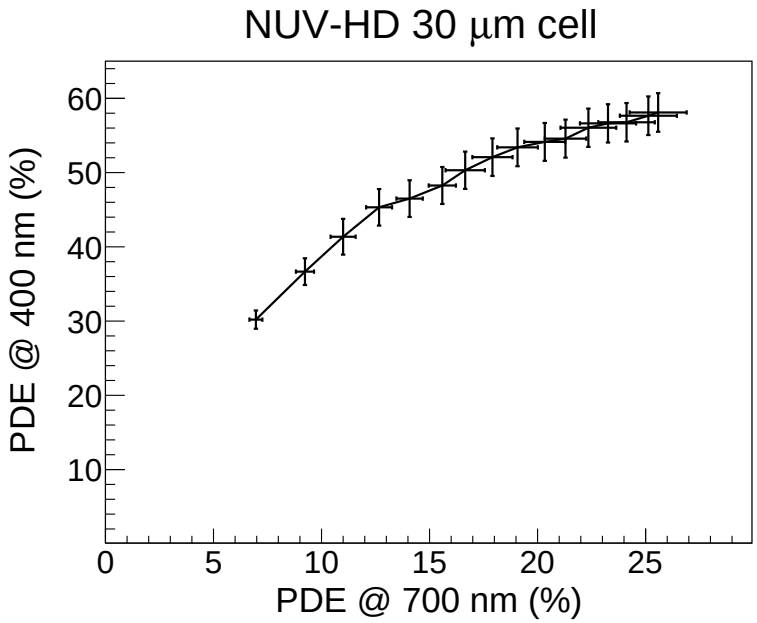

Figure 4.16: PDE at 400 nm as a function of the one at 700 nm for the NUV–HD SPAD with 30 μm cell size.

$$R_{\frac{A}{B}} = \frac{PDE_A}{PDE_B} = \frac{FF_A \times QE \times T_P}{FF_B \times QE \times T_P} = \frac{FF_A}{FF_B} \tag{4.3}$$

in which the subscripts A and B represent two different devices and the other terms are defined as in the previous chapters. Since the FF is known by the cell layout, a theoretical $R_{\frac{A}{B}}$ can be defined for every couple of devices. These last ratios, between the smaller cells and the 40 μm one, are reported in Figure 4.17. For the SPADs having cell sizes equal to 30 μm and 35 μm the expected ratio is confirmed, at least within the measurement errors. However, the smallest SPAD, with 25 μm cell size, has a different behaviour. In particular, it can be seen that the ratio is not constant but it increases with the overvoltage, up to 12–13 V of overvoltage. Its value is always lower than the expected one, even considering the measurement errors. This is in contrast with the idea that the cell FF is equal to the layout one. A possible explanation can be given considering a variable inefficient area, around the active area of the cell, that artificially reduces the effective FF.

The study of the cell FF will be extensively shown in the last chapter of this work. In the next section, a final comparison among the cell pitches is shown.

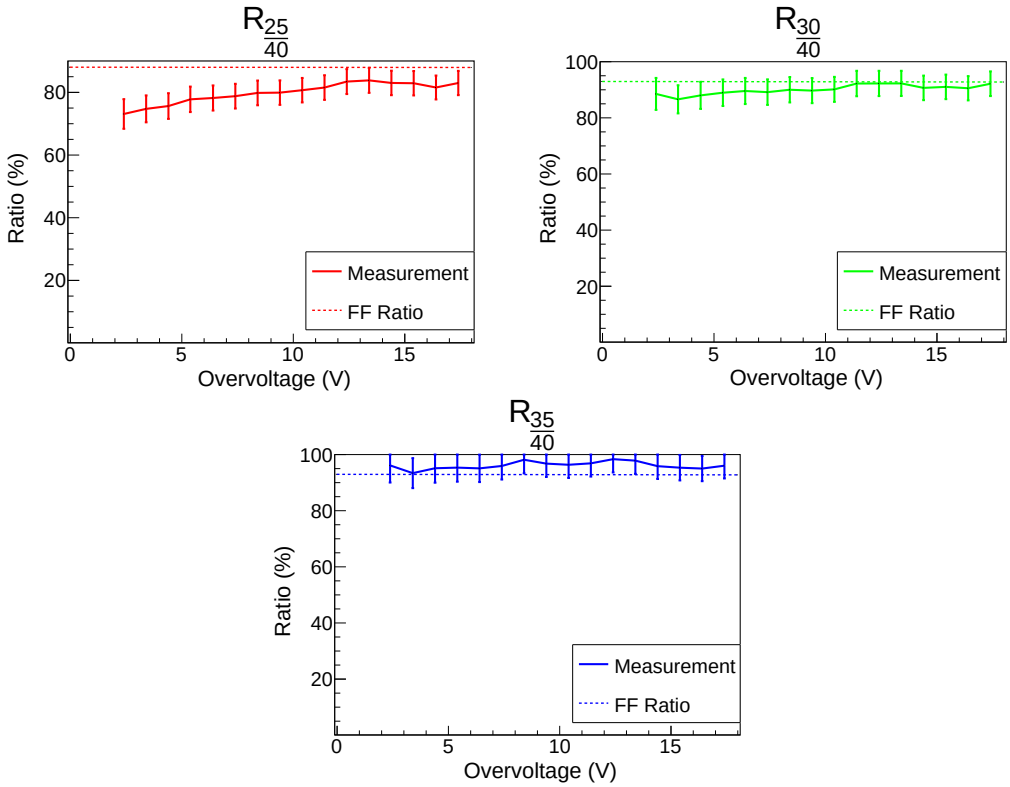

Figure 4.17: Comparison between $R_{\frac{a}{b}}$ (continuous lines) and the FF ratio (dashed lines) of the corresponding devices ($R_{\frac{25}{40}}$ on top left, $R_{\frac{25}{40}}$ on top right and $R_{\frac{35}{40}}$ on bottom). In the $R_{\frac{25}{40}}$ plot, the ratios are not in agreement leading to the hypothesis that the effective FF is smaller than the one defined by the layout.

4.3 Performance of the NUV-HD

In the previous sections, the main features of the NUV–HD were presented as a function of the overvoltage. The comparison among the different cell pitches is not definitive because all the parameters are found increasing with the cell pitch, except the DCR and the delayed noise probability, that are equal among the different devices. It is not possible to conclude what cell is the best because the larger ones have a higher PDE and a higher correlated noise probability. A more conclusive comparison among the devices can be shown if the parameters are expressed as a function of the PDE at 400 nm, the peak in the PDE spectrum. All the data used in this section to perform the comparison are measured on the 1x1 mm^2 SiPMs of the die W2 #1 and the SPADs of the die W2 #4.

In Figure 4.18, the gain as a function of the PDE is shown for all the cell pitches. If the gain is an important requirement in a application, all the cells can give comparable results, without losing PDE. The difference between the cell pitches, observed in Figure 4.2, is almost absent in this comparison. Only

the largest cell, the 40 μm one, has a slightly larger gain at PDE smaller than 50 %. For PDE values larger than this limit, all the cells have the same gain, within the measurement errors. The observed equality among the cells has origin in the different applied overvoltage to have the same PDE. The smaller cells, due to their FF, reaches the same PDE of the larger ones at a larger overvoltage, thus, their gain is also larger and comparable.

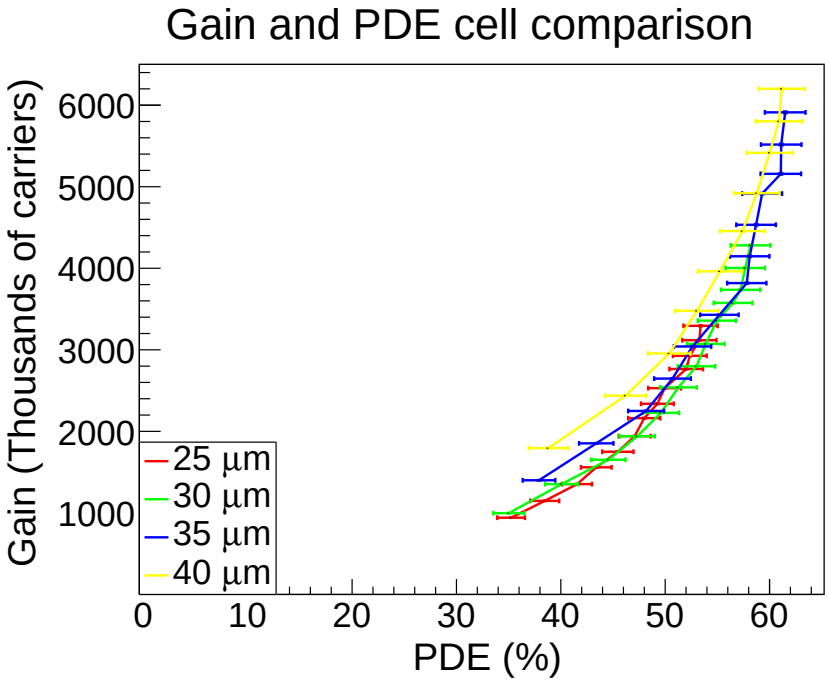

Figure 4.18: Gain of the NUV–HD devices as a function of the PDE at 400 nm for all the cell pitches. The devices are comparable.

In Figure 4.19, the DiCT probability as a function of the PDE is shown for all the cell pitches. There is a device, the smallest cell one, with a larger DiCT probability at every PDE, thus this device is worse than the others. It has, at least, a 50 % higher DiCT probability than the other cells at every PDE value. The agreement between the largest cells, in particular the 35 μm and the 40 μm, is very good at every PDE.

In Figure 4.20, the sum of the delayed noise probabilities as a function of the PDE is shown for all the cell pitches. Since the delayed noise probability is small for every PDE value and the measurement errors are relatively large, the devices can be considered equivalent.

In Figure 4.10, a strange DCR behaviour among the devices of the die W2 #1 was observed and explained. In particular, the very different measured DCR was added to the statistical fluctuations among the same SiPMs on the wafer. In Figure 4.21, in which the DCR as a function of the PDE is shown for all the cell pitches of the die W2 #1, a similar behaviour is observable.

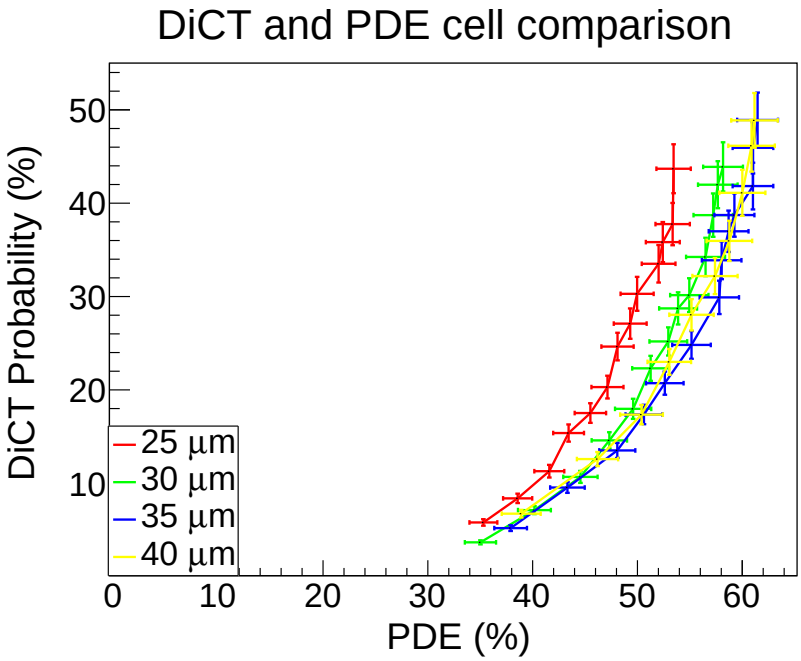

Figure 4.19: DiCT probability of the NUV–HD devices as a function of the PDE at 400 nm for all the cell pitches. The smallest cell device has a higher DiCT probability at any PDE.

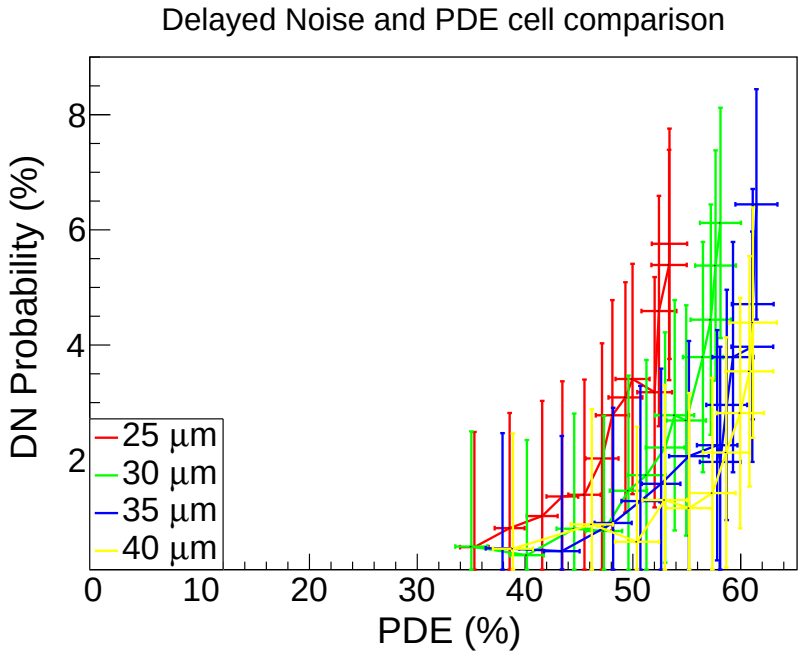

Figure 4.20: Delayed noise probability of the NUV–HD devices as a function of the PDE at 400 nm for all the cell pitches. The large measurement errors do not allow to conclude what device is the best.

The errors on the DCR are not drawn because it was just said that they are negligible with respect to the expected fluctuations.

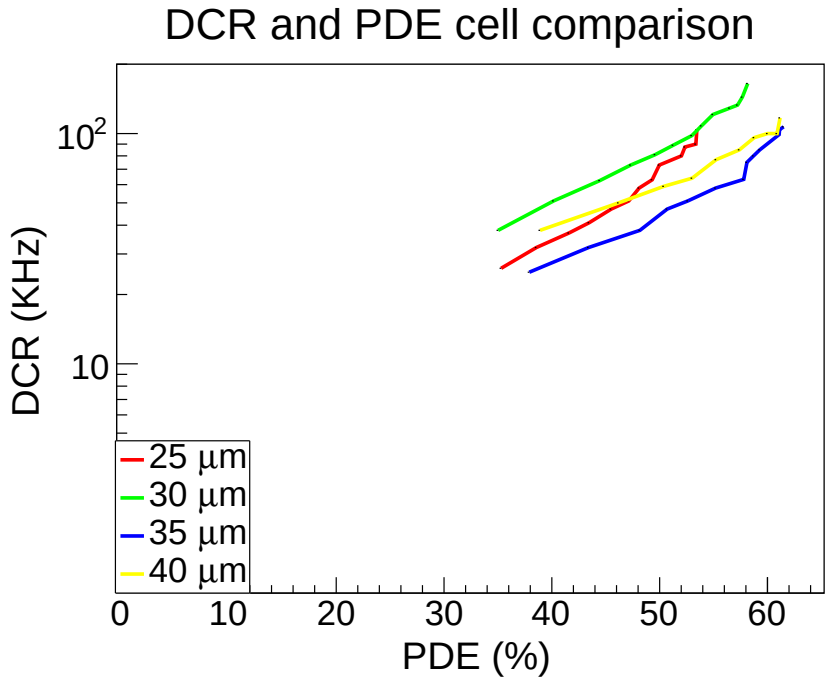

Figure 4.21: DCR of the NUV–HD devices (SiPMs in the die W2 #1) as a function of the PDE at 400 nm for all the cell pitches. The DCR errors are not drawn because negligible.

Since this comparison is not conclusive, due to the discussed fluctuations, a technology DCR is defined and compared. The technology DCR is defined as a DCR band ranging between the minimum measured DCR on a cell type and this value multiplied by the maximum ratio measured in the IV plots of the same devices. A new plot, showing the technology DCR, is presented in Figure 4.22. The technology DCR is lower increasing the cell size, even if the difference reduces with the cell size. At the same PDE, the 25 μm devices have, on average, a DCR larger by a factor about two than the 40 μm devices; the 30 μm devices have a DCR larger by a $\sim$50 %; the 35 μm devices have a DCR larger by a $\sim$30 %.

From the previously shown comparisons, it seems that the 25 μm cell device is worse than all the others. This device has a larger noise, both primary and correlated, at every PDE value. The other devices are very similar with comparable performance at the same PDE. The only parameter, in which a small difference is observable among the largest cells, is the primary noise. Considering the DCR, the largest cell is better, on average, than the others, but due to the statistical fluctuations on the wafer, it is not easy to exploit this difference in big experiments, in which a large number of SiPMs is required.

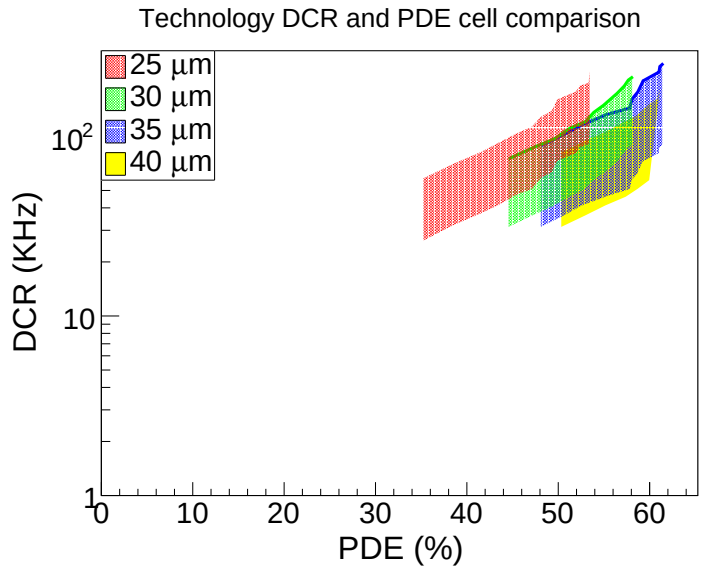

Figure 4.22: Technology DCR of the NUV–HD devices as a function of the PDE at 400 nm for all the cell pitches.

The NUV–HD technology is well suited for all the applications exposed in the sections 2.3 and 2.3.1. In particular, for the CTA experiment the PDE spectrum of the NUV–HD devices seems very good to detect the Cherenkov photons. In Figure 4.23, the two spectra, the PDE of the 30 μm device at about 10 V of overvoltage and the Cherenkov one in atmosphere, are shown.

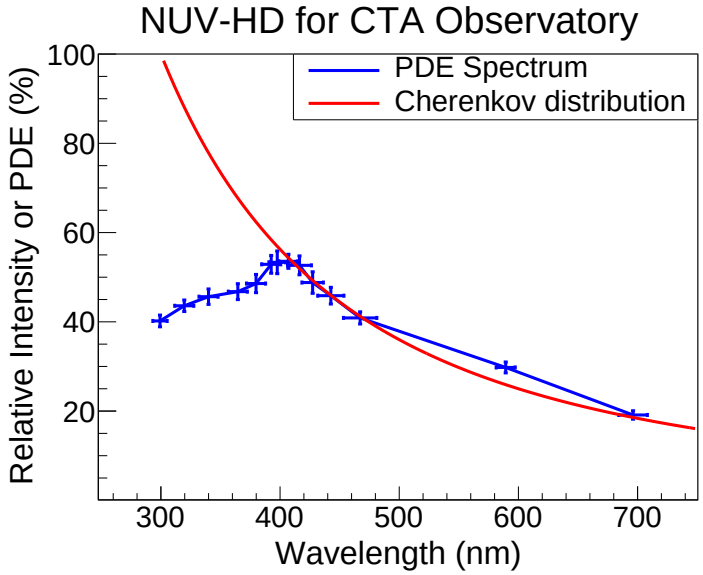

Figure 4.23: Comparison between the NUV–HD technology PDE spectrum and the Cherenkov spectrum in Earth atmosphere. The NUV–HD well matches the Cherenkov spectrum.

Multiplying the NUV–HD PDE for the Cherenkov spectrum and integrating up to the visible range allows to calculate the expected number of detected Cherenkov photons. For the shown 30 μm device, the result is a bit less than 40 %. The 40 μm cell device is expected to exceed this value.

Figure 4.24 is a plot taken from [130] reporting the characteristics of a device from Hamamatsu (50 μm cell pitch and 3x3 mm^2 size), that is considered a reference among SiPM manufacturers. The device primary noise and cross–talk, as a function of the PDE at 450 nm and 550 nm, are reported. The wavelength 450 nm was chosen because it is the peak PDE in the Hamamatsu technology.

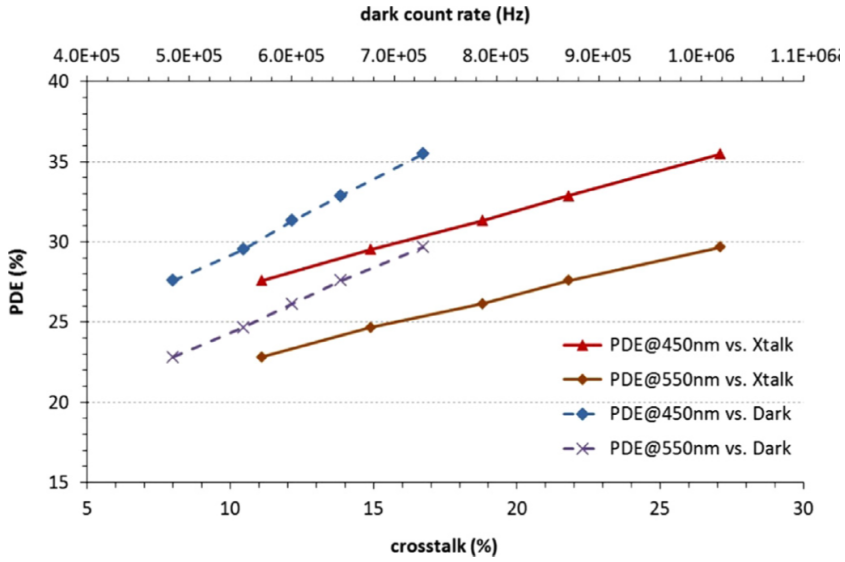

Figure 4.24: Primary noise and cross–talk as a function of the PDE at 450 nm and 550 nm of a Hamamatsu MPPC with 50 μm cell pitch and 3x3 mm^2 size. The plot is taken from [130].

The comparison of both primary and correlated noise of NUV–HD SiPMs (Figures 4.19, 4.20 and 4.22) and Hamamatsu MPPCs (Figure 4.24, after normalization of the DCR to the unit area), allows to conclude that the NUV-HD technology has a lower total noise at any PDE value. This comparison, even if not conclusive (Hamamatsu data are taken from [130], not directly measured), is an indication that the NUV–HD technology can be considered, at least, as a good choice as the Hamamatsu device for the CTA observatory.

Chapter 5

Effective Fill Factor

A new production of NUV–HD devices is extensively studied to get more informations about the factors contributing to the technology PDE. Through these studies it is possible to confirm the expected quantum efficiency of the technology, better understand the triggering probability at extreme conditions and, at last, give an answer to the question emerged from the results reported in Figure 4.17 concerning the observed differences between nominal and experimental values of the fill factor.
Every detail about these studies are just published in [139].

5.1 Effective Fill Factor

In the first chapter it was said that the fill factor is usually considered a constant in the equation (1.14). It can be determined by the cell layout, identifying the active area as the cell region in which the dopant enrichment is realised to create the high–field region. However, this is only an approximation. The electric field is not constant across all the designed active area. There is a transition region, approaching the active area border, in which it decreases from the constant maximum value to zero. Since the triggering probability is proportional to the electric field strength, through the ionisation coefficients α_e and α_h, the triggering probability is not constant inside the designed active area too. For this reason, an effective fill factor, FF_{eff}, always smaller than the one defined by the layout, should be used in equation (1.14). A simple box model, describing the electric field profile in the active area, is proposed to define the FF_{eff}. In this model, the electric field is maximum and constant in a central region of the cell, smaller than the designed active area, and zero outside. Increasing the overvoltage, the maximum electric field region extends to the nominal active area borders. The constant electric field region is defined as the effective active area. In Figure 5.1, the real electric field profile and the box model are represented along with a cell layout. The different inefficient regions, the transition and the ineffective by the layout, are indicated by ar-

rows.

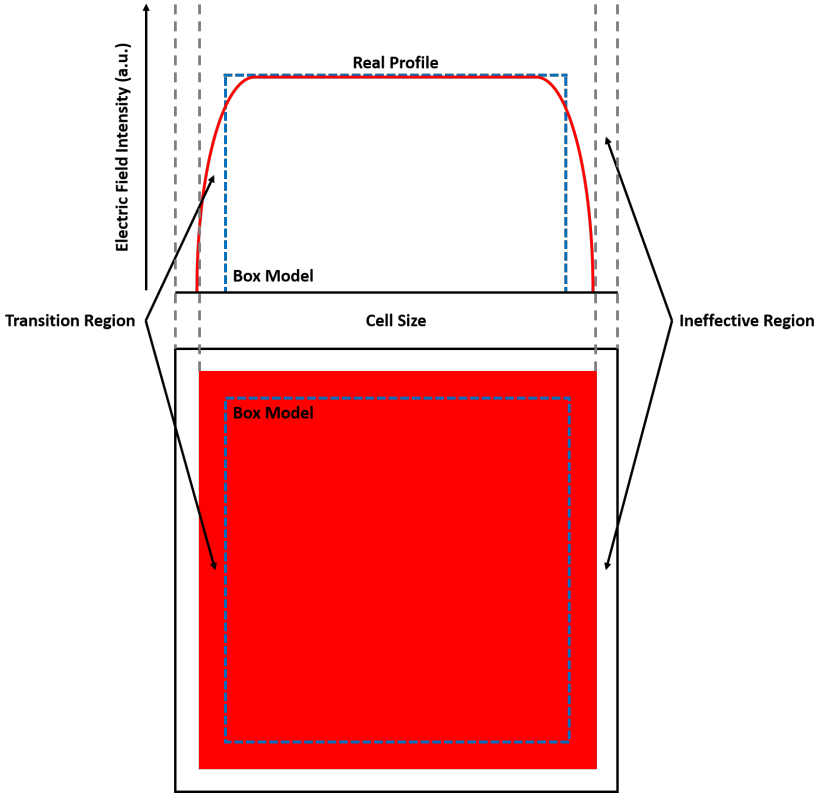

Figure 5.1: The box model is drawn. The blue dashed line represents the electric field profile in the model, while the red curve is the shape of the real one. The difference between the effective active area, inside the square blue dashed line, and the nominal one, the red square, is evident. The inefficient regions are also indicated by arrows.

In the box model, the inefficient border regions are larger than those defined by the layout because the transition regions must be summed up to them. Since this further term decreases its size with the overvoltage, the $\mathrm{FF_{eff}}$ approaches the nominal value increasing the overvoltage. In the box model, the active area is always considered perfectly square, no importance is given to the electrical contacts on the top of the cell.
The equation (1.14) must be rewritten as:

$$PDE(V,\lambda) = FF_{eff}(V) \times QE(\lambda) \times T_P(V,\lambda) \tag{5.1}$$

considering the more correct contribution of the $\mathrm{FF_{eff}}$.

5.2 Device features

Three different NUV–HD devices are tested: a circular SPAD with 10 μm radius active area and 100 % FF (the active area is defined by a metal ring shielding the cell border [64]); a square SPAD with 35 μm cell size, with the same layout of a single SiPM cell with equal cell pitch, and a nominal FF equal to about 81 %; a square photodiode with active area of 1 mm^2 and same dopant profiles of the SPADs, operated at very low bias voltage, far from the breakdown voltage, to avoid multiplication. All the devices have a V_{BD} of about 26 V. The square SPAD is used in these measurements, instead of a SiPM, because it allows to apply a larger overvoltage, due to the lower correlated and primary noises. This is required for a better FF_{eff} and transition region size estimation.
According to the results reported in section 4.2, the difference between the measured FF and the theoretical one is observable only in the 25 μm device, then the maximum expected transition region size is about three micrometres. The circular SPAD has a covered active area, by design, larger than this value, thus its exposed active area is expected to be always defined only be the metal ring. For this reason, it is correct to assume the circular SPAD FF equal to 100 %. In Figure 5.2, a micrograph of the circular SPAD is shown. The metal ring is indicated by an arrow.

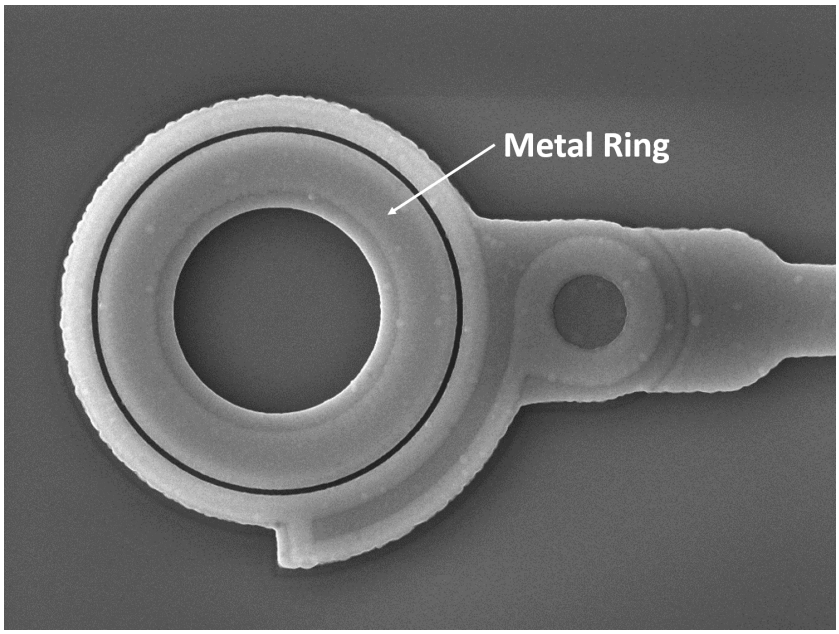

Figure 5.2: A micrograph of the circular SPAD with 10 μm radius is shown. The arrow indicates the metal ring defining the active area.

5.3 Quantum Efficiency measurement

The set–up, presented in the section 3.2.1 and shown in Figure 3.9, is employed to measure the quantum efficiency of the NUV–HD technology substituting the amplifier board with a holder and measuring the photodiode current with a picoammeter.
The photodiode has no internal gain, for this reason it is important to operate it at a low bias voltage to reduce the dark current and increase the signal–to–noise ratio when illuminated with light. The used photodiode has a minimum dark current at 0.100÷0.200 V, thus it is reverse biased at 0.150 V during the measurements. Illuminating the device with a known light source, the following equation (5.2) allows to obtain the QE(λ):

$$QE(\lambda) = \frac{I_{PD-L} - I_{PD-D}}{q_e(I_{REF-L} - I_{REF-D})L_{Cal}(\lambda)} \tag{5.2}$$

in which $I_{PD\text{-}L}$ and $I_{PD\text{-}D}$ are the photodiode currents read in light and in dark, respectively, and the other quantities are defined as in the previous chapters. $L_{Cal}(\lambda)$ allows to convert the reference photodiode electrical current in the photon rate on the device position. It is known for all the LEDs used in the measurements from the calibration procedure described in the section 3.2.1.

In Figure 5.3, the measurement result is compared with the simulated ARC transmission.

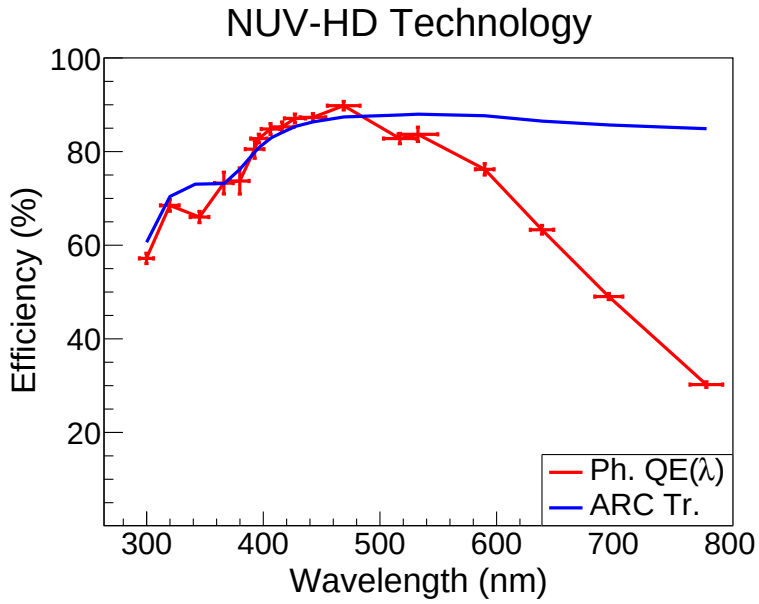

Figure 5.3: A comparison between the direct QE measurement on a NUV–HD photodiode and the simulated ARC transmission is shown. The agreement is very good from NUV region up to the blue. At longer wavelengths, the small active volume size limits the QE.

Since in the NUV–HD technology, the junction is very close to the surface, the carrier collection for short wavelength photons is very high. In this region, an average value of 95 % carrier collection is measured. In blue region, the carrier collection is almost 100 % due to the less important surface loss. At longer wavelengths the absorption depth in silicon is so large that a non negligible fraction of the carriers are photogenerated in the substrate and recombine before the collection. For this reason, the measured QE(λ) reduces compared to the ARC transmission in this region. Since the separation between the simulated ARC and the direct QE results happens between the measurement with the LEDs having central wavelength equal to 468 nm and 519 nm, the active volume size must range between $\sim$1.5 μm and $\sim$4 μm (considering a total absorption within 5 absorption depth) in agreement with the expected epitaxial layer depth.

5.4 Triggering Probability measurement

The circular SPAD is used to measure the triggering probability, $T_P(V, \lambda)$. Since this device has an effective FF equal to 100 %, the equation (5.1) can be simplified in the PDP equation [140, 141]:

$$PDP(V, \lambda) = QE(\lambda) \times T_P(V, \lambda) \tag{5.3}$$

Combining the equation (1.17) and this last one, a fit function for the PDP of the circular SPAD can be written as:

$$PDP(V, \lambda) = [p0](1 - e^{-\frac{OV}{[p1]}}) \tag{5.4}$$

in which [p0] represents the QE(λ) and [p1] the V_λ.

In Figure 5.4, an example of these measurements, illuminating the device with the LED with nominal wavelength equal to 525 nm, is shown. The fit function seems to describe very well the data. In Figure 5.5, the same measurement is repeated applying a larger applied overvoltage to the device. The fit function does not correctly fit the data this time. The fit parameters are very different and incompatible with those obtained in the previous fit, showing the inconsistency of the used fit function. The fit function (5.4) was experimentally derived and assured only at small relative overvoltage (overvoltage with respect to the breakdown voltage) [47]. It was never used in measurements in which the relative overvoltage exceeded the 30 %, to the author knowledge. In the case presented here, the relative overvoltage is about 125 %. The observed disagreement is a clue that the used fit function is only an approximation valid for small relative overvoltage. Since the QE term is a constant in the equation (5.4), the inconsistency of the fit function reveals that the triggering

probability function (1.17) is incorrect.

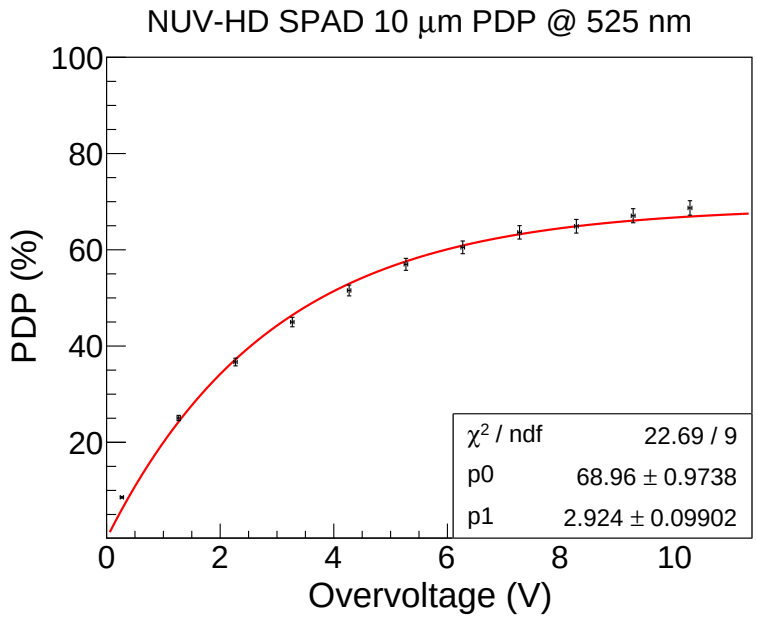

Figure 5.4: An example of the PDP measurement on the SPAD with 10 μm radius at about 525 nm up to 10 V of overvoltage. The fit function (5.4) is superimposed to the data. The fit values are reported inside the plot with their errors.

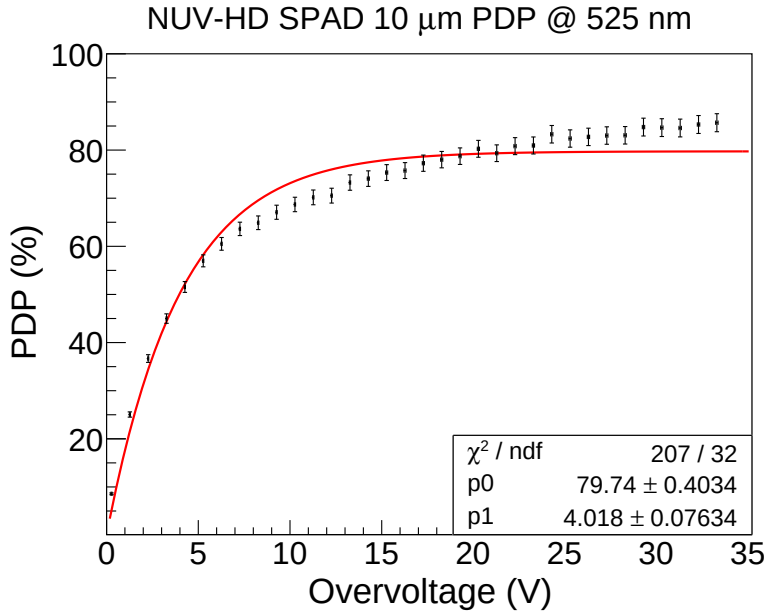

Figure 5.5: PDP measurement of the SPAD with 10 μm radius at about 525 nm up to ~33 V of overvoltage. The fit function (5.4) is superimposed to the data showing its inefficiency.

A new function, better describing the triggering probability, also at large overvoltage, is represented by the equation (5.5):

$$T_P(V,\lambda) = 1 - e^{-\frac{OV}{\alpha+\beta\sqrt{OV}}} = 1 - e^{-\frac{OV}{V_\lambda(V)}} \tag{5.5}$$

in which α and β are two parameters, defined positive, determined by the fit procedure. The equations (1.17) and (5.5) are formally identical, but in this last one, the saturation rate V_λ is voltage dependent, assuring a better agreement with the experimental data, also at large relative overvoltage. Using this function in the equation (5.4), and, assuming the saturation of the triggering probability at the quantum efficiency value, as before, the new PDP fit function is:

$$PDP(V,\lambda) = [p0](1 - e^{-\frac{OV}{[p1]+[p2]\sqrt{OV}}}) \tag{5.6}$$

in which [p0] is defined as before and [p1] and [p2] are α and β, respectively.

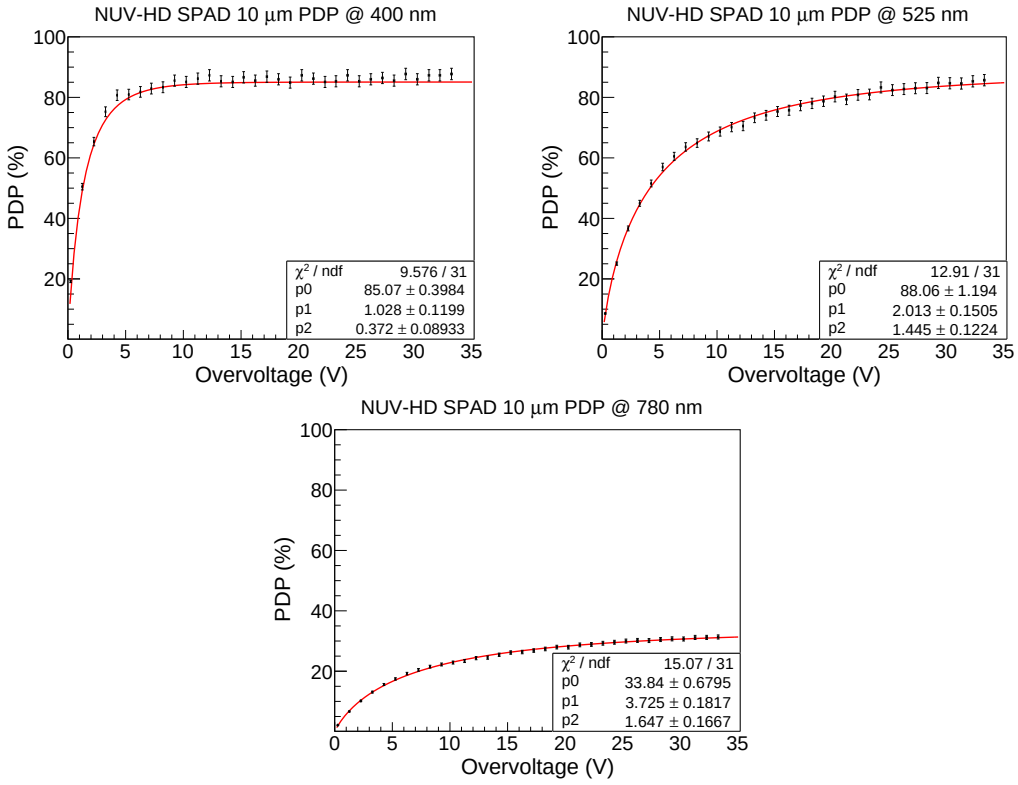

Figure 5.6: PDP measurement of the SPAD with 10 μm radius at about 400 nm (top left), 525 nm (top right) and 780 nm (bottom) up to ~33 V of overvoltage. The fit function (5.6) is superimposed to the data and the fit values reported inside the plot.

Measurement examples of the circular SPAD at three different wavelengths are shown in Figure 5.6. The new fit function gives better results with respect to first one, at least up to the measured overvoltage.

The new fit function allows to compare the QE(λ) directly measured on the photodiode and the one obtained as fit parameter with the circular SPAD. In Figure 5.7, the comparison between the two measurements is shown. The errors on the wavelengths are omitted because they are not important for this comparison and the omission allows to clarify the plot. The agreement between the direct and indirect QE(λ) is good in all the measured spectrum.

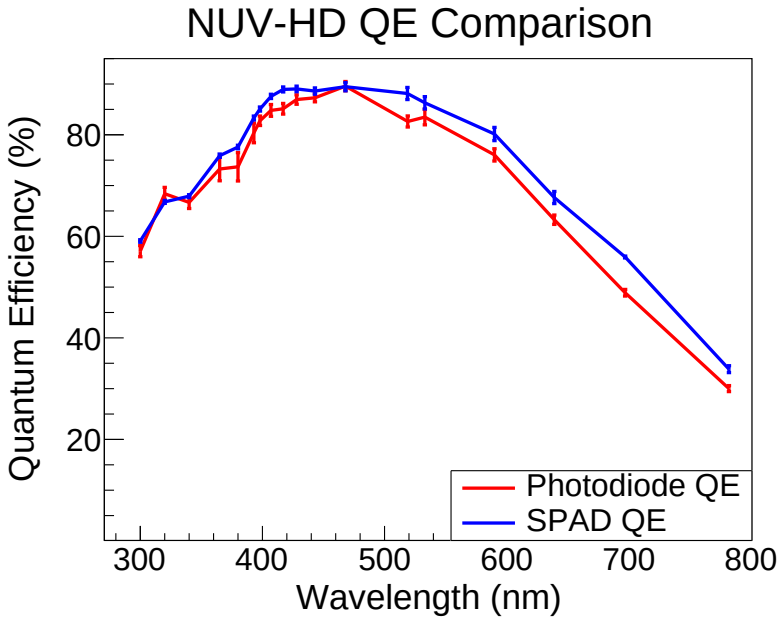

Figure 5.7: A comparison between the QE directly measured with the photodiode and indirectly obtained from the fit procedure of the circular SPAD with 10 μm radius.

At last, it is possible to plot the saturation rate V_λ(V), as a function of the wavelength. The plot is reported in Figure 5.8. The saturation rate plot can be ideally divided into three regions: I)short wavelengths; II)middle wavelengths; III)long wavelengths. In the region I, the photons have a very small absorption depth in silicon, thus they are absorbed close to the surface and the carriers are photogenerated before entering the high–field region. In this region, the events are exclusively triggered by the electrons in the NUV–HD devices, for this reason the electrons are called primary carriers. As a result, all of these photons give an almost constant V_λ value. In the region II, the photon absorption depth rapidly increases, thus the photons are absorbed more and more in depth in the SPAD. The contribution of the slower saturating secondary carriers, the holes, to the triggering probability increases. For this reason, V_λ increases. In the last region, the photon absorption depth is very large com-

pared to the device active volume depth, thus the absorption of photons is almost uniform in the total depth of the device and V_λ is almost constant and wavelength–independent because the event fractions triggered by the primary and secondary carriers are about 1/3 and 2/3 of the total events, respectively.

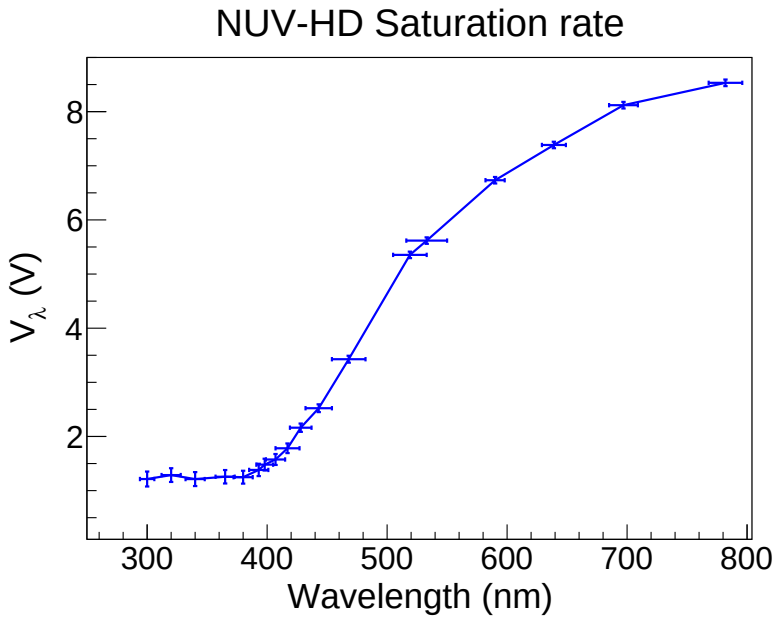

Figure 5.8: The saturation rate obtained from the fit procedure of the circular SPAD with 10 μm radius as a function of the wavelength. In the short–wavelength range it is constant because only the electrons trigger the events. At longer wavelength, V_λ increases due to the event fraction triggered by the slower saturating holes.

It is interesting to note that this measurement gives an indirect estimation of the junction depth, because V_λ starts changing when the photons are absorbed in the region in which both the carriers give a contribution to the total triggering probability, i.e. when they enter the high–field region (almost corresponding to the junction). In the case presented here, the V_λ starts changing around the wavelength 393 nm. The photons are absorbed inside ∼300 nm from the surface at this wavelength, thus this can be considered an upper limit to the junction depth estimation, in agreement with direct measurement of the dopant profiles.

5.5 Effective FF measurement

In this section, a method to calculate the square SPAD FF_{eff} is proposed. The FF_{eff} can be obtained as the ratio between the PDE of the square SPAD, PDE_S, and the PDP of the circular one because the QE(λ) and TP(V;λ) are

equal in both devices:

$$FF_{Eff}(V) = \frac{PDE_S}{PDP} = \frac{FF_{Eff}(V)QE(\lambda)T_P(V,\lambda)}{QE(\lambda)T_P(V,\lambda)} \tag{5.7}$$

In Figure 5.9, the measured PDE and PDP of the devices, illuminated with the LED with nominal wavelength equal to 525 nm, are shown. The PDP is multiplied by the nominal FF of the square SPAD, 81 %. The scaled PDP is larger than the measured PDE showing the importance of the FF_{Eff} to correctly know the device PDE.

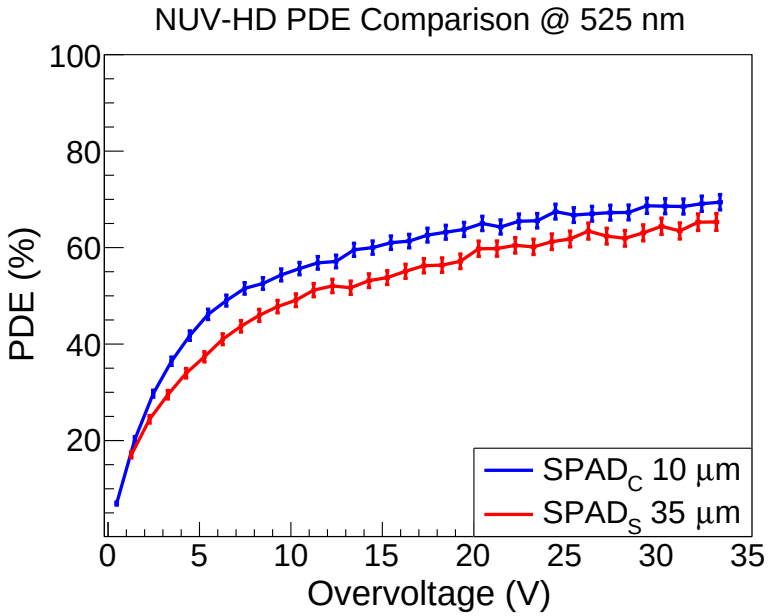

Figure 5.9: A comparison of the square SPAD PDE and the circular SPAD PDP, multiplied by the nominal FF of the square device, at 525 nm is shown. The scaled PDP is always larger than the square SPAD PDE because the FF_{Eff} is smaller than the on defined by the layout.

In Figure 5.10, the ratios between FF_{Eff} and the nominal one, as a function of the overvoltage, for different wavelength measurements, ranging from NUV to NIR, are shown. The measurements errors are omitted to have a more clear plot. A relative error of ∼5 % is found on average, thus all the wavelengths are in agreement within the errors. The electric field model of a perfect box in the total device depth agrees with these measurements because different wavelengths, thus photons absorbed at different depths, show no different ratio between the effective and the nominal FF. The FF_{Eff} never reaches the nominal value. In the typical SiPM operational overvoltage range (between 5 and 10 V), the FF_{Eff} ranges between 80 % and 90 % of the nominal value, for the 35 μm cell.

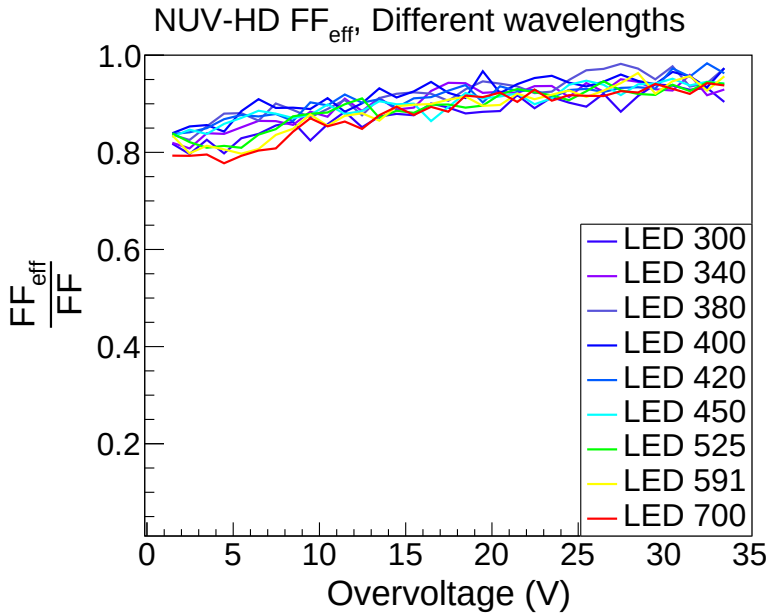

Figure 5.10: Ratio between the measured FF_{Eff} and the nominal one at different wavelengths. The measurement errors are not drawn for clarity, they have a relative value of about 5 %. All the measurement at different wavelengths are in agreement confinrming the box model.

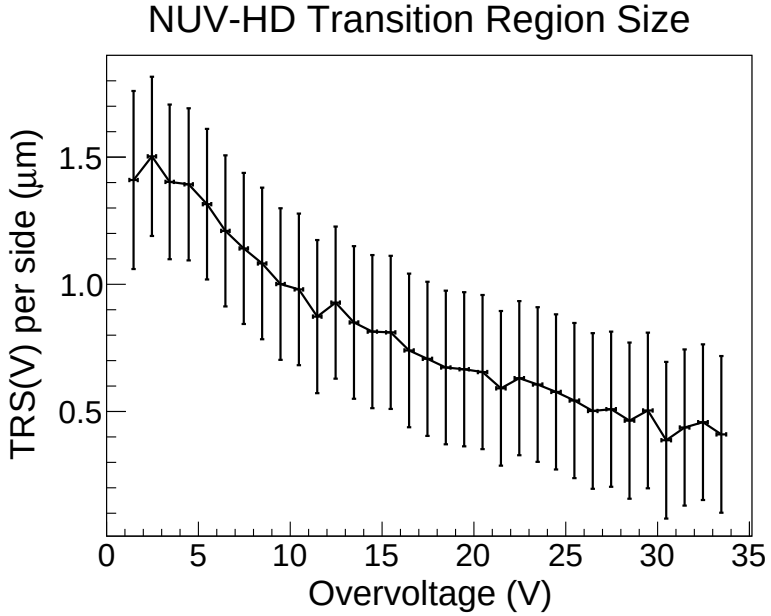

Figure 5.11: Measured transition region size (TRS) of the NUV–HD technology. In the realistic biasing range, up to about 10 V, the TRS ranges between 1 μm and 1.5 μm.

From the FF_{Eff}, it is possible to calculate the transition region size (TRS) around the active area of the cell. Following the box model proposed in the section 5.1, from the FF_{Eff}, the following equation (5.8) derives:

$$TRS(V) = \frac{\sqrt{FF} - \sqrt{FF_{Eff}}}{2} CS \tag{5.8}$$

in which CS is the cell pitch and the factor two is inserted to calculate the TRS per side. In Figure 5.11, the calculated TRS(V) is shown. In the typical operational overvoltage range, it has values between ∼1 and ∼1.5 μm per side.

Inverting the equation (5.8), the calculated TRS(V) can be used to estimate the FF_{Fff} of the other NUV–HD large cells. The nominal FF of the cells 25 μm, 30 μm and 40 μm are 72 %, 77 % and 83 %, respectively. In Figure 5.12, the simulated FF_{Eff} are shown. The smallest cell, the 25 μm one, has an expected FF_{Eff} between 55 % and 60 % in the typical operational overvoltage, much lower than the nominal one. For larger cells, the effect of the transition region becomes less and less important. In the 40 μm device, the reduction of the FF_{Eff} compared to the nominal value is about 10 % in the operating condition.

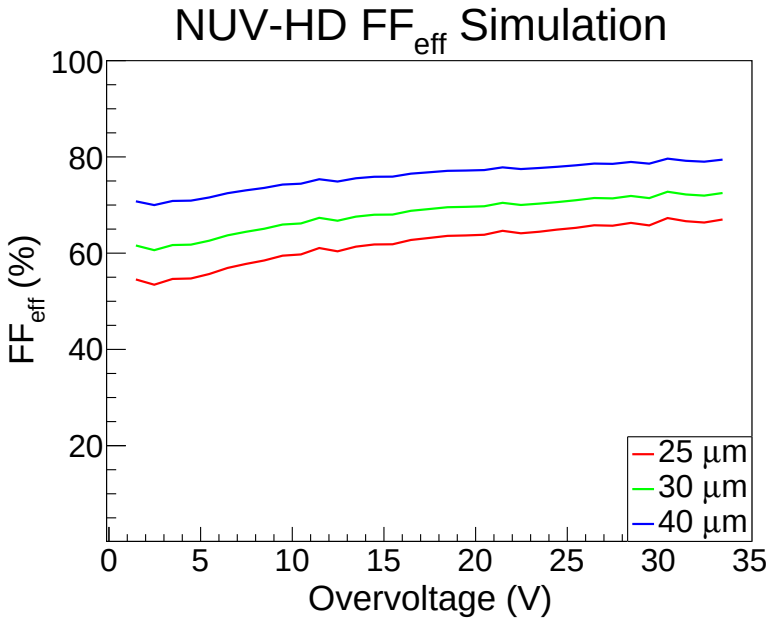

Figure 5.12: Simulated effective FF (FF_{Eff}) of the NUV–HD large cells calculated inverting the equation (5.8) using the TRS calculated before. The effect of the TRS(V) on the FF_{Eff} is more important in the smallest cell. In the realistic biasing range the 25 μm cell device has a FF_{Eff} not exceeding the 60 %, much less than the 72 % nominal value.

If these results are extended to the NUV–HD small cells, with cell pitch equal to 15 μm and 20 μm, the situation worsens. The FF_{Eff} of these devices,

in the operating condition, is below the 50 %, not more than the 75 % of the nominal value.

Even if the TRS impact decreases with the cell size, the production of larger cells, over the actual 35–40 μm, would not solve the difference between the effective FF and the one defined by the layout. To significantly improve the PDE performance of all the cell size devices, a smaller TRS(V) must be obtained. This will be possible with a technology redesign of the active area border regions.

Conclusion

In this thesis, a silicon photodetector type, that is catching a growing interest, is investigated: the Silicon Photomultiplier (SiPM). It is a pixelated photosensor operated at a reverse bias voltage larger than the breakdown one. After a brief introduction of the detector, the main features of the device are shown paying more attention on the noise sources and on the detection efficiency.
Two main detector noise sources are identified: primary noise, or dark count rate (DCR), and correlated noise (afterpulsing and cross–talk). The DCR, at room temperature, is mainly attributed to the thermally generated electron–hole pairs having the possibility to reach the high–field region triggering an avalanche signal not correlated with the arrival of incoming photons. These signals are identical to the ones generated by incoming photons, thus the DCR is always summed up to the detector response to incoming light. The other noise source is always caused by a primary fired cell, either by a spontaneous event or by a photogenerated one. For this reason it is called correlated noise. An afterpulsing event is generated by a carrier of an avalanche trapped in a crystal defect and released after a proper time, triggering a secondary avalanche with an average lower number of carriers due to the lower effective bias voltage of the cell. An optical cross–talk event is caused by the secondary photons, travelling from a fired cell to a neighbouring one, emitted by the hot carriers in the avalanche. This last noise is subdivided into two types, direct and delayed. The first one is due to the secondary photons reaching the neighbouring cell and generating an electron–hole pair in the active volume, the last one is due to the secondary photons reaching the substrate of a neighbouring cell and generating an electron–hole pair that diffuse into the active volume.
The SiPM photo–detection efficiency (PDE) is defined as the ratio among the average number of detected photons and the incoming ones. The PDE is the product of three different terms: fill factor (FF), quantum efficiency ($QE(\lambda)$) and triggering probability ($T_P(V,\lambda)$). The first is the ratio between the active area and the total one of the cell; the second is the probability that an incoming photon is absorbed in the silicon and the photogenerated carriers can reach the high–field region; the last term is the probability for a carrier to trigger an avalanche in the detector.

After the general discussion about the detector, a great attention is given to the development of SiPMs at Fondazione Bruno Kessler (FBK, Trento, Italy)

in the last decade. The activity began in 2005 within a three–year collaboration with the Italian National Institute for Nuclear Physics (INFN). The first SiPM produced was in n–on–p technology with a dimension of 1x1 mm^2 and a cell pitch of 40 μm. During the first years development, many important steps about the characterisation procedure were done. In particular, the study of the IV and the development of automatic procedures to measure the IV on wafer, before cutting the devices. During the subsequent years, new SiPM productions improve the performance. The typical DCR decreased from the initial value of a few MHz/mm^2 to some hundred KHz/mm^2, the breakdown uniformity on wafer decreases to some hundred mV and the PDE increased to over the 30 % in the visible spectrum. In 2013, two separate technology lines were presented, called RGB–SiPMs and NUV–SiPMs. The first technology was the successor of the original one, while the last technology was a p–on–n with peak efficiency in the NUV–violet part of the electromagnetic spectrum. The two technologies had a very similar layout, with the only difference in the dopant–type profiles. The NUV technology was further developed in these last three years. The first important upgrade to the technology was the adoption of a new substrate with a lower carrier lifetime, leading to the NUV–Low–AP technology. This technology had a very big improvement in terms of delayed correlated noise suppression. As shown, the original NUV–SiPMs suffered from a very high delayed noise probability that reduced their operating overvoltage, having an effect also on the maximum achievable PDE. The new technology, reducing the noise probability by about one order of magnitude, put the operating overvoltage limit at least two times the previous one, allowing to better exploit the device properties. The last important upgrade was the introduction of the High–Density (HD) concept on the Low–AP technology. The main features of the HD concept were the introduction of deep trenches to electrically and optically isolate the cells and a new layout with smaller inefficient border regions. The trenches had to reduce the optical transmission of the secondary photons from a cell to a neighbouring one, reducing the cross–talk probability, while, due to the increased FF, the devices were expected to have a larger PDE.

The NUV–HD SiPMs are extensively studied in this thesis. A complete characterisation procedure, able to extract all the important parameters from a new production is developed and presented. First, the FBK standard characterisation procedure in dark is reported in detail. It allows to extract the gain, the time constant of the cell recharge, all the information about the noise sources, both primary and correlated, and the Excess Charge Factor (ECF), the average amount of charge associated to the correlated noise summed up to the primary event charge. This procedure exploits the important advantages of the Differential Leading Edge Discriminator filter (DLED), thus it is presented too. For every extracted parameter, the measurement error source and value is given.

For the PDE measurement, a new set–up and three different methods are developed and presented. About the set–up, a complete study on the errors associated to the use of LEDs as light sources is presented. In particular, a dependence of the LED light emission spectrum on the applied bias voltage is observed. The light calibration procedure at the device location is described and different light sources are compared obtaining a very good agreement in the visible range. The uniformity of light at the device position is assured by a direct measurement using a SPAD and two micropositioners. The use of an optical fibre to transport the light is also tested and found adequate only for light with wavelength longer than 350 nm. About the methods, a detailed description is given and advantages and drawbacks are discussed for each one. In every method, precautions able to reduce the correlated noise influence on the results to a negligible value are described. The three methods are equivalent in terms of the measurement precision and reliability showing the agreement in the results obtained with two SiPMs 1x1 mm^2 with different cell pitch at different wavelengths ranging from NUV to NIR. The only observed difference is the measurement time. The continuous counting method (CCM) represents a good compromise for a single measurement; the pulsed counting method (PCM) allows to measure the PDE of a few wavelengths in the same time, but it increases the complexity of the set–up requiring a fast pulse generator; the photocurrent method (PM) is the optimal choice for a complete PDE scan, but a preliminary characterisation in dark, to know the ECF, is required. At last, the equivalence between the PDE measured on SiPMs and SPADs, having the same layout of single SiPM cells, is shown. This result is of fundamental importance because the SPADs have the advantages of an increased measurement precision in a lower time and the possibility to bias at a larger overvoltage the devices then the SiPMs allowing to obtain more information in extreme conditions.

The described set–ups and characterisation procedures are used to carry out the measurements on NUV–HD SiPMs of different cell sizes, ranging from 25 μm to 40 μm. During this characterisation, different devices, taken from two wafers, are measured to assure the uniformity of the parameters among the devices. The results are always in agreement, thus the expected uniformity is demonstrated. The only parameter that exhibits an experimental distribution larger than expected is the DCR. The statistical fluctuations of defects inside the wafer is responsible to the different DCR of the SiPMs. From the automatic IV measurement, the maximum DCR is estimated almost three times larger than the minimum one. To better compare the devices with different cell size, all the data are plotted as a function of the PDE. From this comparison, the 25 μm device is found worse than the larger cell devices, having a larger noise, both primary and correlated, at any PDE value. The other cells are equivalent within the measurement errors, only the DCR is found decreasing with the cell pitch. Thus, at last, the 40 μm cell size device is defined as the

best choice, but the 30 μm and the 35 μm devices are almost as good as the largest cell one. The NUV–HD larger cells have a PDE larger than 50 % with a correlated noise probability (sum of the cross–talk and afterpulsing) of about 20 % and an average primary noise of 60–70 KHz/mm^2. In particular, the NUV–HD technology was found very well suited for the Cherenkov Telescope Array Observatory (CTA), having a PDE spectrum peaked at about 400 nm well matching the Cherenkov radiation spectrum in the Earth atmosphere, and a very high signal–to–noise ratio, defined as the peak PDE with respect to the DCR and correlated noise probability.

During the PDE measurements, an unexpected behaviour is observed, namely a lower measured FF with respect to the expected one (defined by the layout). To better understand this observation, a complete study of the factors contributing to the PDE is performed. Three different devices are used: a photodiode, a circular SPAD with 100 % FF and a square SPAD with 35 μm cell size (having an equal layout to a single SiPM cell) and a nominal FF equal to 81 %. The measurements on low dark current photodiodes allow to directly obtain the technology QE(λ). These measurements show a very high QE(λ) in the NUV and visible wavelength ranges, exceeding the 80 % in the peak PDE region. At longer wavelengths, the QE decreases due to the small active volume (equal to the epitaxial layer thickness). The PDP of the circular SPADs with 100 % FF is measured and fitted with an experimentally derived function, found in literature, describing the increase of the PDP, or PDE, considering also the FF contribution, with the overvoltage at a single wavelength. This function shows an incompatibility to represent the acquired data at large overvoltage, thus a new function is proposed. With this model, a saturation rate parameter, V_λ, is defined and shown as a function of the wavelength. From the fit procedure, the QE(λ) is also extracted and compared to the photodiode QE(λ) direct measurement finding a good agreement. The square SPAD is tested to measure the effective FF (FF_{Eff}). The FF_{Eff} ranges between the 80 % and the 90 % of the nominal value in the typical operational overvoltage range and a transition region size (TRS(V)) between 1 and 1.5 μm is estimated. The FF_{Eff} is critical because in the smallest devices, with cell pitch lower than 25 μm, its value is only the 50–60 % of the nominal value, reducing the achievable maximum PDE. It is also found that the FF_{Eff} better approaches the nominal value in the larger cells but, even increasing the cell size over the actual 40 μm, the device would not show a further significant improvement. For this reason, a smaller TRS(V) must be obtained, redesigning the electric field border region, to further improve the PDE.

The study of the factors contributing to the PDE was very important because it allowed a better knowledge of these factors limiting the SiPMs PDE, in particular, in the small cell size devices. This knowledge will help in addressing the technological aspects that should be modified in order to further improve the PDE.

Bibliography

[1] A. Kelber et al. (2003). Animal colour vision – behavioural tests and physiological concepts. *Biol. Rev.*, *78*(1), 81–118.

[2] https://mwmw.gsfc.nasa.gov/.

[3] J. E. Elias (for the CMS Hadron Calorimeter Readout Group). Photodetectors for the CMS hadron calorimeters. *Nucl. Instrum. Methods A*, 387 (1997) 104–106.

[4] X. Michalet et al. Hybrid photodetector for single–molecule spectroscopy and microscopy. *Proc. SPIE* doi:10.1117/12.763449.

[5] R. Esper-Chaín et al. Configurable Quadrant Photodetector: An Improved Position Sensitive Device. *IEEE Sens. J.*, vol. 16, no. 1, pp. 109–119, Jan. 1, 2016.

[6] A. Ferri et al. Performance of FBK low–afterpulse NUV silicon photomultipliers for PET application. 2016 *JINST* **11** P03023.

[7] H. Anderhub et al. Design and operation of FACT - the first G–APD Cherenkov telescope. 2013 *JINST* **8** P06008.

[8] P. L. Richards. Bolometers for infrared and millimeter waves. *J. Appl. Phys.*, 1994 76:1, 1–24.

[9] S. P. T. The Bolometer. *Nat.*, **57**, 620–622 (28 April 1898).

[10] W. S. Boyle and K. F. Rodgers. Performance Characteristics of a New Low–Temperature Bolometer. *J. Opt. Soc. Am.*, 49, 66–69 (1959).

[11] A. E. Lange et al. Improved fabrication techniques for infrared bolometers. *Int. J. Infrared Milli. Waves*, 1983 Sep. 1, vol. 4, issue 5, pp. 689–706.

[12] E. E. Haller et al. NTD Germanium: A Novel Material for Low Temperature Bolometers. In *Neutron Transmutation Doping of Semiconductor Materials (1984th Edition)*, Proceedings of the Fourth International Conference on Neutron Transmutation Doping of Semiconductor Materials, 21–36.

[13] E. E. Haller. Physics and design of advanced IR bolometers and photoconductors. *Infrared Phys.*, vol. 25, No. 1, pp. 257–266, 1985.

[14] C. W. Siemens. On the Increase of Electrical Resistance in Conductors with Rise of Temperature, and Its Application to the Measure of Ordinary and Furnace Temperatures; Also on a Simple Method of Measuring Electrical Resistances. Royal Society, 1871.

[15] H. Hertz. Ueber einen Einfluss des ultravioletten Lichtes auf die electrische Entladung. *Ann. Phys.*, vol. 267, no. 8, pp. 983–1000.

[16] W. Hallwachs. Ueber den Einfluss des Lichtes auf electrostatisch geladen Körper. *Ann. Phys.*, vol. 269, issue 2, pp. 301–312.

[17] J. Elster and H. Geitel. Ueber die Entladung negativ electrischer Körper durch das Sonnen–und Tageslicht. *Ann. Phys.*, vol. 274, issue 12, pp. 497–514.

[18] A. Einstein. Ueber einen die Erzeugung und Verwandlung des Lichtes betraffenden heuristichen Gesichtspunkt. *Ann. Phys.*, vol. 322, issue 6, pp. 132–148.

[19] V. K. Zworykin et al. In *Proc. IRE 24 (3)*, 1936.

[20] B. K. Lubsandorzhiev. On the history of photomultiplier tube invention. *Nucl. Instrum. Methods A*, 567 (2006) 236–238.

[21] J. Rajchman and E. W. Pike. Electrostatic focusing in Secondary Emission Multipliers. Technical report, *RCA Technical Report*, TR–362, Sept. 1937.

[22] *Photomultiplier Tubes: Basics and Applications (Third Edition).* HAMAMATSU PHOTONICS KK.

[23] A. J. Dekker. *Advances in Research and Applications.* Academic Press, New York (1958).

[24] A. Dubus et al. Improved age–diffusion model for low–energy electron transport in solids. II. Application to secondary emission from aluminum. *Phys. Rev. B*, 36, 5093, 1 Oct. 1987.

[25] O. Hachenberg and W. Brauer. *Secondary Electron Emission from Solids.* Academic Press, New York (1959).

[26] S. M. Sze and Kwok K. NG. *Physics of Semiconductor Devices (3rd Edition - 2006).* Wiley–Interscience.

[27] K. G. McKay and K. B. McAfee. Electron Multiplication in Silicon and Germanium. *Phys. Rev.*, 91, 1079, 1 Sept. 1953.

[28] K. M. Johnson. High–Speed Photodiode Signal Enhancement at Avalanche Breakdown Voltage. *IEEE Trans. Electron Devices*, vol. 12, no. 2, pp. 55–63, Feb. 1965.

[29] P. P. Webb et al. Properties of avalanche photodiodes. *RCA Rev.*, 1975, vol. 35, 234–278.

[30] R. J. McIntyre. Multiplication Noise in Uniform Avalanche Diodes. *IEEE Trans. Electron Devices*, vol. ED–13, no. 1, pp. 164–168, Jan. 1966.

[31] R. J. McIntyre. The Distribution of Gains in Uniformly Multiplying Avalanche Photodiodes: Theory. *IEEE Trans. Electron Devices*, vol. 19, no. 6, pp. 703–713, June 1972.

[32] R. B. Emmons. Avalanche Photodiode Frequency Response. *J. Appl. Phys.*, 1967 38:9, 3705–3714.

[33] *Avalanche Photodiodes (Application Report).* Laser Components.

[34] *Opto–semiconductor handbook.* HAMAMATSU PHOTONICS KK.

[35] S. Cova et al. Towards picosecond resolution with single–photon avalanche diodes. *Rev. Sci. Instrum.*, vol. 52, no. 3, 408–412 (1981).

[36] S. Cova et al. A Semiconductor Detector for Measuring Ultraweak Fluorescence Decays with 70 ps FWHM Resolution. *IEEE J. Quantum Electron.*, vol. 19, no. 4, pp. 630–634, April 1983.

[37] B. F. Levine and C. G. Bethea. Detection of single 1.3 μm photons at 45 Mbit/s. *Electron. Lett.*, vol. 20, no. 6, pp. 269–271, March 1984.

[38] R. J. McIntyre. Recent developments in silicon avalanche photodiodes. *Meas.*, vol. 3, no. 4, pp. 146–152 (1985).

[39] S. Cova et al. Avalanche semiconductor detector for single optical photons with a time resolution of 60 ps. *Nucl. Instrum. Methods A*, 253 (1987) 482–487.

[40] A. Lacaita et al. Four–hundred–picosecond single–photon timing with commercially available avalanche photodiodes. *Rev. Sci. Instrum.*, vol. 59, no. 7, 1115–1121 (1988).

[41] A. Lacaita et al. Double epitaxy improves single–photon avalanche diode performance. *Electron. Lett.*, vol. 25, no. 13, pp. 841–843, June 1989.

[42] S. Cova et al. 20–ps timing resolution with single–photon avalanche diodes. *Rev. Sci. Instrum.*, vol. 60, no. 6, 1104–1110 (1989).

[43] A. Lacaita et al. Observation of avalanche propagation by multiplication assisted diffusion in p–n junctions. *Appl. Phys. Lett.*, vol. 57, no. 5, 489–491 (1990).

[44] M. Ghioni and G. Ripamonti. Improving the performance of commercially available Geiger–mode avalanche photodiodes. *Rev. Sci. Instrum.*, vol. 62, no. 1, 163–167 (1991).

[45] N. S. Nightingale. A new silicon avalanche photodiode photon counting detector module for astronomy. *Exp. Astron.*, (1990) 1:407.

[46] A. Lacaita et al. Recent advances in the detection of optical photons with silicon photodiodes. *Nucl. Instrum. Methods A*, 326 (1993) 290–294.

[47] H. Dautet et al. Photon counting techniques with silicon avalanche photodiodes. *Appl. Opt.*, 32, 3894–3900 (1993).

[48] S. Cova et al. Avalanche photodiodes and quenching circuits for single–photon detection. *Appl. Opt.*, 35, 1956–1976 (1996).

[49] S. Cova et al. Active–Quenching and Gating Circuits for Single–Photon Avalanche Diodes (SPADs). *IEEE Trans. Nucl. Sci.*, vol. 29, no. 1, pp. 599–601, Feb. 1982.

[50] T. E. Ingerson et al. Photon counting with photodiodes. *Appl. Opt.*, 22, 2013–2018 (1983).

[51] R. G. W. Brown et al. Characterization of silicon avalanche photodiodes for photon correlation measurements. 2: Active quenching. *Appl. Opt.*, 26, 2383–2389 (1987).

[52] R. G. W. Brown et al. Characterization of silicon avalanche photodiodes for photon correlation measurements. 1: Passive quenching. *Appl. Opt.*, 25, 4122–4126 (1986).

[53] N. Bacchetta et al. MRS detectors with high gain for registration of weak visible and UV light fluxes. *Nucl. Instrum. Methods A*, 387 (1997) 225–230.

[54] A. V. Akindinov et al. New results on MRS APDs. *Nucl. Instrum. Methods A*, 387 (1997) 231–234.

[55] G. Bondarenko et al. Limited Geiger–mode silicon photodiode with very high gain. *Nucl. Phys. B (Proc. Suppl.)*, vol. 61, no. 3, 347–352, (1998).

[56] S. Vasile et al. Photon Detection with High Gain Avalanche Photodiode Arrays. *IEEE Trans. Nucl. Sci.*, vol. 45, no. 3, pp. 720–723, Jun. 1998.

[57] S. Vasile et al. High Gain Avalanche Photodiode Arrays for DIRC Applications. *IEEE Trans. Nucl. Sci.*, vol. 46, no. 4, pp. 848–852, Aug. 1999.

[58] G. Bondarenko et al. Limited Geiger–mode microcell silicon photodiode: new results. *Nucl. Instrum. Methods A*, 442 (2000) 187–192.

[59] V. Saveliev and V. Golovin. Silicon avalanche photodiodes on the base of metal–resistor–semiconductor (MRS) structures. *Nucl. Instrum. Methods A*, 442 (2000) 223–229.

[60] B. Dolgoshein et al. An advanced study of silicon photomultiplier. *ICFA Instrum. Bull.*, 23 (2001) 28–41.

[61] P. Buzhan et al. Silicon photomultiplier and its possible applications. *Nucl. Instrum. Methods A*, 504 (2003) 48–52.

[62] D. Renker. Geiger–mode avalanche photodiodes, history, properties and problems. *Nucl. Instrum. Methods A*, 567 (2006) 48–56.

[63] S. Seifert et al. Simulation of Silicon Photomultiplier Signals. *IEEE Trans. Nucl. Sci.*, vol. 56, no. 6, pp. 3726–3733, Dec. 2009.

[64] F. Acerbi et al. High Detection Efficiency and Time Resolution Integrated–Passive–Quenched Single–Photon Avalanche Diodes. *IEEE J. Sel. Top. Quantum Electron.*, vol. 20, no. 6, pp. 268–275, Nov.–Dec. 2014.

[65] *SensL C–Series SiPM Datasheet*. SensL Technologies Ltd.

[66] *MPPC and MPPC module for precision measurement*. HAMAMATSU PHOTONICS KK.

[67] S. Gundacker et al. State of the art timing in TOF–PET detectors with LuAG, GAGG and L(Y)SO scintillators of various sizes coupled to FBK–SiPMs. 2016 *JINST* **11** P08008.

[68] B. Lutz and the CMS Collaboration. Upgrade of the CMS Hadron Outer Calorimeter with SiPM sensors. 2012 *J. Phys.: Conf. Ser.* **404** 012018.

[69] F. Acerbi et al. NUV Silicon Photomultipliers With High Detection Efficiency and Reduced Delayed Correlated–Noise. *IEEE Trans. Nucl. Sci.*, vol. 62, no. 3, pp. 1318–1325, June 2015.

[70] C. Piemonte et al. Development of an automatic procedure for the characterization of silicon photomultipliers. *2012 IEEE Nucl. Sci. Symp. Med. Imaging Conf. Rec. (NSS/MIC)*, Anaheim, CA, 2012, pp. 428–432.

[71] G. Zappala' et al. Set–up and methods for SiPM Photo–Detection Efficiency measurements. 2016 *JINST* **11** P08014.

[72] J. A. del Alamo and R. M. Swanson. Modelling of minority–carrier transport in heavily doped silicon emitters. *Solid–State Electron.*, vol. 30, no. 11, 1127–1136 (1987).

[73] M. S. Tyagi and R. Van Overstraeten. Minority carrier recombination in heavily–doped silicon. *Solid–State Electron.*, vol. 26, no. 6, 577–597 (1983).

[74] K. S. Champlin. Microplasma Fluctuations in Silicon. *J. Appl. Phys.*, 1959 30:7, 1039–1050.

[75] R. J. McIntyre. Theory of Microplasma Instability in Silicon. *J. Appl. Phys.*, 1961 32:6, 983–995.

[76] R. H. Haitz. Model for the Electrical Behavior of a Microplasma. *J. Appl. Phys.*, 1964 35:5, 1370–1376.

[77] R. H. Haitz. Mechanisms Contributing to the Noise Pulse Rate of Avalanche Diodes. *J. Appl. Phys.*, 1965 36:10, 3123–3131.

[78] W. G. Oldham. New Method for Breakdown Voltage Determination in p–n Junctions. *Appl. Phys. Lett.*, vol. 19, no. 11, 466–467 (1971).

[79] W. G. Oldham. Triggering Phenomena in Avalanche Diodes. *IEEE Trans. Electron Devices*, vol. 19, no. 19, pp. 1056–1060, Sep. 1972.

[80] C. Piemonte. A new Silicon Photomultiplier structure for blue light detection. *Nucl. Instrum. Methods A*, 568 (2006) 224–232.

[81] R. Van Overstraeten and H. De Man. Measurement of the ionization rates in diffused silicon p–n junctions. *Solid–State Electron.*, vol. 13, no. 5, 583–608 (1970).

[82] W. N. Grant. Electron and hole ionization rates in epitaxial silicon at high electric fields. *Solid–State Electron.*, vol. 16, no. 10, 1189–1203 (1973).

[83] W. Maes et al. Impact ionization in silicon: a review and update. *Solid–State Electron.*, 33 (1990) 705.

[84] M. Ghioni et al. Compact active quenching circuit for fast photon counting with avalanche photodiodes. *Rev. Sci. Instrum.*, vol. 67, no. 10, 3440–3448 (1996).

[85] C. Piemonte et al. Characterization of the First Prototypes of Silicon Photomultiplier Fabricated at ITC–irst. *IEEE Trans. Nucl. Sci.*, vol. 54, no. 1, pp. 236–244, Feb. 2007.

[86] C. Piemonte et al. New results on the characterization of ITC–irst Silicon Photomultipliers. *2006 IEEE Nucl. Sci. Symp. Conf. Rec.*, San Diego, CA, 2006, pp.1566–1569.

[87] G. Collazuol et al. Studies of silicon photomultipliers at cryogenic temperatures. *Nucl. Instrum. Methods A*, 628 (2011) 389–392.

[88] C. Piemonte et al. Recent Developments on Silicon Photomultipliers produced at FBK–irst. *2007 IEEE Nucl. Sci. Symp. Conf. Rec.*, Honolulu, HI, 2007, pp. 2089–2092.

[89] G. Llosa' et al. Energy and Timing Resolution Studies With Silicon Photomultipliers (SiPMs) and 4–Pixel SiPM Matrices for PET. *IEEE Trans. Nucl. Sci.*, vol. 56, no. 3, pp. 543–548, June 2009.

[90] G. Llosa' et al. Monolithic 64–channel SiPM matrices for Small Animal PET. *2009 IEEE Nucl. Sci. Symp. Conf. Rec. (NSS/MIC)*, Orlando, FL, 2009, pp. 2658–2661.

[91] C. Piemonte et al. Timing performance of large area SiPMs coupled to LYSO using dark noise compensation methods. *2011 IEEE Nucl. Sci. Symp. Conf. Rec.*, Valencia, 2011, pp. 59–63.

[92] R. I. Wiener et al. Timing and Energy Characteristics of LaBr3[Ce] and CeBr3 Scintillators Read by FBK SiPMs. *2011 IEEE Nucl. Sci. Symp. Conf. Rec.*, Valencia, 2011, pp. 4013–4019.

[93] C. Piemonte et al. Performance of FBK SiPMs coupled to PETA3 read–out ASIC for PET application. *Nucl. Instrum. Methods A*, 718 (2013) 345–346.

[94] A. Gola et al. The DLED Algorithm for Timing Measurements on Large Area SiPMs Coupled to Scintillators. *IEEE Trans. Nucl. Sci.*, vol. 59, no. 2, pp. 358–365, April 2012.

[95] A. Tarolli et al. Influence of the active area size and read–out method on the timing performance of SiPMs coupled to LYSO scintillators. *Nucl. Instrum. Methods A*, 702 (2013) 77–79.

[96] N. Serra et al. Characterization of new FBK SiPM technology for visible light detection. 2013 *JINST* **8** P03019.

[97] A. Ferri et al. First results on NUV–SiPMs at FBK. *Nucl. Instrum. Methods A*, 718 (2013) 371–372.

[98] T. Pro et al. New Developments of Near–UV SiPMs at FBK. *IEEE Trans. Nucl. Sci.*, vol. 60, no. 3, pp. 2247–2253, June 2013.

[99] A. Ferri et al. Performance of FBK low–afterpulse NUV silicon photomultipliers for PET application. 2016 *JINST* **11** P03023.

[100] C. Piemonte et al. Characterization of the First FBK High–Density Cell Silicon Photomultiplier Technology. *IEEE Trans. Electron Devices*, vol. 60, no. 8, pp. 2567–2573, Aug. 2013.

[101] F. Acerbi et al. Technological and design improvements of FBK NUV silicon–photomultipliers. In *2015 Fotonica AEIT Italian Conference on Photonics Technologies*, pages 1–3.

[102] C. Piemonte et al. Performance of NUV–HD Silicon Photomultiplier Technology. *IEEE Trans. Electron Devices*, vol. 63, no. 3, pp. 1111–1116, March 2016.

[103] G. Llosa'. Overview of Silicon Photomultiplier Applications. *Proc. Sci.*, PoS(PhotoDet 2012)013.

[104] P. Bohn et al. Radiation damage studies of silicon photomultipliers. *Nucl. Instrum. Methods A*, 598 (2009) 722–736.

[105] A. Berra et al. Silicon Photomultipliers as a Readout System for a Scintillator–Lead Shashlik Calorimeter. *IEEE Trans. Nucl. Sci.*, vol. 58, no. 3, pp. 1297–1307, June 2011.

[106] F. Simon and C. Soldner. Uniformity studies of scintillator tiles directly coupled to SiPMs for imaging calorimetry. *Nucl. Instrum. Methods A*, 620 (2010) 196–201.

[107] A. Ebrahimi (on behalf of the CALICE Collaboration). Commissioning of the New Multi–layer Integration Prototype of the CALICE Tile Hadron Calorimeter. *2014 IEEE Nucl. Sci. Symp. Conf. Rec. (NSS/MIC*, Seattle, WA, 2014, pp. 1–3.

[108] *BC-418, BC-420, BC-422 Premium Plastic Scintillators.* Saint–Gobain.

[109] A. Ferri et al. Performance of FBK high–density SiPM technology coupled to Ce:LYSO and Ce:GAGG for TOF–PET. *Phys. Med. Biol.*, 2014 Feb. 21;59(4):869–880.

[110] I. Sacco et al. A compact, high–density gamma–detection module for Time–of–Flight measurements in PET applications. *Nucl. Instrum. Methods A*, 824 (2015) 233–236.

[111] Sun Il Kwon et al. Bismuth germanate coupled to near ultraviolet silicon photomultipliers for time–of–flight PET. *Phys. Med. Biol.*, 2016 Sept. 21;61(18):L38–L47.

[112] R. Mao et al. Emission Spectra of LSO and LYSO Crystals Excited by UV Light, X–Ray and γ–ray. *IEEE Trans. Nucl. Sci.*, vol. 55, no. 3, pp. 1759–1766, June 2008.

[113] http://darkside.lngs.infn.it/.

[114] http://next.ific.uv.es/next/.

[115] B. Bottino et al. The Darkside Experiment. *IL NUOVO CIMENTO*, **40 C** (2017) 52.

[116] F. Acerbi et al. Cryogenic Characterization of FBK HD Near–UV Sensitive SiPMs. *IEEE Trans. Electron Devices*, vol. 64, no. 2, pp. 521–526, Feb. 2017.

[117] D. Lorca et al. The NEXT experiment: A high pressure xenon gas TPC for neutrinoless double beta decay searches. *Nucl. Instrum. Methods A*, 718 (2013) 387–390.

[118] J. J. Gomez Cadenas et al. Present Status and Future Perspectives of the NEXT Experiment. *Adv. High Energy Phys.*, vol. 2014 (2014), Article ID 907067.

[119] V. Alvarez et al. SiPMs coated with TPB: coating protocol and characterization for NEXT. 2012 *JINST* **7** P02010.

[120] https://www.cta observatory.org/.

[121] J. Hinton et al. A New Era in Gamma–Ray Astronomy with the Cherenkov Telescope Array. *Editorial/Astropart. Phys.*, 43, 1 – 2 (2013).

[122] https://www.auger.org/.

[123] L. D. Landau and E. M. Lifshitz. *Electrodynamics of Continuous Media (Second Edition Revised and Enalrged)*. Elsevier.

[124] https://www.mpi hd.mpg.de/hfm/HESS/.

[125] http://veritas.sao.arizona.edu/.

[126] https://magic.mppmu.mpg.de/.

[127] B. S. Acharya et al. Introducing the CTA concept. *Astropart. Phys.*, 43 (2013) 3-18.

[128] http://www.isdc.unige.ch/fact/.

[129] The CTA Consortium. Design concepts for the Cherenkov Telescope Array CTA: an advanced facility for ground–based high–energy gamma–ray astronomy. *Exp. Astron.*, (2011) 32: 193.

[130] D. Marano et al. Electro–optical characterization of MPPC detectors for the ASTRI Cherenkov telescope camera. *Nucl. Instrum. Methods A*, 768 (2014) 32–42.

[131] Seul Ki Yang et al. Precision measurement of the photon detection efficiency of silicon photomultipliers using two integrating spheres. *Opt. Express*, 22, 716–726 (2014).

[132] https://www.dynasil.com/knowledge-base/tunable-light sources/.

[133] http://www.roithner laser.com/led.html.

[134] https://www.thorlabs.com/newgrouppage9.cfm?objectgroup_id=2814.

[135] K. Yamamoto et al. Development of Multi–Pixel Photon Counter (MPPC). *2007 IEEE Nucl. Sci. Symp. Conf. Rec.*, Honolulu, HI, USA, 2007, pp.1511–1515.

[136] P. Eckert et al. Characterisation studies of silicon photomultipliers. *Nucl. Instrum. Methods A*, 620 (2010) 217.

[137] A. N. Otte et al. A measurement of the photon detection efficiency of silicon photomultipliers. *Nucl. Instrum. Methods A*, 567 (2006) 360.

[138] G. Zappala'. Performance of the latest prototypes of NUV–HD Silicon Photomultipliers.
https://indico.cern.ch/event/391665/contributions/1827320/.

[139] G. Zappala' et al. Study of the photo–detection efficiency of FBK High–Density silicon photomultipliers. 2016 *JINST* **11** P11010.

[140] C. Niclass et al. A Single Photon Avalanche Diode Implemented in 130–nm CMOS Technology. *IEEE J. Select. Topics Quantum Electron.*, vol. 13, no. 4, pp. 863–869, July–aug. 2007.

[141] C. Veerappan and E. Charbon. CMOS SPAD based on Photo–Carrier Diffusion Achieving PD $>$ 40% From 440 to 580 nm at 4 V Excess Bias. *IEEE Photon. Technol. Lett.*, vol. 27, no. 23, pp. 2445–2448, Dec. 1, 2015.